Plume Chemistry Simulations with the SCICHEM Model

Jessie van Hooft

Thesis submitted for the degree of
Master of Science in Environmental Chemistry
60 credits

Department of Chemistry
Faculty of Mathematics and Natural Sciences

UNIVERSITY OF OSLO

May 2023

Plume Chemistry Simulations with the SCICHEM Model

Jessie van Hooft

Thesis submitted for the degree of Master of Science in Environmental Chemistry

60 Credits

Department of Chemistry

Faculty of Mathematics and Natural Sciences

University of Oslo

May 2023

2023

Plume Chemistry Simulations with the SCICHEM Model

Jessie van Hooft

http://www.duo.uio.no/

Trykk: Reprosentralen, Universitetet i Oslo

Abstract

Amine-based post-combustion carbon capture is a method used for reducing CO_2 emissions from industrial point sources. During this process, amines can be released into the environment and form carcinogenic nitrosamines and nitramines. Consequently, the location where it is safe to build carbon capture facilities depends on the levels of carcinogens, and where in the atmosphere they are formed. In this project, power plant plume fields simulated using the plume chemistry model SCICHEM were compared to published results obtained with the Fluidity-Chem model. Following this, SCICHEM was used to understand the influence of the atmospheric chemical background, the applied atmospheric chemistry scheme and NO emission strength on the chemical evolution of an isolated ship plume. Subsequently, NO, NO_2, O_3 and OH fields were simulated after NO emission from a hypothetical Waste-to-Energy plant using SCICHEM, first without and later with the emission of the amine piperazine. It was found that SCICHEM cannot simulate plume edge details well, thereby emphasizing the need for more detailed models like the Volumetric Particle Approach model, currently under development at NILU, that was also tested for comparison. Moreover, the application of different chemistry schemes was found to lead to different results. Processes such as ozone titration, HNO_3 formation and HONO formation, should be included in the chemistry scheme. The atmospheric chemical background and especially the peroxy radicals therein, e.g. HO_2 and $CH_3C(O)O_2$, were found to play an important role in OH depletion or formation close to the source. Under low NO emission (i.e. 3.02 g/s), the conventional conception of OH being depleted near the source was found not to be valid. On the contrary, the OH chemistry starts close to the source, resulting in OH formation beginning at 2 km downwind from the source. As a result, piperazine nitrosamine and nitramine levels were found to be highest close to the source. With an emission of 0.032 g/s of piperazine, maximum nitrosamine and nitramine concentrations of 0.97 ng/m^3 and 0.72 ng/m^3, respectively, were found at surface level approximately 1 to 1.5 km downwind from the source. In the case of additional direct nitrosamine emission, the nitrosamine level increased to up to 1.54 ng/m^3 close to the source. Higher NO emissions of 30.2 g/s were found to lower the nitrosamine and nitramine concentrations, and shift the maximum concentration further downwind from the source due to increased OH depletion. Meteorological parameters and background conditions were simplified and kept constant throughout the entire run, which is not realistic. Therefore, improved simulations should be performed using varying background and meteorological conditions that are valid for the locations of interest.

Preface

I would like to start by thanking my supervisor Armin Wisthaler for introducing me to the field of atmospheric chemistry. I had no prior experience in this field, but I have learned so much in the last two years. Armin, your knowledge and inspiring passion have shown me how exciting and important atmospheric chemistry is. Thank you for steering me towards a project that suits my interests perfectly. Thank you for your guidance and practical assistance by providing some of the emission levels and the piperazine chemistry scheme. Your enthusiasm for the project and the ideas you contributed have made it a positive experience and helped me grow as a scientist.

Secondly, I would like to thank my second supervisor Massimo Cassiani for sharing his knowledge and experience. Massimo, your clear explanation of the SCICHEM and Volumetric Particle Approach models was invaluable to me. Moreover, I would like to thank you for providing the ambient conditions for the WtE plant and for the effort you put into running the Volumetric Particle Approach model to obtain results for this project.

Thirdly, I would like to thank Baptiste Languille. I am grateful for your help with getting the model to work, obtaining better graphs and interpreting some of the results. Your kindness, patience, enthusiasm and optimism really made this project an enjoyable experience!

Also, a big thank you to everyone else at the Atmospheric Chemistry Group at UiO. Even though we did not work together directly, the atmosphere within the group has been amazing! I have truly enjoyed my time here, and I could not have been more grateful that I was welcomed into this group. In particular I would like to thank Silje Solevåg, with whom I shared my two years at UiO. Thank you for being there to discuss ideas, results or simply helping me to find the correct words. Thank you for making our office a fun place to be. Your kindness, enthusiasm, passion and work ethic are inspiring!

A big thank you to my friends here in Norway, you have made my time here very special! And lastly, a special thank you to my friends and family back home in the Netherlands. Even though I have been far away from home for most of the last two years, you were always there for me and I really appreciate it!

Table of Contents

Abbreviations XI
Definitions XII
1 Introduction 1
1.1 The Atmospheric Impact of Amine-Based Post-Combustion Carbon Capture 2
1.2 Atmospheric Chemistry in a Combustion Plume 3
1.3 Atmospheric Chemistry of Piperazine 7
1.4 Reactive Plume Models 9
1.5 Aim of the Project 12
2 Methods 13
2.1 SCICHEM Model 14
2.2 Volumetric Particle Approach Model 15
2.3 Case Study 1: Power Plant Plume Chemistry Simulations 16
2.4 Case Study 2: Ship Plume Chemistry Simulations 17
2.4.1 Effect of Different Chemistry Schemes 18
2.4.2 Effect of Different Background Conditions 18
2.4.3 Effect of Reduced NO Emission on the OH Field 19
2.5 Case Study 3a: Waste-to-Energy Plant Plume Chemistry Simulations (without Amines) 19
2.5.1 Effect of Chemistry on the OH Field 20
2.5.2 Effect of Different Emissions on the OH Field 20
2.6 Case Study 3b: Waste-to-Energy Plant Plume Chemistry Simulations (with Amines) 20
2.7 SCICHEM and Volumetric Particle Approach Model Comparison 23
3 Results and Discussion 24
3.1 Case Study 1: Power Plant Plume Chemistry Simulations 24
3.2 Case Study 2: Ship Plume Chemistry Simulations 27
3.2.1 Effect of Different Chemistry Schemes 27
3.2.2 Effect of Different Background Conditions 30
3.2.3 Effect of Reduced NO Emission on the OH Field 36
3.2.4 Summary Case Study 2 38
3.3 Case Study 3a: Waste-to-Energy Plant Plume Chemistry Simulations (without Amines) 41

3.3.1 Effect of Chemistry on the OH Field 45
3.3.2 Effect of Different Emissions on the OH Field 46
3.3.3 Summary Case Study 3a 51
3.4 Case Study 3b: Waste-to-Energy Plant Plume Chemistry Simulations (with Amines) 56
3.4.1 Summary Case Study 3b 66
3.5 SCICHEM and Volumetric Particle Approach Model Comparison 70
3.5.1 Effect of Different NO Emission 79
4 Conclusion 87
References 92
Appendices 102
Appendix 1: Model Input 102
Appendix 2: Multi-component Input Files 116
Appendix 3: NILU-Provided Ambient Conditions 120
Appendix 4: Calculations 123

Abbreviations

CALPUFF	California Puff
CCS	Carbon Capture and Storage
CESAR	CO_2 Enhanced Separation and Recovery
EMEP	Cooperative Programme for Monitoring and Evaluation of the Long-range Transmission of Air Pollutants in Europe. In short called: European Monitoring and Evaluation Programme
GUI	Graphical User Interface
NILU	Norsk Institutt for Luftforskning (Norwegian Institute for Air Research)
PARADE	Panache Réactif en Atmosphère avec Dépôts (Atmospheric Reactive Plume with Deposits)
PCCC	Post-Combustion Carbon Capture
ppb	Parts per billion
ppm	Parts per million
ppt	Parts per trillion
ROME	Reactive and Optics Model of Emissions
SCIPUFF	Second-order Closure Integrated Puff
TRPM	Turbulent Reacting Plume Model
VMR	Volume Mixing Ratio
VOC	Volatile Organic Compound
VPA	Volumetric Particle Approach
WtE	Waste-to-Energy

Definitions

Actinic flux	Solar radiation that plays a role in photochemistry (Ryu et al., 2017).
Albedo	The fraction of the incoming solar radiation that is reflected by the surface (Knipping, 2021b; Song et al., 2019).
Bowen ratio	The ratio between sensible and latent heat fluxes from the surface to the air. Sensible heat fluxes are due to the temperature difference between surface and air. Latent heat fluxes are associated to water evaporation or condensation at the surface (Knipping, 2021b; Stull, 1983; Taylor, 2015).
Carbon Capture and Storage	A technique used to remove CO_2 from combustion emissions and store it (Scott et al., 2013).
Conserved scalar	Scalars that are not influenced by chemical reactions (Brown & Bilger, 1998).
Eulerian model	Model that simulates air parcels fixed at a specific location in the air (Vallero, 2021).
Fractional cloud cover	The fraction of the sky that is covered by clouds. 0 indicates a completely clear sky, whereas 1 indicates a completely overcast sky (Knipping, 2021b).
Gaussian puff method	An air pollution modelling method used to simulate three-dimensional concentration distributions, originating from a point source, using constant emissions and meteorological parameters (Lee et al., 2021).
Lagrangian model	Model that simulates air parcels moving with the local wind (Brasseur & Jacob, 2017).
Point source	A localized compact emission source at a fixed location, e.g. a stack (Chu & Wang, 2014).
Primary amine	A molecular functional group containing a nitrogen atom to which one carbon atom and two hydrogen atoms are bonded, i.e. $-CH_2NH_2$ (Yurkanis Bruice, 2017).
Puff	A cloud containing emitted species mixed with the air. Each puff moves with local wind and in mathematic models the

	concentration distribution of the emitted species is often assumed to be Gaussian within each puff (Nanni et al., 2022; Tomas et al., 2018).
Secondary amine	A molecular functional group containing a nitrogen atom to which two carbon atoms and one hydrogen atom are bonded, i.e. -CH_2NHCH_2- (Yurkanis Bruice, 2017).
Stochastic differential equations	"A differential equation whose coefficients are random numbers or random functions of the independent variable (or variables)" (Van Kampen, 2007, pp. 396).
Surface roughness (Roughness length)	The unevenness of a surface (Day & Chenoweth, 2013; Knipping, 2021b). The roughness length is a parameter relating near surface wind to the surface roughness in mathematical models (Shen et al., 2022).
Tertiary amine	A molecular functional group containing a nitrogen atom to which three carbon atoms are bonded, i.e. -$CH_2N(CH_2$-$)CH_2$- (Yurkanis Bruice, 2017).
Tracer	A compound of which a known amount is purposefully released into the atmosphere to follow the movement through the atmosphere (Simmonds et al., 2021).
Volume Mixing Ratio	Concentrations represented as mole fractions by volume (Brasseur & Jacob, 2017; Seinfeld & Pandis, 2016).
Volatile Organic Compound	"… any compound of carbon, excluding carbon monoxide, carbon dioxide, carbonic acid, metallic carbides or carbonates, and ammonium carbonate, which participates in atmospheric photochemical reactions" (United States Environmental Protection Agency, 2022b).

1 Introduction

Industrial combustion processes play an important role in the global energy supply chain. For example in power and Waste-to-Energy (WtE) plants, they transform fossil fuels (e.g. oil, coal or natural gas) or biofuels (e.g. fuels from waste or biomass) into electric energy (Guziana et al., 2014; Obermoser et al., 2009; Putrus & Bentley, 2016). Industrial combustion processes are, however, not only essential for the energy sector, but also for manufacturing industries like cement production (Canpolat et al., 2002; Thakuri et al., 2021).

Stacks in combustion plants are point sources of a number of pollutants, which play an important role in atmospheric chemistry. These pollutants can have negative impacts on human health as well as on the ecosystem (Benkovitz et al., 1996; Dignon, 1992; Hewitt, 2001; Kamal et al., 2017). One of the pollutants in combustion plant plumes is carbon dioxide (CO_2), an important greenhouse gas contributing to global warming. More than 65% of the greenhouse gas emissions from human activity, especially from fossil fuel usage, consists of CO_2 (IPCC, 2014). As a result, the CO_2 level in the atmosphere has increased by 50% since the 18^{th} century (National Aeronautics and Space Administration, 2023). Another pollutant found in combustion plant plumes is NO_x, which is a collective term used to indicate both nitrogen monoxide (NO) and nitrogen dioxide (NO_2) (Goldman et al., 2013; Queensland Government, 2022). Other pollutants also typically found in combustion plumes are: carbon monoxide (CO), sulfur dioxide (SO_2), nitrous acid (HONO) and acetaldehyde (CH_3CHO) (Müller et al., 2016; Neuman et al., 2016; Zeng et al., 2018).

Ending fossil fuel use altogether would be the obvious solution to curb global warming, but it is not that straightforward. There must be sufficient alternative energy sources to sustain the growing global energy demand (Trainer, 2007). Moreover, some countries are reluctant to switch from fossil fuels to sustainable energy sources for several reasons. Firstly, the transition to a sustainable energy system comes at a high financial cost. Secondly, not all sustainable energy methods are proven to work adequately on larger scales. And lastly, some of the proposed sustainable energy methods require a significant surface area, which many countries do not have (Haikola et al., 2019; Siddi, 2016). Curbing global warming is also challenging, because it is difficult to reduce emissions in some sectors. For example, in the cement industry, part of the CO_2 emission is caused by the production process itself (Paltsev et al., 2021; Thakuri et al., 2021). For this reason, several countries, e.g. Norway, invest in methods such as Carbon

Capture and Storage (CCS). CCS is a technique to remove 85 to 95% of the CO_2 from combustion emissions (Scott et al., 2013). Limiting global warming to less than 2 °C by the year 2050 while using fossil fuels as an energy source is only possible when CCS is applied (IPCC, 2014). The most common CCS method is amine-based post-combustion carbon capture (PCCC). This method removes CO_2 from flue gas before it reaches the atmosphere by washing the flue gas with an aqueous amine solution in an absorber column. CO_2 is acidic and binds to the basic amine, resulting in the formation of a salt in aqueous solution. This solution is then transported and heated to 120 °C in a desorber column. The heating process causes the salt to separate again, after which the amine can be re-used and the CO_2 can be stored (Gibbins & Chalmers, 2008; Reynolds et al., 2012). One of the countries investing in CCS is Norway. Their Longship project aims to store large amounts of CO_2 3,000 m below the North Sea seabed, in order to help Norway and Europe reach their climate goals (CCS Norway, 2022).

CCS does, however, have a few drawbacks. The process requires energy, and therefore increases the need for fossil fuels (Scott et al., 2013). Moreover, the aqueous amine solution undergoes oxidative and thermal degradation during the PCCC process. As a result, the solution needs to be renewed or reclaimed. Finally, an important environmental consequence of amine-based PCCC is that some of the amines enter the atmosphere during the process (McDonald et al., 2014; Nielsen, Herrmann, et al., 2012).

1.1 The Atmospheric Impact of Amine-Based Post-Combustion Carbon Capture

Amines are highly reactive and undergo photo-oxidation forming nitrosamines and nitramines, which are carcinogenic compounds. Nitrosamine and nitramine formation at the carbon capture and storage plant is the result of NO_x reacting with emitted amines. In the daytime, the most important oxidant in this photo-oxidation is the hydroxyl radical (OH), which abstracts a hydrogen atom from the amine. The formed amine radical can then react with NO or NO_2 forming nitrosamines or nitramines (see Figure 1). Because of the dependence on OH, the formation of nitrosamines and nitramines is expected to be highest where the OH concentration is greatest. However, some of the amines can already form nitrosamines in the amine plant itself, leading to a direct emission (De Koeijer et al., 2013; Manzoor et al., 2017; Mazari et al., 2019; Nielsen, Herrmann, et al., 2012; Onel et al., 2014; Ravnum et al., 2014; Thompson et al., 2019; Tønnesen, 2011). Stable nitrosamines and nitramines are formed from secondary amines.

Primary amines form unstable nitrosamines, due to the low electron density surrounding the nitrogen atom. However, primary amines can form stable nitramines. Absence of a hydrogen atom prevents tertiary amines from directly forming nitrosamines or nitramines. Primary and tertiary amines can, however, indirectly lead to the formation of stable nitrosamines. Moreover, tertiary amines can also indirectly form stable nitramines. There are many different pathways to form stable nitrosamines from secondary amines, depending on the amine solution used, environmental conditions (e.g. the actinic flux), the presence of oxidizing radicals (e.g. OH) and ambient NO_x concentrations (Chandan et al., 2013; De Koeijer et al., 2013; Mitch, 2019; Nielsen, D'Anna, et al., 2012; Thompson et al., 2019; Voice et al., 2015). Because of the possible health risks related to nitrosamines and nitramines, the Norwegian Institute of Public Health has set the limit of nitrosamines and nitramines at a yearly average of 0.3 ng/m^3 (Norwegian Institute of Public Health, 2016).

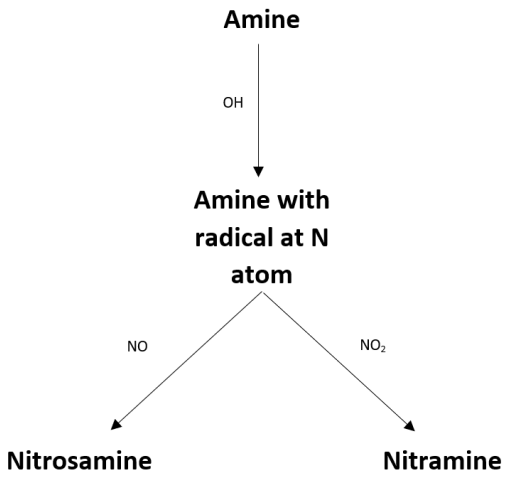

Figure 1: A simplified visual representation of the reactions involved in nitrosamine and nitramine formation from amines emitted during the amine-based carbon capture process.

1.2 Atmospheric Chemistry in a Combustion Plume

Since both nitrosamines and nitramines are secondarily formed in the atmosphere via the reaction with OH radicals, it is important to understand which chemical processes influence the concentration of OH radicals in a combustion plume in the atmosphere.

About 95% of the NO_x from combustion plants is emitted as NO and 5% as NO_2 (Scottish Environment Protection Agency, 2013; Vilà-Guerau de Arellano et al., 1990). The emitted NO_2 can react with atomic oxygen (O) forming NO and molecular oxygen (O_2), as is shown in R1 (Shiekh et al., 2016). However, under influence of radiation, the emitted NO_2 can also produce

NO and O, as shown in R2. O is a precursor for ozone (O_3) production in the troposphere, as shown in R3 (Cheng et al., 1986; Whalley et al., 2010). Here O reacts in a three-body reaction with O_2 and another molecule (M, usually molecular nitrogen (N_2)) forming O_3. Under influence of radiation, O_3 dissociates back to O or to an excited oxygen atom ($O(^1D)$) depending on the radiation wavelength, as shown in R4 and R5 (Hewitt, 2001; Lu & Khalil, 1992; Vilà-Guerau de Arellano et al., 2015). The formed $O(^1D)$ is most often deactivated to the ground state by collision with another molecule (M), as shown in R6. However, a small fraction can react with water forming the hydroxyl radical (OH), which is shown in R7 (Hewitt, 2001; Vilà-Guerau de Arellano et al., 2015).

The NO emitted by combustion sources is of great importance in atmospheric chemistry as well. Especially near the source, where the NO concentration is high, it leads to ozone titration. Ozone titration is a process in which the emitted NO reacts with the O_3 present in the atmosphere, forming NO_2 and O_2, as shown in R8 (Cheng et al., 1986). Since most of the NO_x emitted is NO, the ozone titration process is dominant near the source and almost all O_3 near the source is removed. Thus, when the O_3 concentration near the source is reduced as a result of ozone titration, the formation of OH from O_3 (R5 and R7) is reduced near the source as well (Kim et al., 2016; Kim et al., 2017; Springston et al., 2005; Tønnesen, 2011; VanLoon, 2017). When the plume travels further through the air, the NO concentration becomes diluted with the background air as a result of turbulence (Karamchandani et al., 2002; Seinfeld & Pandis, 2016). Consequently, less O_3 is used in the reaction with NO (R8) and more OH is produced (R5 and R7) further away from the source than near the source (Chowdhury et al., 2015; Luria et al., 1999). This means that further away from the source, the plume contains increasing concentrations of OH and O_3 and decreasing concentrations of NO and NO_2 (Brock et al., 2002; Karamchandani et al., 2000; Karamchandani et al., 2002; Karamchandani et al., 2020; Kim et al., 2017; Zaveri et al., 2003).

Towards the edges of the plume, O_3 formation relative to the ambient O_3 volume mixing ratio (VMR) is also expected to occur (Gillani et al., 1998; Kim et al., 2016; Luria et al., 1999; Ryerson et al., 2001). O_3 production in the troposphere depends on NO_x and Volatile Organic Compound (VOC) concentrations (Kim et al., 2016; Ryerson et al., 1998; Ryerson et al., 2001; Springston et al., 2005; Zaveri et al., 2003). The United States Environmental Protection Agency describes VOCs as “any compound of carbon, excluding carbon monoxide, carbon dioxide, carbonic acid, metallic carbides or carbonates, and ammonium carbonate, which

participates in atmospheric photochemical reactions" (United States Environmental Protection Agency, 2022b). VOCs are emitted from various sources, e.g. vegetation, industrial solvents, pesticides or building materials (United States Environmental Protection Agency, 2022a; Vilà-Guerau de Arellano et al., 2015). Species such as OH, O_3, nitrate (NO_3) and chlorine (Cl) can oxidize VOCs, thereby producing peroxy radicals (RO_2). RO_2 can react with NO forming other peroxy radicals and NO_2. The formed NO_2 can then, under influence of radiation, produce NO and O (R2). Subsequently, the formed O can react with O_2 forming O_3 (R3) (Brasseur & Jacob, 2017; Brune et al., 2016; Khan et al., 2015). Important peroxy radicals are: the hydroperoxy radical (HO_2), the methylperoxy radical (CH_3O_2) and the acetylperoxy radical ($CH_3C(O)O_2$). The latter two are formed from organic precursors such as methane (CH_4) or acetaldehyde (CH_3CHO, R9). $CH_3C(O)O_2$ can react with NO forming NO_2 and CH_3O_2 (R10). The formed CH_3O_2 reacts with NO forming NO_2 and HO_2 (R11). Finally, ambient and formed HO_2 react with NO forming NO_2 and OH (R12) (Onel et al., 2017; Yarwood et al., 2021). Towards the plume's edges, the ambient air containing high VOC levels mixes with the diluting NO_x field in the plume. This results in a higher VOC/NO_x ratio at the edge than in the center of the plume and enables formation of O_3 (Gillani et al., 1998; Luria et al., 1999).

OH is an important species in the atmosphere. It plays an important role in, amongst others, VOC oxidation, where O_3 and in turn OH itself (R5 and R7) are formed (Neuman et al., 2016). It is also called the "cleaning agent" of the atmosphere, because it reacts with pollutants during daytime, converting for instance NO_2 into nitric acid (HNO_3, R13). HNO_3 acts as a sink for OH as well as for NO_x and can be easily removed from the atmosphere, e.g. by wet deposition. Consequently, high OH concentrations in the atmosphere reduce the lifetime of NO_x (Brasseur & Jacob, 2017; Janssen et al., 1991; Kim et al., 2017; Vilà-Guerau de Arellano et al., 2015; Zaveri et al., 2003). HO_2 is an important OH precursor contributing significantly to the OH production in the atmosphere. HO_2 can react, for example, with NO (R12), O (R14) or O_3 (R15) forming OH (Albrecht et al., 2019; Chen et al., 2022; Lu & Khalil, 1992; Simonaitis & Heicklen, 1973). HO_2 also indirectly affects the production of O_3 (R12, R2 and R3), which is another precursor for OH (R5 and R7). Besides O_3 and HO_2, HONO is another important source of OH (Martinez et al., 2003). In emission plumes from combustion plants, HONO can either be emitted directly or formed during daytime by the reaction between the emitted NO and the ambient OH (R16) (Neuman et al., 2016). HONO can dissociate back into OH and NO under the influence of radiation, as is shown in R17 (Alicke et al., 2003; Martinez et al., 2003). HONO has a lower dissociation energy than O_3. As a result, its photolysis reaction (R17) takes place

earlier in the day than the photolysis of O_3 (R5). However, because HONO has a relatively short lifetime with peak concentrations occurring in the earliest hours of the morning, it becomes a less important OH source during the day (Alicke et al., 2003). A visual representation of the species and the chemical reactions mentioned above (R1-R17) and their mutual relations is shown in Figure 2.

$$NO_2 + O \rightarrow NO + O_2$$

R1

$$NO_2 + h\nu(\lambda < 420\ nm) \rightarrow NO + O$$

R2

$$O + O_2 + M \rightarrow O_3 + M$$

R3

$$O_3 + h\nu\ (\lambda < 1180\ nm) \rightarrow O_2 + O$$

R4

$$O_3 + h\nu\ (\lambda < 320\ nm) \rightarrow O(^1D) + O_2$$

R5

$$O(^1D) + M \rightarrow O + M$$

R6

$$O(^1D) + H_2O \rightarrow 2\ OH$$

R7

$$NO + O_3 \rightarrow NO_2 + O_2$$

R8

$$CH_3CHO + OH \xrightarrow{O_2} CH_3C(O)O_2 + H_2O$$

R9

$$CH_3C(O)O_2 + NO \xrightarrow{O_2} NO_2 + CH_3O_2$$

R10

$$CH_3O_2 + NO \xrightarrow{O_2} CH_2O + NO_2 + HO_2$$

R11

$$HO_2 + NO \rightarrow OH + NO_2$$

R12

$$OH + NO_2 + M \rightarrow HNO_3 + M$$

R13

$$HO_2 + O \rightarrow OH + O_2$$

R14

$$HO_2 + O_3 \rightarrow OH + 2\ O_2$$

R15

$$OH + NO + M \rightarrow HONO + M$$

R16

$$HONO + h\nu\ (300\ nm < \lambda < 405\ nm) \rightarrow OH + NO$$

R17

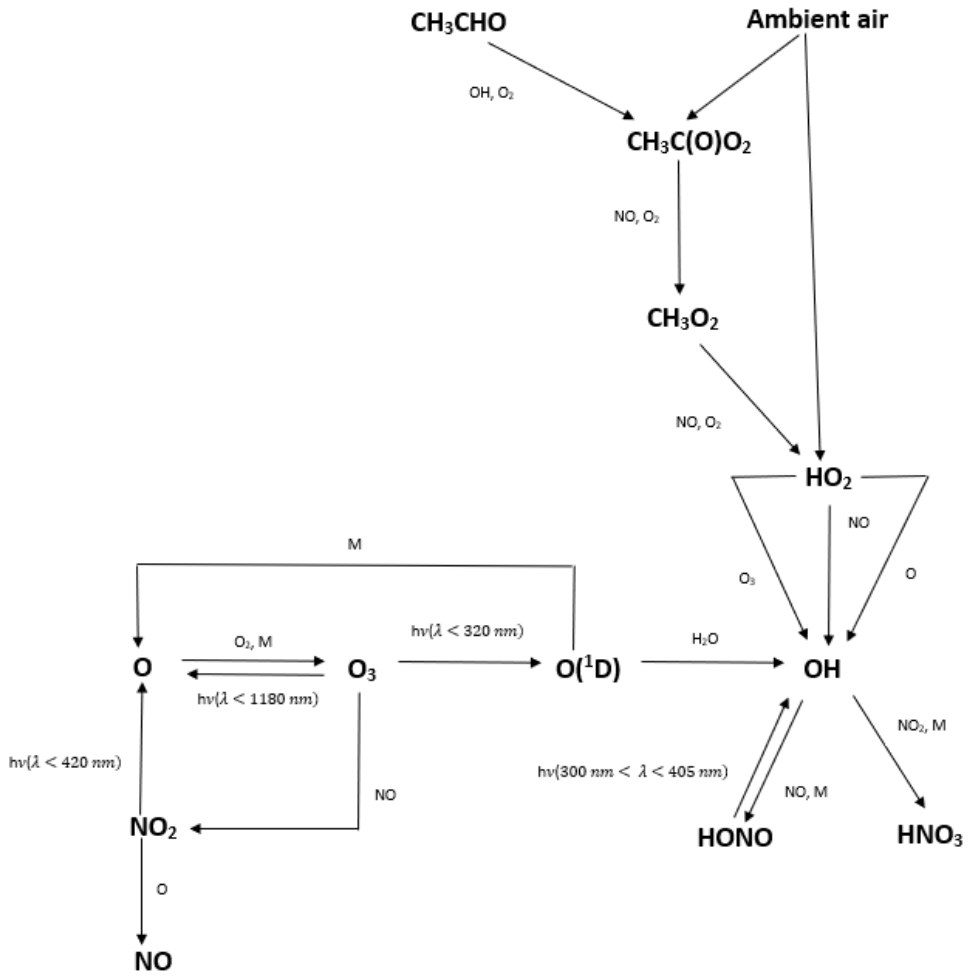

Figure 2: A visual representation of the main species and reactions involved in the NO, NO_2, O_3 and OH chemistry in an emission plume, after emission of NO from a combustion plant stack.

1.3 Atmospheric Chemistry of Piperazine

One of the amine solvents which has been widely studied for application in CCS, is piperazine (PZ, $C_4H_{10}N_2$) (Gaspar et al., 2016; Stowe et al., 2016; Yoon & Hwang, 2022). PZ has been applied in PCCC, for example in the European CESAR (CO_2 Enhanced Separation and Recovery) project, as a mixture with 2-amino-2-methylpropan-1-ol (AMP), also known as the CESAR 1 solvent (European Commission, 2012; Languille et al., 2021). Using concentrated aqueous PZ may result in faster CO_2 absorption, and is therefore also being considered for application in the CCS process (Farmer, 2018; Freeman et al., 2010).

Upon emission, 18% of the PZ is oxidized by OH, forming the piperazine radical which contains a radical at the nitrogen atom (PZNR, $C_4H_9N_2$, R18) (Tan et al., 2021). This radical

can react in several different ways. It can react with O_2 forming HO_2 and the piperazine imine (PZI, $C_4H_8N_2$), as is shown in R19. PZNR can also react with NO_2 forming the piperazine nitramine ($PZNO_2$, $C_4H_9N_2NO_2$), as is shown in R20. $PZNO_2$ can be oxidized by OH forming several products grouped together as $PZNO_2P$ (R21). Instead of reacting with NO_2, PZNR can also react with NO forming the piperazine nitrosamine (PZNO, $C_4H_9N_2NO$), as is shown in R22. PZNO can either be photolyzed back to PZNR (R23) or be oxidized by OH forming several new products which are grouped together as PZNOP (R24). The remaining 82% of PZ reacts with OH forming a radical at the carbon atom (PZCR, $C_4H_9N_2$), as can be seen in R25. O_2 can then bind to the radical, forming $PZCO_2$ ($C_4H_9N_2O_2$, R26). One of the oxygen atoms can be abstracted by NO. Subsequently, O_2 can abstract a hydrogen atom, resulting in ring-opening and the formation of the piperazine aldehyde (PZALD, $C_4H_9N_2O$), HO_2 and NO_2 (R27). Since HO_2 is a precursor for OH (R12), both PZI and PZALD formation play an important role in the OH cycle as well (Nielsen, D'Anna, et al., 2012; Onel et al., 2014; Tan et al., 2021). An overview of the piperazine chemical scheme (R18-R27) can be seen in Figure 3.

$$PZ + OH \rightarrow PZNR + H_2O$$

R18

$$PZNR + O_2 \rightarrow PZI + HO_2$$

R19

$$PZNR + NO_2 \rightarrow PZNO_2$$

R20

$$PZNO_2 + OH \rightarrow PZNO_2P$$

R21

$$PZNR + NO \rightarrow PZNO$$

R22

$$PZNO + h\nu \rightarrow PZNR + NO$$

R23

$$PZNO + OH \rightarrow PZNOP$$

R24

$$PZ + OH \rightarrow PZCR + H_2O$$

R25

$$PZCR + O_2 \rightarrow PZCO_2$$

R26

$$PZCO_2 + NO + O_2 \rightarrow PZALD + HO_2 + NO$$

R27

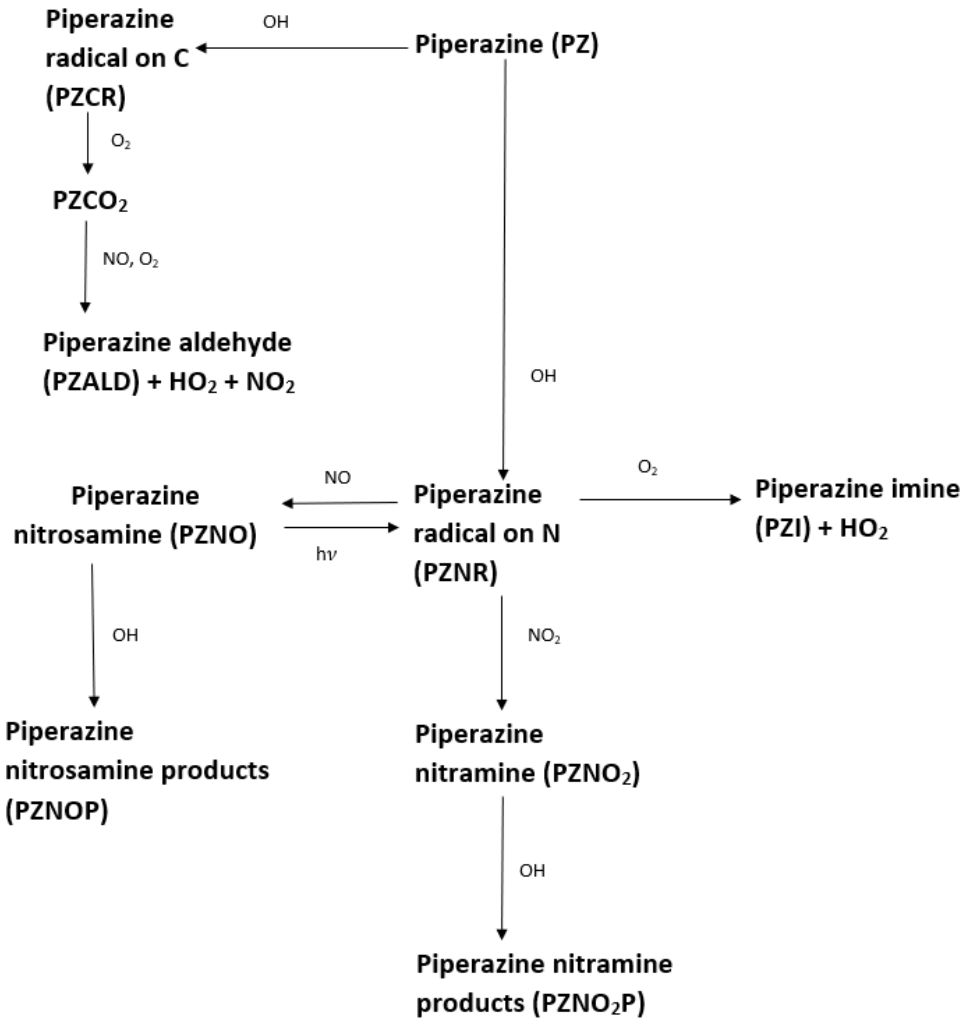

Figure 3: A visual representation of the main species and reactions involved in the piperazine (PZ) chemistry scheme after emission of piperazine from a combustion plant stack.

1.4 Reactive Plume Models

Computer models can be employed to simulate concentrations of chemical species caused by emission and can thus predict whether concentrations will exceed guideline values (Brasseur & Jacob, 2017). Conventional dispersion models do not take actual reactions and reaction rates into account, but use a scaling factor to determine the concentration of species at different points in time and space (Hennig et al., 2016). Generally, air quality modelling uses a grid to depict the atmosphere (Karamchandani et al., 2002). Grid-based chemical transport models with a coarse grid cannot simulate concentration gradients close to the source (Karamchandani et al., 2011). Both of these models do not accurately consider how the NO emitted from a combustion plant stack reacts with O_3 and thereby depletes the O_3 near the source (R8). As a result, such

models tend to under- or overestimate the OH concentration near the source, and thus the atmospheric reactions with OH that take place near the source (Brown & Bilger, 1998; Georgopoulos & Seinfeld, 1986; Kim et al., 2017). Consequently, these models may predict unrealistic nitrosamine and nitramine levels near CCS facilities, which may result in incorrect assessments (Manzoor et al., 2014).

Reactive plume models include non-linear chemistry, because it is not sufficient to work with average chemical (conversion) rates. Moreover, reactive plume models take into account that pollutants do not mix with the ambient gases immediately after emission, but only after reaching a certain, time-dependent, distance away from the source (Georgopoulos & Seinfeld, 1986). Typically, reactive plume models are used for simulating impacts within a 200 km radius from one or more point sources, e.g. the environmental impacts of power plants (Karamchandani et al., 2000). Reactive plume models often include conserved scalars, which are independent of chemical reactions. These scalars can be used to determine the degree of mixing between the emitted and ambient gases (Brown & Bilger, 1998).

Georgopoulos and Seinfeld (1986) made a classification of the different types of reactive plume models based on how mixing is included in the model. Class 1 models assume that the initial dispersion volume is reduced, due to the emissions by a point source, which have a smaller resolution than the computational grid. Models of this class do not take concentration fluctuations within a single grid cell into account. Class 2 models assume that the plume emitted from a stack has a non-mixed center. Around the center, the plume is well-mixed with the surrounding background. The size of the center is inversely related to the distance from the source. The further away from the source, the better mixed the plume becomes, resulting in a smaller non-mixed center. Mixing is assumed to depend on mixing rate constants and the concentration of the unmixed reactants. Class 3 models combine the reduced initial dispersion volume from class 1 models and the concentration fields with a non-mixed center from class 2 models. Class 3 models can be divided into two sub-classes. Class 3A assumes that the growing plume volume can be divided into boxes that increase in size. Each of these boxes contains a well-mixed concentration field and includes slow chemistry to avoid fine scale turbulent fluctuations. Class 3B models do not consider concentration fluctuations. Instead, they assume that the plume contains a Gaussian concentration field. The transport of conserved scalars is used in combination with equilibrium reactions to find concentration profiles of the species of interest. Class 4 models do not include mean concentration gradients. Instead, they apply

turbulent fluctuations to the nonlinear chemistry within a homogenous atmospheric volume. Class 5 models use higher order closure schemes to include fine scale fluctuations into the mean field gradients. And finally, class 6 models use probability densities to describe the macro- and micro-mixing and determine, at least in principle, the complete chemical system, thereby creating a situation that resembles reality as accurately as possible (Georgopoulos & Seinfeld, 1986).

There are many different reactive plume models available, such as the California Puff (CALPUFF) dispersion modelling system, the Turbulent Reacting Plume Model (TRPM), the Reactive and Optics Model of Emissions (ROME) and the Panache Réactif en Atmosphère avec Dépôts (PARADE) model, and new models are continuously being developed (Abdul-Wahab et al., 2011; Joos et al., 1967; Karamchandani et al., 2000). However, many of these models have shortcomings in how chemistry is included or how physical phenomena are represented. For example, ROME is a steady-state model which can only include one emission source and is not able to account for differences in wind speed and/or direction within a short range of distance (Federal Aviation Administration, 2008; Karamchandani et al., 2000). CALPUFF, on the other hand, is a non-steady state puff dispersion model which applies a very simplified chemistry scheme (Karamchandani et al., 2000).

1.5 Aim of the Project

The dispersion models that are currently used for environmental impact assessments on amine-based carbon capture plants do not take into account the detailed chemical transformation process that occurs in the plume of a carbon capture plant. Often a scaling factor is used to determine atmospheric concentrations (Georgopoulos & Seinfeld, 1986; Kim et al., 2017). However, this may lead to an over- or underestimations of NO, NO_2, O_3 and OH concentrations in the plume emitted by a carbon capture facility. Because OH and NO_x can react with amines forming the carcinogenic compounds nitrosamines and nitramines, unrealistic simulations may lead to an over- or underestimation of associated health risks (De Koeijer et al., 2013).

Therefore, the main aim of this project was to explore the atmospheric chemistry that occurs in combustion plumes, without and with amines. For this purpose, a reactive plume model (SCICHEM, EPRI (2021)) was used. In addition, exploratory results were obtained with the Volumetric Particle Approach (VPA) model (Cassiani (2013)) that is currently under development by Dr. Massimo Cassiani from the Norwegian Institute for Air Research (NILU).

2 Methods

The majority of the plume simulations in this project were carried out with SCICHEM, a free open source model (EPRI, 2021; Karamchandani et al., 2020). In addition, Dr. Massimo Cassiani (NILU) provided exploratory results from his Volumetric Particle Approach (VPA) model (Cassiani, 2013). These models can be classified according to the system by Georgopoulos and Seinfeld (1986), as described in section 1.4. The SCICHEM (section 2.1) and the VPA (section 2.2) models are classified as a class 5 and a class 6 model, respectively (Georgopoulos & Seinfeld, 1986). Both models are Lagrangian models, as they simulate air parcels moving with the local wind (Brasseur & Jacob, 2017; Cassiani, 2013; Karamchandani et al., 2000). The concentrations in the parcels are modelled at different points in time and space. Both the SCICHEM and the VPA model use the concept of surplus (deficit) concentration to consider increment (decrease) of the plume concentration with respect to the existing background that is considered separately from the plume (Cassiani, 2013; Karamchandani et al., 2000; Knipping, 2021a). In principle, Lagrangian models can be used for various distances away from the source, from a few meters up to thousands of kilometers, as, contrary to Eulerian models, they are not subject to artificial diffusion (Knipping, 2021a, 2021b). However, Lagrangian models with plume chemistry and explicit modelling of mixing (e.g. SCICHEM and the VPA model) are typically useful within a few tens of kilometers from the source location (United States Environmental Protection Agency, 2017).

Four case studies were carried out in this project. In case study 1 (section 2.3), the SCICHEM results were compared to the results obtained with the Fluidity-Chem model by Zheng et al. (2020). The Fluidity-Chem model has been validated against measurement data and has been shown to capture the details on the plume edges. In case study 2 (section 2.4), the influence of the atmospheric chemical background, the applied atmospheric chemistry scheme and NO emission strength on the chemical evolution of an isolated ship plume was investigated. Subsequently, a simulation was performed for a Waste-to-Energy plant plume. To understand the chemistry in such a plume, the NO, NO_2, O_3 and OH fields were simulated (case study 3a, section 2.5). Finally, a highly reactive amine (piperazine, PZ) was added to the Waste-to-Energy plant plume to simulate the formation of amine breakdown products (case study 3b, section 2.6). Another Waste-to-Energy plant plume simulation was performed (section 2.7) in order to compare the SCICHEM and VPA models. Since the focus of this project is only on the

chemistry within the plume, the meteorology and topography were simplified and kept constant in all simulations.

2.1 SCICHEM Model

SCICHEM is a freely accessible Lagrangian photochemical chemical transport model (EPRI, 2021; Knipping, 2021b). It is based on the Second-order Closure Integrated Puff (SCIPUFF) model, which is expanded with chemistry modules (Karamchandani et al., 2018; Karamchandani et al., 2000; Knipping, 2021b). SCICHEM models an emission plume as a series of puffs, based on the Gaussian puff method (Knipping, 2021a, 2021b). This model is able to simulate the impacts of a single point source in one simulation. However, if there are other point sources that the plume will meet, this information needs to be included in the background concentrations entered into the model. SCICHEM can consider background concentrations that vary over space and/or time. This allows for realistic modelling of the chemical transformation of pollutants, since other possible point sources that may influence the plume chemistry are included in the model as well (Karamchandani et al., 2018; Karamchandani et al., 2020). Moreover, SCICHEM uses varying time steps and output grids. This means that the model determines the time step that is appropriate for the reactions and dispersion occurring in each puff. This prevents the unnecessary use of small time steps. Fitting output fields are also determined by the model. Consequently, grid information and concentration fields do not have to be entered in the model (Knipping, 2021a, 2021b). SCICHEM links the reactive species to a non-reactive tracer. The tracer is used to determine the transport pathway, and the chemical modules are applied to the reactive species to determine chemical transformation (Chowdhury et al., 2015; Karamchandani et al., 2000). Another advantage of SCICHEM is that the model takes the overlapping of puffs into consideration. Otherwise, each overlapping puff would react similarly with the background particles that have already been partially used up by interacting with the previous puff. Therefore, failure to take the overlapping of puffs into account would result in an unrealistically high estimation of the chemical reaction rates (Karamchandani et al., 2018).

SCICHEM divides the power plant plume dispersion into three parts. In the first part, when the plume is close to the emission source (stack), the main reactions taking place are those between NO, NO_2 and O_3. In the second part, when midrange plume dispersion takes place, reactions forming secondary acids are included. And finally in the third part, long-range plume

dispersion, all chemical transformation reactions are used by the model (Karamchandani et al., 2000). SCICHEM has been compared to in-plume field study measurements as well as to the results of other models. This led to the conclusion that SCICHEM is fairly accurate, with a moderate inclination towards over- or underestimation (Karamchandani et al., 2018; Karamchandani et al., 2020).

To model and plot plumes using SCICHEM, the SCICHEM Graphical User Interface (GUI) included in the download files for SCICHEM version 3.3 was used (EPRI, 2021). The GUI has, however, not been updated since the release of SCICHEM version 2.0, but is still suitable for creating simple projects (Knipping, 2021b). Chemical parameters (e.g. species type and gas deposition velocity), atmospheric parameters (e.g. wind speed and direction), and release scenario parameters (e.g. exit velocity and stack height) can be entered in the GUI prior to running the model and plotting the plume. An overview of the parameters needed and the specific input values for the cases described below (section 2.3-2.7) can be found in Table 12 to Table 15 in Appendix 1. To all SCICHEM simulations, operational boundary layer and large-scale variability were applied. This means that SCICHEM internally sets them based on the other input information (Knipping, 2021b).

2.2 Volumetric Particle Approach Model

In the Volumetric Particle Approach (VPA) model every single particle is treated like a box model and information is exchanged between the different boxes (Cassiani, 2013). Each individual box then applies the chemistry as well as all other processes that naturally occur in the atmosphere. The motion of the particles depends on the meteorological field determined by a meteorological model, while the turbulent dispersion is simulated based on stochastic differential equations (Cassiani et al., 2013; Thomson, 1987). Since the particles in the plume interact, a mixing module is included in the model to account for mixing between the particles. The mixing is simulated by the “interaction by exchange with the mean” model (Cassiani et al., 2020; Cassiani et al., 2013; Pope, 1985). However, the VPA model uses several approximations for the mixing process between the plume and background, whereas other probability density function transport models actively simulate the background particles (Cassiani, 2013; Cassiani et al., 2020; Cassiani et al., 2005; Pope, 1985). Still, an important advantage is that a considerable amount of computational time is saved by not modelling background particles (Cassiani, 2013). Different and adaptable time steps are used for simulating particle dispersion,

the mixing process and advancing the chemistry. The background chemistry and the plume chemistry are treated separately and combined afterwards. The background chemistry is currently advanced on the three-dimensional Eulerian, grid based, model EPISODE (Hamer et al. (2020)) using a horizontal grid resolution of 1 km^2. The plume appears as a source term in the Eulerian model when the edge of the Lagrangian model domain is exceeded. Since the VPA model is still at the early development stage, it was not yet ready to be run by non-experts. The VPA model was thus run by Dr. Massimo Cassiani. The output of the VPA model consists of time and space averaged concentrations over a certain height and horizontal grid. These averages are obtained by sampling the particle field pertaining to each grid averaging element. No amine chemistry is currently included in the VPA model that was therefore only used for studying the NO_x, O_3 and OH chemistry. The chemical scheme used in the VPA model in this preliminary study is a simplified EMEP (European Monitoring and Evaluation Programme) scheme as described by Walker et al. (2003) and is included in Figure 43 in Appendix 2 (European Commission, 2019; European Monitoring and Evaluation Programme, 2021). Below, this chemical scheme will be simply referred to as the adapted EMEP chemistry scheme.

2.3 Case Study 1: Power Plant Plume Chemistry Simulations

The aim of case study 1 was to compare the SCICHEM results to the results obtained by Zheng et al. (2020) with the Fluidity-Chem model, which has been shown to capture details at the plume edges (Chowdhury et al., 2015; Zheng et al., 2020). Zheng et al. (2020) simulated a plume emitted from a stack at the Cumberland Power Plant in Tennessee, USA (36 N, 87 W). NO was emitted at 3502.74 g/s at a height of 193.5 m. The wind was assumed to be constant at a speed of 5 m/s and coming from the west (Zheng et al., 2020). All input parameters for the SCICHEM GUI are shown in Table 12 in Appendix 1. The multi-component input file used for these simulations was the SCICHEM multi-component input file “fullchem_ae5_SW” without the ambient file “SW.amb”. Nothing was altered in this file for these simulations. The multi-component input file can be found in the example folder in the SCICHEM version 3.3 download. The fields within the plume were plotted at surface height, since that was the height at which Zheng et al. (2020) plotted their plume fields as well.

2.4 Case Study 2: Ship Plume Chemistry Simulations

In case study 2, an isolated ship plume was simulated. The study by Charlton-Perez et al. (2009) served as a reference point for the simulations, and the conditions mentioned in their work were implemented to simulate NO, NO_2, OH and O_3 in the ship plume. In this case, 33 g/s of NO was emitted from the stack of a typical merchant ship in the North Atlantic Ocean (15 N, 54 W). The wind was assumed constant at a speed of 4 m/s coming from the east. All input parameters entered in the SCICHEM GUI are shown in Table 13 in Appendix 1. The multi-component input file, with the reactions, rate constants and ambient VMRs as used by Charlton-Perez et al. (2009), is shown in Figure 42 in Appendix 2. The ambient VMRs, which were constant throughout the simulation, are also shown in Table 1. The ambient VMRs of OH, NO_2 and O_3 were taken from the Charlton-Perez et al. (2009) study and assumed to be constant in the SCICHEM simulations. Moreover, the ambient VMRs of CO and CH_4 from the full SCICHEM multi-component input file ("fullchem_ae5_SW"; which can be found in the SCICHEM version 3.3 download) were used, as Charlton-Perez et al. (2009) only stated that these ratios remained constant throughout the simulation and did not mention specific values. The ambient VMR of H_2O was set internally by SCICHEM based on the meteorological input. This was achieved in the simulation by setting the ambient VMR to -1.0 ppm (Knipping, 2021b).

Table 1: Ambient volume mixing ratios (in ppb) from the multi-component file (Figure 42 in Appendix 2) that were used in the SCICHEM simulation of an isolated ship plume based on the paper by Charlton-Perez et al. (2009). ^{A}*: an ambient* H_2O *VMR of* $-1.0 \cdot 10^3$ *indicates that the actual ambient VMR used in the SCICHEM simulation is determined internally based on the meteorological input.*

Species	Ambient VMR
NO_2	0.1
O_3	27
OH	$3.66 \cdot 10^{-4}$
CH_2O	0.1
CH_3OOH	0.1
H_2O_2	0.1
CO	$2.20 \cdot 10^2$
H_2O^A	$-1.0 \cdot 10^3$
CH_4	$1.945 \cdot 10^3$

2.4.1 Effect of Different Chemistry Schemes

The atmospheric chemistry schemes used for the simulations were the full SCICHEM chemistry multi-component input file ("fullchem_ae5_SW" given in the examples folder of SCICHEM version 3.3) and an adapted EMEP chemistry scheme provided by NILU (see Figure 43 in Appendix 2). Compared to the scheme used in the full SCICHEM chemistry multi-component input file, the adapted EMEP chemistry scheme is a simplified chemistry scheme. However, it is more elaborate than the chemistry scheme used by Charlton-Perez et al. (2009). All ambient VMRs were altered to match those of Charlton-Perez et al. (2009) as described in Table 1 above. Ambient VMRs of species were set to 0 ppm, if mentioned in the adapted EMEP or the full SCICHEM chemistry multi-component input file, but not in Table 1. The effect of different chemistry schemes was only determined within 30 km downwind from the source.

2.4.2 Effect of Different Background Conditions

In order to understand the impact of the different atmospheric background conditions on the NO_x, O_3 and OH fields, the simulation with the full SCICHEM multi-component input file ("fullchem_ae5_SW") was repeated. After the simulation using the ambient levels provided by Charlton-Perez et al. (2009) given in Table 1 above, a simulation was executed without adding an ambient file, resulting in the use of the default ambient VMRs from the full SCICHEM multi-component input file. Then a simulation was performed with the ambient file "FL.amb", which contains the background conditions for Florida. After this, a simulation was performed using the "WA.amb" ambient file, containing the background conditions for the state of Washington. Both ambient files can be found in the sciData folder within the binary folder of the SCICHEM version 3.3 download. Finally, NILU-provided ambient VMRs (Table 16 in Appendix 3) were implemented in the full SCICHEM multi-component input file. All ambient VMRs for the species not included in the NILU-provided ambient levels, but included in the full SCICHEM multi-component input file, were set to 0 ppm. When the default, NILU-provided or Charlton-Perez et al. (2009) ambient VMRs were used, these mixing ratios were constant during the day. The Florida and Washington State ambient files, however, contain ambient VMRs that vary diurnally (Knipping, 2021b). Table 2 shows the different background VMRs at local noon, for NO, NO_2, O_3, OH, HO_2 and $CH_3C(O)O_2$ for the different backgrounds. The distance of interest was once again limited to 30 km downwind from the source.

Table 2: Background volume mixing ratios of NO, NO_2, O_3, OH, HO_2 and $CH_3C(O)O_2$ used for five simulations of the ship plume. The multi-component input file "fullchem_ae5_SW" was used with the ambient volume mixing ratios of Charlton-Perez et al. (2009) as described in Table 1, the default volume mixing ratios from the multi-component file, Florida ("FL.amb"), Washington State ("WA.amb") and NILU-provided background conditions (Table 16 in Appendix 3).

	NO (ppt)	**NO_2 (ppt)**	**O_3 (ppb)**	**OH (10^6 molec. cm^{-3})**	**HO_2 (ppt)**	**$CH_3C(O)O_2$ (ppt)**
Charlton-Perez et al. (2009)	0	100	27	9	0	0
Default	28	2400	63	0.08	6.89	3.13
FL.amb	66.8	3731	33	0.08	6.89	3.13
WA.amb	10.55	1361.2	27.5	0.08	6.89	3.13
NILU	167	561	34.4	7.48	10.6	0.35

2.4.3 Effect of Reduced NO Emission on the OH Field

The NO emission was decreased by a factor of 10 (from 33 g/s to 3.3 g/s) to determine the effect of this reduction on the OH field. This was done using the full SCICHEM multi-component input file ("fullchem_ae5_SW" without the ambient file "SW.amb"), the Charlton-Perez et al. (2009) multi-component input file (Figure 42, in Appendix 2) and the multi-component input file containing the adapted EMEP chemistry scheme (Figure 43 in Appendix 2). In all of these files, the ambient VMRs were replaced by the ratios included in Table 1, while the ambient VMRs of species not mentioned in Table 1 were set to 0 ppm. Similarly to section 2.4.1 and 2.4.2, the distance of interest was limited to 30 km downwind from the source.

2.5 Case Study 3a: Waste-to-Energy Plant Plume Chemistry Simulations (without Amines)

In this case, the WtE plant's NO emission at a stack height of 80 m was assumed to be, on average, 3.02 g/s and the amount of NO_2 emitted was neglected. Appendix 4 contains the conversion from volume mixing ratio (in ppm) to the flue gas emission rates (in g/s). The wind speed was assumed to be constant (4 m/s) and coming from the southeast (135°). The input parameters for the SCICHEM GUI are shown in Table 14 in Appendix 1. The multi-component input file that was used for these simulations was the SCICHEM multi-component input file "fullchem_ae5_SW" without the ambient file "SW.amb". The ambient VMRs were replaced in the multi-component input file by the NILU-provided ambient levels (Table 16 in Appendix 3).

Ambient levels for species that are included in the multi-component input file, but not in the NILU-provided ambient conditions, were set to 0 ppm.

2.5.1 Effect of Chemistry on the OH Field

To understand the underlying chemistry of the OH field, in particular near the source, changes were made in the multi-component input file by removing the reactions that are involved in OH production or depletion one by one.

2.5.2 Effect of Different Emissions on the OH Field

Five other emission scenarios were simulated:

i) The NO emission was increased by a factor of 10 to 30.2 g/s to find the effect on the corresponding OH field.

ii) A simulation was performed where in addition to an NO emission of 3.02 g/s, $3.02 \cdot 10^{-2}$ g/s (1%) NO_2 was emitted.

iii) A simulation was run with a HONO emission of $3.02 \cdot 10^{-3}$ g/s (0.1%) added to the NO and NO_2 emissions.

iv) The two above-mentioned simulations with NO_2 and HONO emissions were repeated using an NO emission of 30.2 g/s whilst keeping the NO_2 and HONO emissions at respectively 1% and 0.1% of the NO emission.

v) In addition to NO (both 3.02 g/s and 30.2 g/s), 0.016 g/s of acetaldehyde (CH_3CHO) was emitted.

All conversions from volume mixing ratios (in ppb) to emission rates (in g/s) can be found in Appendix 4.

2.6 Case Study 3b: Waste-to-Energy Plant Plume Chemistry Simulations (with Amines)

After running the SCICHEM model to simulate NO, NO_2, OH and O_3 fields in the combustion plume (section 2.5), emission of the amine piperazine (PZ) was included in the second run. This

was done by adding R18 to the multi-component input file ("fullchem_ae5_SW" without the ambient file "SW.amb"), where PZNR is the piperazine radical with the radical at the N atom (Onel et al., 2014; Tan et al., 2021). The formation of the piperazine imine (PZI, R19), the piperazine nitramine ($PZNO_2$, R20) and nitrosamine (PZNO, R22) and secondary reactions with OH forming new products ($PZNO_2P$, R21 and PZNOP, R24) were subsequently included, as well as the photolysis reaction of PZNO (R23). A photolysis rate of $0.34 \cdot J_{NO_2}$ was used, where J_{NO_2} is the default NO_2 photolysis rate from the multi-component input file. A secondary PZ oxidation pathway was added, where PZ reacts with OH forming a radical in the C position: PZCR (R25). The reactions by which PZCR forms $PZCO_2$ (R26) and PZALD (R27) were added as well. For simplicity, R25 and R26 have been grouped together into a single reaction (Nielsen, D'Anna, et al., 2012; Tan et al., 2021). All reaction rate constants and the photolysis rate are shown in Table 3. As in case study 3a (section 2.5), the ambient VMRs were replaced in the multi-component input file by the NILU-provided ambient levels (see Table 16 in Appendix 3). An ambient VMR of $3 \cdot 10^{-8}$ ppm was used for PZ. For all other species involved in the PZ chemistry scheme as shown in R18-R27 (i.e. PZNR, PZI, $PZNO_2$, $PZNO_2P$, PZNO, PZNOP, PZCR, $PZCO_2$, PZALD) an ambient VMR of $3 \cdot 10^{-10}$ ppm was used. The background levels of all species present in the multi-component file but not included in the NILU-provided background (Table 16 in Appendix 3) were set to 0 ppm. It was assumed that there would be no deposition for any of the species involved in the PZ chemistry scheme (European Chemicals Bureau, 2005; National Library of Medicine *National Center for Biotechnology Information*, 2022).

Two emission scenarios were considered:

i) Besides the emission of NO (i.e. 3.02 g/s or 30.2 g/s) and CH_3CHO (0.016 g/s), a total PZ emission of 0.032 g/s was used. In order to take into account that only 18% of PZ forms nitrosamines and nitramines, two different PZ species (i.e. PZA and PZB) were emitted with the exact same parameters. PZA was emitted corresponding to 18% of the total PZ emission (i.e. 0.006 g/s), to take part in R18-R24. PZB was emitted corresponding to 82% of the total PZ emission (i.e. 0.026 g/s) to take part in R25-R27 (Tan et al., 2021).

ii) Since PZNO can also be directly released from the stack, a simulation was performed in which $2.1 \cdot 10^{-4}$ g/s PZNO was released in addition to 3.02 g/s NO, 0.016 g/s CH_3CHO and

0.032 g/s PZ. The conversions from volume mixing ratios (in ppm and ppb) to emission rates (in g/s) are detailed in Appendix 4.

$$PZ + OH \rightarrow PZNR + H_2O$$

R18

$$PZNR + O_2 \rightarrow PZI + HO_2$$

R19

$$PZNR + NO_2 \rightarrow PZNO_2$$

R20

$$PZNO_2 + OH \rightarrow PZNO_2P$$

R21

$$PZNR + NO \rightarrow PZNO$$

R22

$$PZNO + h\nu \rightarrow PZNR + NO$$

R23

$$PZNO + OH \rightarrow PZNOP$$

R24

$$PZ + OH + O_2 \rightarrow PZCO_2 + H_2O$$

R25 + R26

$$PZCO_2 + NO + O_2 \rightarrow PZALD + HO_2 + NO$$

R27

Table 3: Chemical kinetics parameters in the piperazine chemical scheme (Figure 3, R18-R27). The reaction rates for R25 and R26 have been combined into one reaction rate. J_{NO_2}, as used in the photolysis rate of R23 (J_{23}) is the default NO_2 photolysis rate from the full SCICHEM multi-component input file ("fullchem_ae5_SW").

Reaction Number	**Reaction Rate Constant (cm^3 $molec.^{-1}$ min^{-1})**	**Photolysis Rate**	**Reference**
R18	$k_{18} = 1.5 \cdot 10^{-8}$		Onel et al. (2014), Tan et al. (2021)
R19	$k_{19} = 3.0 \cdot 10^{-18}$		Tan et al. (2021)
R20	$k_{20} = 1.9 \cdot 10^{-11}$		Tan et al. (2021)
R21	$k_{21} = 7.5 \cdot 10^{-9}$		Tan et al. (2021)
R22	$k_{22} = 3.3 \cdot 10^{-11}$		Tan et al. (2021)
R23		$J_{23} = 0.34 \cdot J_{NO_2}$	Tan et al. (2021)
R24	$k_{24} = 7.5 \cdot 10^{-9}$		Tan et al. (2021)
R25 + R26	$k_{25+26} = 1.5 \cdot 10^{-8}$		Onel et al. (2014), Tan et al. (2021)
R27	$k_{27} = 6.0 \cdot 10^{-10}$		Tan et al. (2021)

2.7 SCICHEM and Volumetric Particle Approach Model Comparison

Both the SCICHEM and VPA models were used to perform another simulation of the WtE plant plume. The wind was assumed to vary with height and to come from the west (270°). NO emissions were set to 3.013 g/s at stack height (i.e. 75 m). All input values are given in Table 15 in Appendix 1. The used ambient VMRs and the adapted EMEP chemistry scheme, including rate constants, are given in the multi-component input file shown in Figure 43 in Appendix 2. The VPA model output is height averaged; in this case, an average from surface level to 50 m was generated. Since the SCICHEM GUI is not able to produce a height-averaged output, the fields were plotted at 0, 25 and 50 m height. The wind was assumed to come from the west at a speed of 4.38 m/s, 5.20 m/s and 6.10 m/s at 0, 25 and 50 m height respectively. NO emissions were then increased by a factor of 10 from 3.013 g/s to 30.13 g/s.

3 Results and Discussion

In this section, the results of the different case studies are presented. In case study 1 (section 3.1) SCICHEM is used to simulate NO_x and O_3 in a power plant plume that was previously simulated by Zheng et al. (2020) with the Fluidity-Chem model. The latter is proven to capture the fine details at the plume edges (Zheng et al., 2020). In case study 2 (section 3.2) the influence of the atmospheric chemical background, the applied atmospheric chemistry scheme and NO emission strength on the chemical evolution of an isolated ship plume is investigated (Charlton-Perez et al., 2009). The last two case studies (3a and 3b) include plume chemistry simulations for a WtE plant. In case study 3a (section 3.3) SCICHEM was used to simulate the chemistry in a WtE plant plume without amines being emitted. In case study 3b (section 3.4), piperazine was added to the emission scenario in the SCICHEM simulation. Finally, in section 3.5 the results for a WtE plant plume without amines, obtained using the SCICHEM and VPA models, are compared.

3.1 Case Study 1: Power Plant Plume Chemistry Simulations

Figure 4A and B show the NO_2 and NO fields in the plume of the Cumberland Power Plant in Tennessee obtained using the SCICHEM model with the input parameters given by Zheng et al. (2020). In both fields, the maximum VMR is found near the source, i.e. 72 ppb for NO_2 and 340.7 ppb for NO. The presence of the maximum VMR of NO near the source can be explained by the fact that NO is emitted by the source with 3502.74 g/s. The presence of the maximum VMR of NO_2 near the source can be explained by the reaction between the emitted NO and O_3 forming NO_2 close to the source (see R8). Both fields then gradually decrease back to the ambient VMR of 2.40 ppb (NO_2) and $2.8 \cdot 10^{-2}$ ppb (NO). The NO_2 field (Figure 4A) spans a distance of approximately 75 km, whereas the NO field (Figure 4B) spans a distance of approximately 35 km. This difference can be explained by rapid oxidation of NO to NO_2 in the atmosphere (United States Environmental Protection Agency, 1999). A clear similarity can be seen, when comparing the resulting NO_2 and NO fields to the NO_x field (Figure 4C) modelled by Zheng et al. (2020) using the Fluidity-Chem model. The SCICHEM GUI is neither able to plot NO_x fields, nor to gradually decrease the VMR from 15 to 0 ppb. This means that the NO_2 and NO fields simulated using SCICHEM (Figure 4A-B) need to be added together in order to

be able to compare them to the NO_x field (Figure 4C) simulated by Zheng et al. (2020). Moreover, since it was not possible to set a gradual decrease from 15 ppb down to 0 ppb in the SCICHEM GUI, the fields are less detailed and appear shorter, even though the simulated values actually show an increase compared to the ambient VMR further downwind. The main parts of the fields correspond well, with 54 and 55 ppb at 30 km downwind and 27 and 30 ppb at 60 km downwind from the source in Figure 4A-B and Figure 4C, respectively.

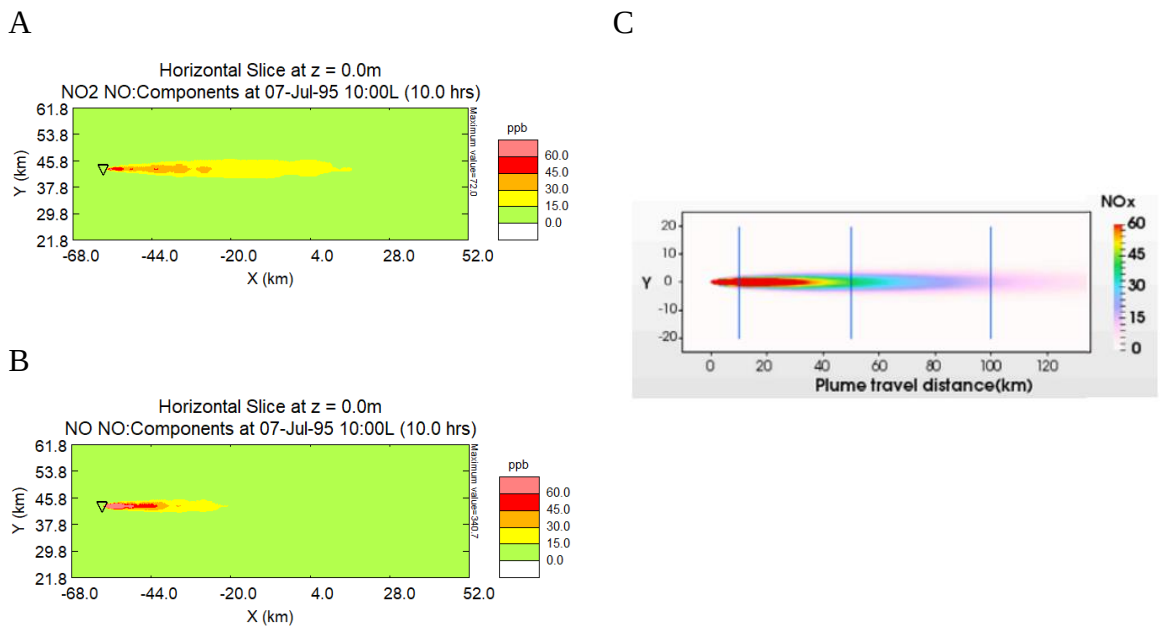

*Figure 4:**A**) NO_2 field modelled with SCICHEM and plotted with the SCICHEM GUI after emission of 3502.74 g/s NO at a stack height of 193.5 m at the Cumberland Power Plant, Tennessee, USA, using the input parameters from case number 1 as presented by Zheng et al. (2020). The emission source is indicated by the symbol ∇. **B**) as in A) but for NO. **C**) NO_x field (in ppb) at the Cumberland Power Plant, Tennessee, USA. Adapted from the NO_x field modelled in case 1 by Zheng et al. (2020): "Emission rate (13.9 ton/h): the spatial distribution of the species NO_x ... (ppbv) at the stable stage (t = 10 hr), with the minimum and maximum adaptive mesh resolutions of 100 m and 20 km respectively, the time step Δt is 400 s."(Zheng et al., 2020). Note: axes in A-B have different values compared to those in C, but they have the same extensions in both South-North (y) and East-West (x) directions.*

Figure 5A shows the O_3 field in the Cumberland Power Plant plume obtained using the SCICHEM model with the input parameters given by Zheng et al. (2020). It shows the depletion of the O_3 VMR near the source. At approximately 20 km downwind from the source, a VMR of 18 ppb is observed. At 40 km downwind, a VMR of 45 ppb and up to 60 km downwind, a mixing ratio of 60 ppb is seen. This depletion pattern is also found in the O_3 field modelled with the Fluidity-Chem model by Zheng et al. (2020) as is shown in Figure 5B. The observed depletion pattern in the O_3 field (Figure 5A) also corresponds to the pattern observed for NO and NO_2 (Figure 4A and B) and can be explained by the reaction between O_3 and NO forming NO_2 (see R8). Figure 5A also shows an increase in the O_3 VMR starting at approximately 100 km downwind. This increase was also observed by Zheng et al. (2020) (Figure 5B) and can

be explained by the fact that the NO is mixed better with the ambient air at that distance downwind. Therefore, this far downwind, and contrary to the atmospheric chemistry closer to the source, not all O_3 formed immediately reacts with NO, resulting in O_3 formation instead of depletion. SCICHEM (Figure 5A) was not able to simulate the "wing-like" pattern of the O_3 formation at the plume edges starting at 20 km downwind as shown in Figure 5B.

A B

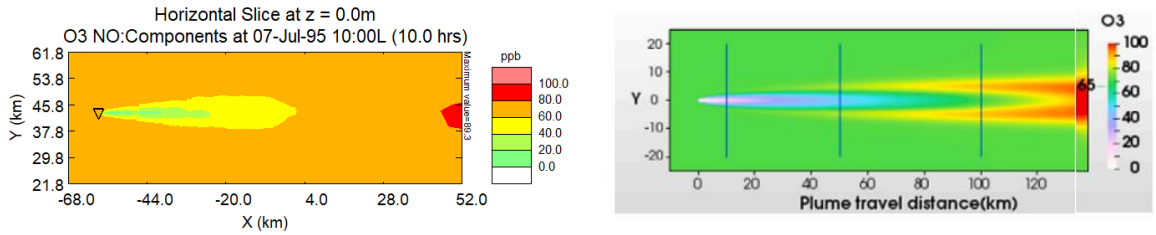

*Figure 5: **A**) O_3 field modelled with SCICHEM and plotted with the SCICHEM GUI after emission of 3502.74 g/s NO at a stack height of 193.5 m at the Cumberland Power Plant, Tennessee, USA, using the input parameters from case number 1 as presented by Zheng et al. (2020). The emission source is indicated by the symbol ∇. **B**) O_3 field (in ppb) at the Cumberland Power Plant, Tennessee, USA. Adapted from the O_3 field modelled in case 1 by Zheng et al. (2020): "Emission rate (13.9 ton/h): the spatial distribution of the species …,O_3, … (ppbv) at the stable stage (t = 10 hr), with the minimum and maximum adaptive mesh resolutions of 100 m and 20 km respectively, the time step Δt is 400 s."(Zheng et al., 2020). Note: the axes in A-B have different values compared to those in C, but they have the same extension both in South-North (y) and East-West (x) directions.*

The model used by Zheng et al. (2020) has been validated against measurement data at the Cumberland Power Plant in Tennessee. It was found that within 66 km of the source, the maximum peak height varied 10 to 20% from the measured values, and further downwind an even better match was found (Zheng et al., 2020). The model used by Zheng et al. (2020) can therefore be considered as an accurate model for the NO, NO_2, O_3 chemistry that is the focus of this research project. Since the results of the SCICHEM simulations adequately correspond with the results presented by Zheng et al. (2020), it can be concluded that SCICHEM works well and applies the chemistry appropriately, despite that some default settings had to be used for meteorological parameters (i.e. surface roughness, precipitation, Bowen ratio, albedo and fractional cloud cover). However, this case study shows that SCICHEM misses some crucial detailing on the edges of the plume. Any O_3 formation towards the plume edges results in OH formation there. And, since OH plays such an important role in atmospheric chemistry, accurate simulation of these details may be important. This emphasizes the need for a model that is able to accurately simulate plume edge details, e.g. the VPA model that will be discussed below.

3.2 Case Study 2: Ship Plume Chemistry Simulations

In this section, the influence of the applied atmospheric chemistry scheme, atmospheric chemical background and NO emission strength on the chemical evolution of an isolated ship plume is investigated. The study by Charlton-Perez et al. (2009) served as an initial reference (simplified atmospheric chemistry scheme and atmospheric chemical background for a ship plume), but due to missing input information (e.g. stack height and measuring height) it was not possible to make a consistent comparison between the SCICHEM results and the results obtained by Charlton-Perez et al. (2009). This comparison is therefore not included in this thesis.

3.2.1 Effect of Different Chemistry Schemes

Figure 6 shows the NO_2 and NO fields simulated using different chemistry schemes and the ambient VMRs by Charlton-Perez et al. (2009) as described in Table 1. Figure 6A shows the fields based on the chemistry scheme used by Charlton-Perez et al. (2009) (Figure 42 in Appendix 2). Figure 6B shows the NO_2 and NO fields based on the full SCICHEM chemistry scheme as included in the multi-component input file "fullchem_ae5_SW". Figure 6C shows the NO_2 and NO fields based on the adapted EMEP chemistry scheme (Figure 43 in Appendix 2). All NO_2 and NO fields show the highest VMR close to the source, which is as expected. NO is emitted by the source and reacts with O_3 to form NO_2 close to the source (R8). However, contrary to simulations employing the other chemistry schemes, when using the adapted EMEP chemistry scheme the NO field spans a longer distance and the NO_2 field a shorter distance (Figure 6C). This difference indicates that less NO is converted to NO_2, which could be the result of different reaction rates being used in the chemistry schemes. Figure 7A-C depict the corresponding O_3 fields, which all show a depletion area spanning approximately 3 km downwind from the source location; this is in line with NO reacting with O_3 close to the source forming NO_2 (R8). Figure 8A-C depict the OH fields, which all show a depletion of OH close to the source as well. Within the first 3 km downwind from the source, total OH depletion can be observed. This corresponds to the O_3 depletions shown in Figure 7A-C, because O_3 is a precursor for OH. Consequently, when no O_3 is present, no OH is formed (R5 and R7). Thus, regardless of the applied chemistry scheme, under the ambient levels as described in Table 1

O_3 and OH depletion is simulated close to the source. However, the OH depletion areas within the first 30 km are different depending on which chemistry scheme is used. For example, when the Charlton-Perez et al. (2009) chemistry scheme (Figure 42 in Appendix 2) is applied, as is shown in Figure 8A, the OH depletion area is longer than in the other two cases depicted in Figure 8B and C. These differences were linked to the different HNO_3 behaviors in the chemistry schemes. The OH depletion areas (Figure 8A-C) span a longer distance downwind from the source than the O_3 depletion areas (Figure 7A-C). OH depletion occurring while there was no O_3 depletion anymore (i.e. after the first 3 km downwind from the source) was found to be the result of the reaction between OH and NO_2 forming HNO_3 (R13).

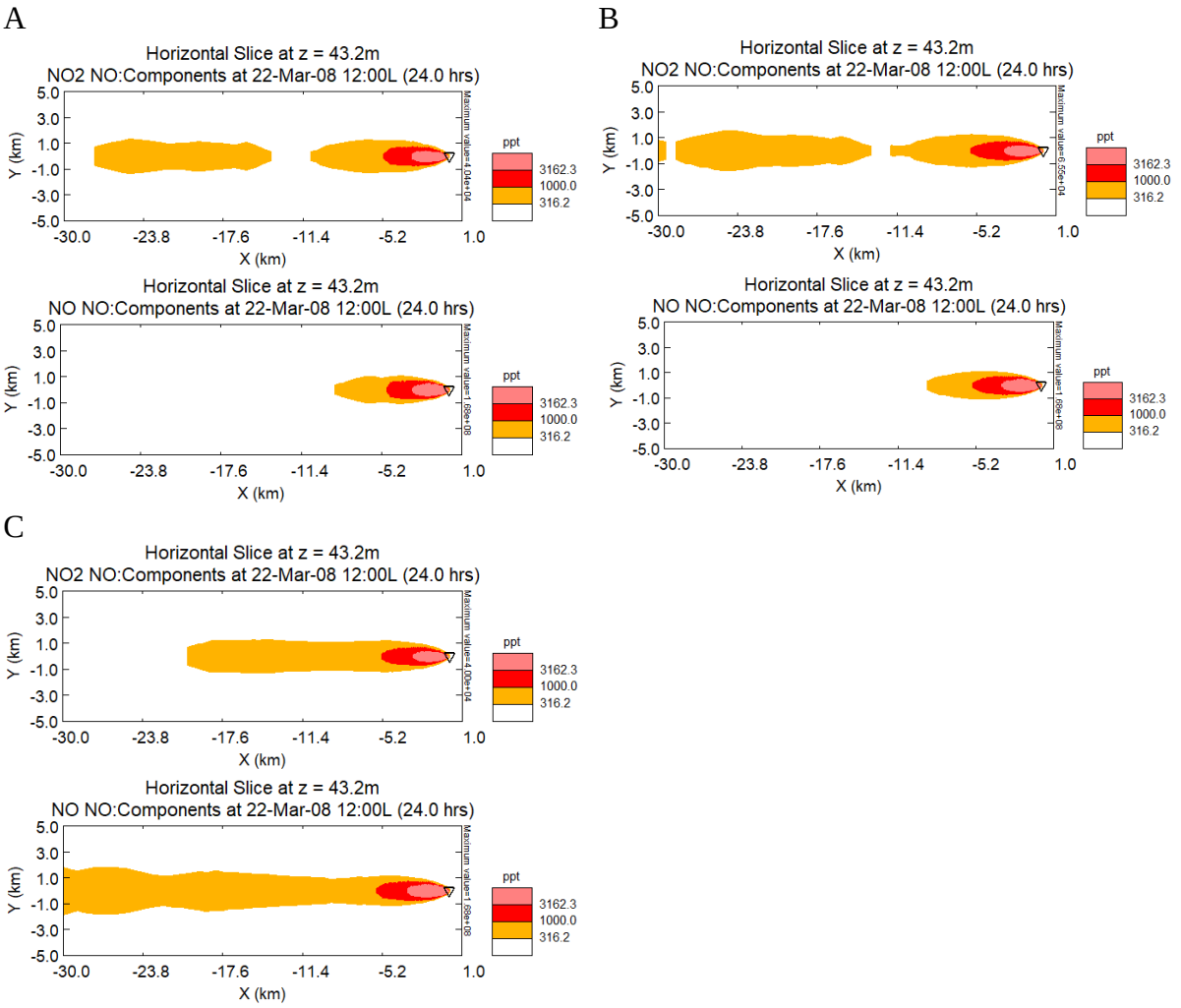

Figure 6: NO_x (NO_2 (top) and NO (bottom)) fields modelled with SCICHEM and plotted with the SCICHEM GUI after emission of 33 g/s NO from a stack with a height of 43.2 m. The source location is indicated by the symbol ∇. Different chemistry schemes were applied, all with the background conditions described by Charlton-Perez et al. (2009) as shown in Table 1. ***A)*** *Charlton-Perez et al. (2009) chemistry scheme (Figure 42 in Appendix 2).* ***B)*** *Full SCICHEM chemistry scheme as included in the multi-component input file "fullchem_ae5_SW".* ***C)*** *Adapted EMEP chemistry scheme (Figure 43 in Appendix 2).*

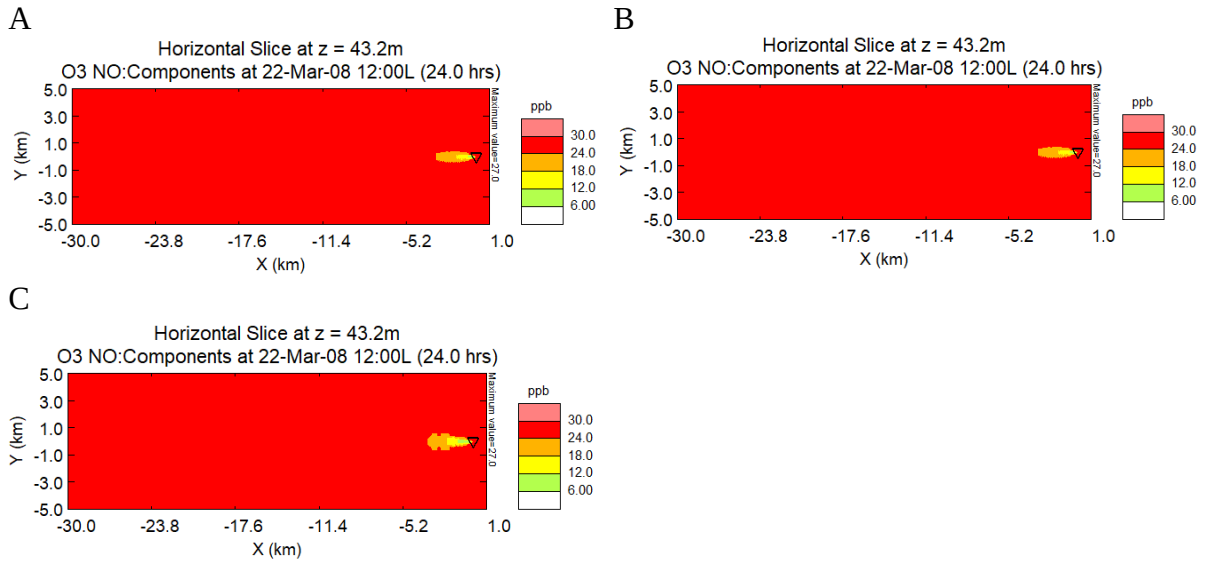

*Figure 7: O_3 fields modelled with SCICHEM and plotted with the SCICHEM GUI after emission of 33 g/s NO from a stack with a height of 43.2 m. The source location is indicated by the symbol ∇. Different chemistry schemes were applied, all with the background conditions described by Charlton-Perez et al. (2009) as shown in Table 1. **A)** Charlton-Perez et al. (2009) chemistry scheme (Figure 42 in Appendix 2). **B)** Full SCICHEM chemistry scheme as included in the multi-component input file "fullchem_ae5_SW". **C)** Adapted EMEP chemistry scheme (Figure 43 in Appendix 2).*

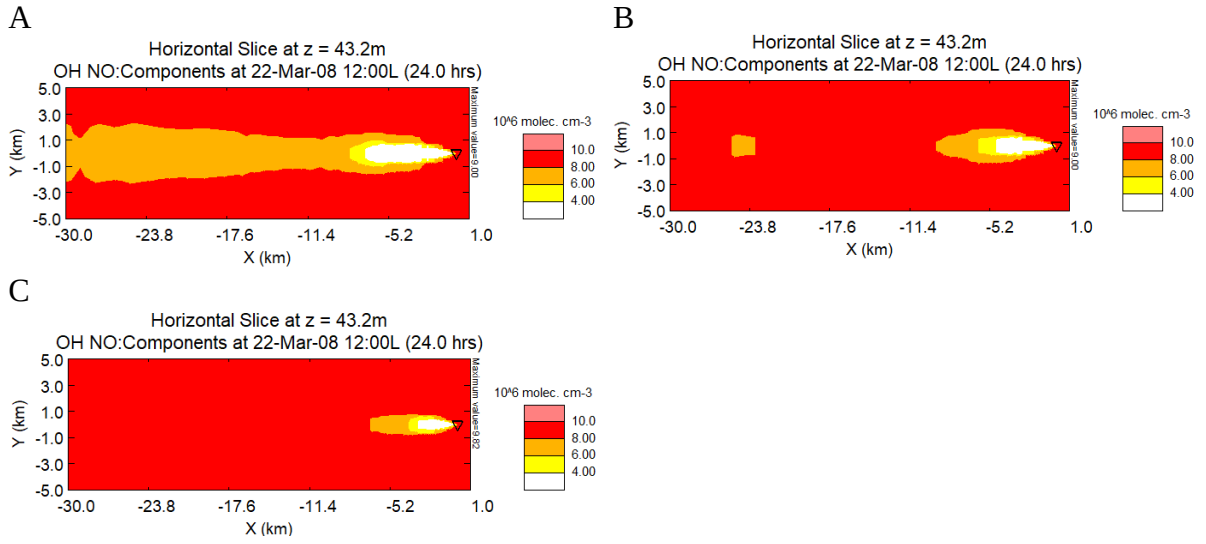

*Figure 8: OH fields modelled with SCICHEM and plotted with the SCICHEM GUI after emission of 33 g/s NO from a stack with a height of 43.2 m. The source location is indicated by the symbol ∇. Different chemistry schemes were applied, all with the background conditions described by Charlton-Perez et al. (2009) as shown in Table 1. **A)** Charlton-Perez et al. (2009) chemistry scheme (Figure 42 in Appendix 2). **B)** Full SCICHEM chemistry scheme as included in the multi-component input file "fullchem_ae5_SW". **C)** Adapted EMEP chemistry scheme (Figure 43 in Appendix 2).*

3.2.2 Effect of Different Background Conditions

Figure 9 shows the NO_2 fields corresponding to five different ambient levels. The ambient levels as used by Charlton-Perez et al. (2009) (Table 1), the default ambient levels from the multi-component input file "fullchem_ae5_SW" without the "SW.amb" file, the Florida ambient levels ("FL.amb"), the Washington state ambient levels ("WA.amb") and the NILU-provided ambient levels (Table 16 in Appendix 3) were applied respectively in Figure 9A, B,

C, D and E. The Florida ambient levels were applied since, the subtropical climate conditions in Florida resemble the conditions of the location used by Charlton-Perez et al. (2009). Washington State was chosen because it has a climate resembling Norway. In all cases, it can be observed that formation of NO_2 takes place near the source location, followed by a decrease back to ambient VMRs. In all cases, except in the cases where Charlton-Perez et al. (2009) and NILU-provided background levels were applied (Figure 9A and Figure 9E, respectively), the NO_2 field is relatively short, spanning approximately 5 km. In Figure 9E, the field spans approximately 7.5 km. However, in Figure 9A, ambient levels are not restored within the 30 km distance considered. Under relatively low NO_2 ambient levels (Figure 9A and E), the increase of NO_2 as a result of oxidation of the emitted NO is enough to cause a visible increase further downwind. Under the relatively high NO_2 ambient levels (Figure 9B-D), the additional NO_2 formed as a result of NO oxidation is not enough to lead to a visible increase starting at 5 km downwind from the source, due to the color scale used. Figure 10A to E show the corresponding NO fields, all with the highest VMR of $1.68 \cdot 10^8$ ppt near the source location, followed by a rapid decline back to ambient concentrations. Both the maximum VMR near the source and the rapid decline back to ambient concentrations were expected, since NO is emitted by the source and is rapidly oxidized to NO_2 when it reaches the atmosphere (United States Environmental Protection Agency, 1999). Contrary to the other NO fields, the NO field under NILU-provided ambient levels (Figure 10E) is more elongated, spanning at least 30 km. Figure 11A to E show the corresponding O_3 fields, which all have a depletion area near the source location, albeit short. Due to the color scale used, Figure 11B shows a particularly small area of O_3 depletion, which is the result of the high ambient O_3 level compared to the other backgrounds used (Figure 11A,C-E). As a result, only a relatively large depletion is visible in the O_3 field. For example, a 3.1 ppb depletion relative to the ambient level in Figure 11A shifts the resulting VMR to the next color level. In Figure 11B, a 35.4 ppb depletion would be required to shift the VMR to the next color level. The depletion is expected and corresponds to what is shown in Figure 9A to E and Figure 10A to E: close to the source there is a high level of NO which reacts with O_3 forming NO_2 (R8), and this results in a depletion of O_3 and formation of NO_2. Figure 12A to E show the corresponding OH fields. Figure 12A and Figure 12E show an OH depletion near the source, which is expected based on the depletion shown in the O_3 fields (Figure 11A and Figure 11E). O_3 is a precursor for OH. So when O_3 is depleted, the reactions forming OH are reduced (R5 and R7). Figure 12B to D show, however, an unexpected OH formation near the source. The reaction between HO_2 and NO forming OH and NO_2 (R12) was found to be responsible

for this. Involved in this reaction are both the ambient HO_2 and the HO_2 that is formed out of ambient $CH_3C(O)O_2$ (R10 and R11). Figure 12E also shows an OH formation starting 6 km downwind from the source. This area of formation was also found to be the result of the reaction between HO_2 and NO forming OH (R12).

It can be noticed that the background conditions set by Charlton-Perez et al. (2009) force OH depletion close to the source. They emit a large amount of NO in a relatively clean atmosphere, as can be seen in Table 1. Species such as peroxy radicals (e.g. HO_2 and $CH_3C(O)O_2$) are not included in the background close to the source. Therefore, the clean conditions as set by Charlton-Perez et al. (2009) result in ozone titration close to the source, and eventually in OH depletion (Charlton-Perez et al., 2009). Using a more polluted background with peroxy radicals (e.g. the default ambient levels, Florida ambient levels or Washington state ambient levels) leads to OH formation near the source. However, under the NILU-provided background conditions, where the peroxy radicals are also included, no OH formation occurs close to the source. This could be explained by the $CH_3C(O)O_2$ ambient VMR being almost an order of magnitude lower under NILU-provided ambient levels than under the default, Florida and Washington State ambient levels, whereas the HO_2 ambient VMR is only a factor of 1.5 higher under NILU-provided ambient levels (Table 2). As a result, the reaction between HO_2 and NO forming OH and NO_2 (R12) is more limited under NILU-provided ambient levels than under default, Florida and Washington State ambient levels. It is, however, important to note that in reality the background conditions are not stable. For example, OH concentrations vary significantly in the course of a day (Davis, 1977). Therefore, accurate modeling of concentration fields requires the use of accurate ambient concentrations for the location and period of interest.

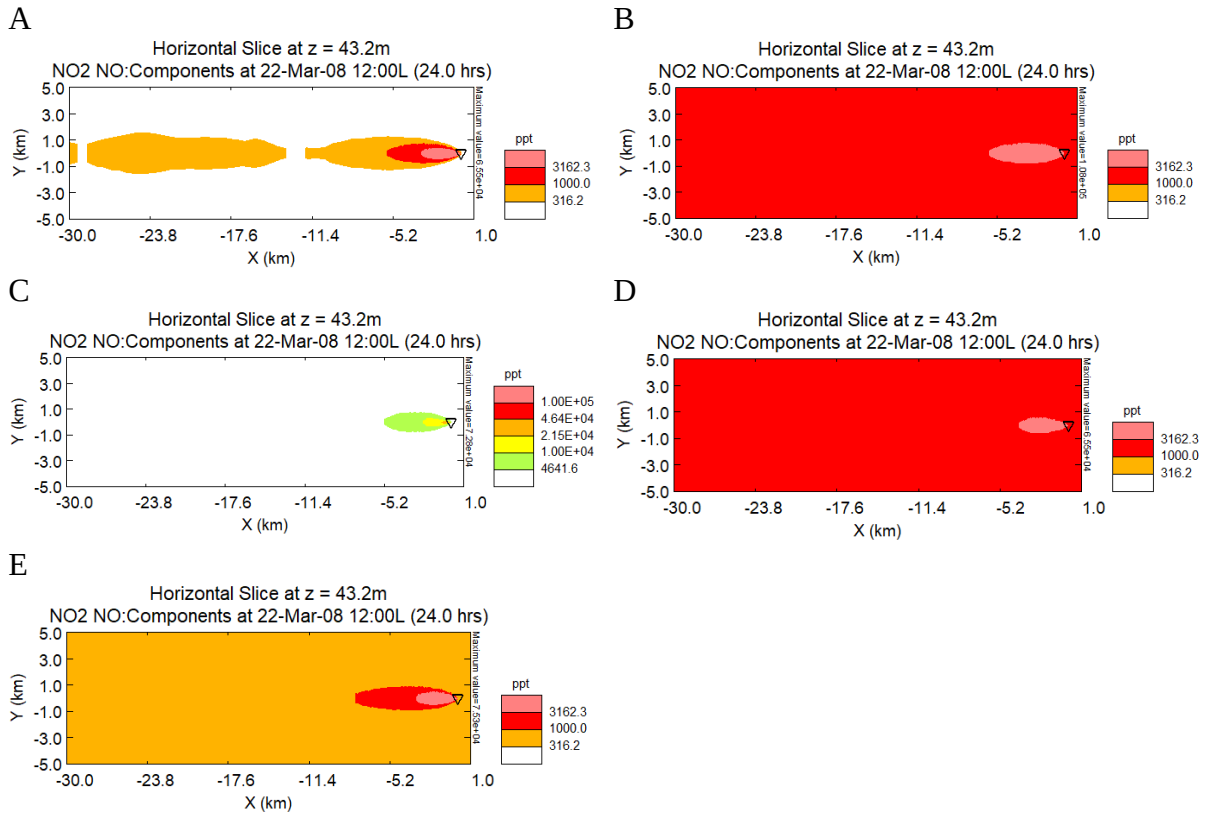

*Figure 9: NO_2 fields modelled with SCICHEM and plotted with the SCICHEM GUI after emission of 33 g/s NO from a stack with a height of 43.2 m. The source location is indicated by the symbol ∇. Different background volume mixing ratios were applied in the multi-component file "fullchem_ae5_SW". **A)** Charlton-Perez et al. (2009) ambient volume mixing ratios (Table 1). **B)** Default values from the multi-component input file. **C)** Florida ambient volume mixing ratios ("FL.amb"). Note the different color scale compared to the fields shown in A, B, D and E. **D)** Washington State volume mixing ratios ("WA.amb"). **E)** NILU-provided ambient volume mixing ratios (Table 16 in Appendix 3).*

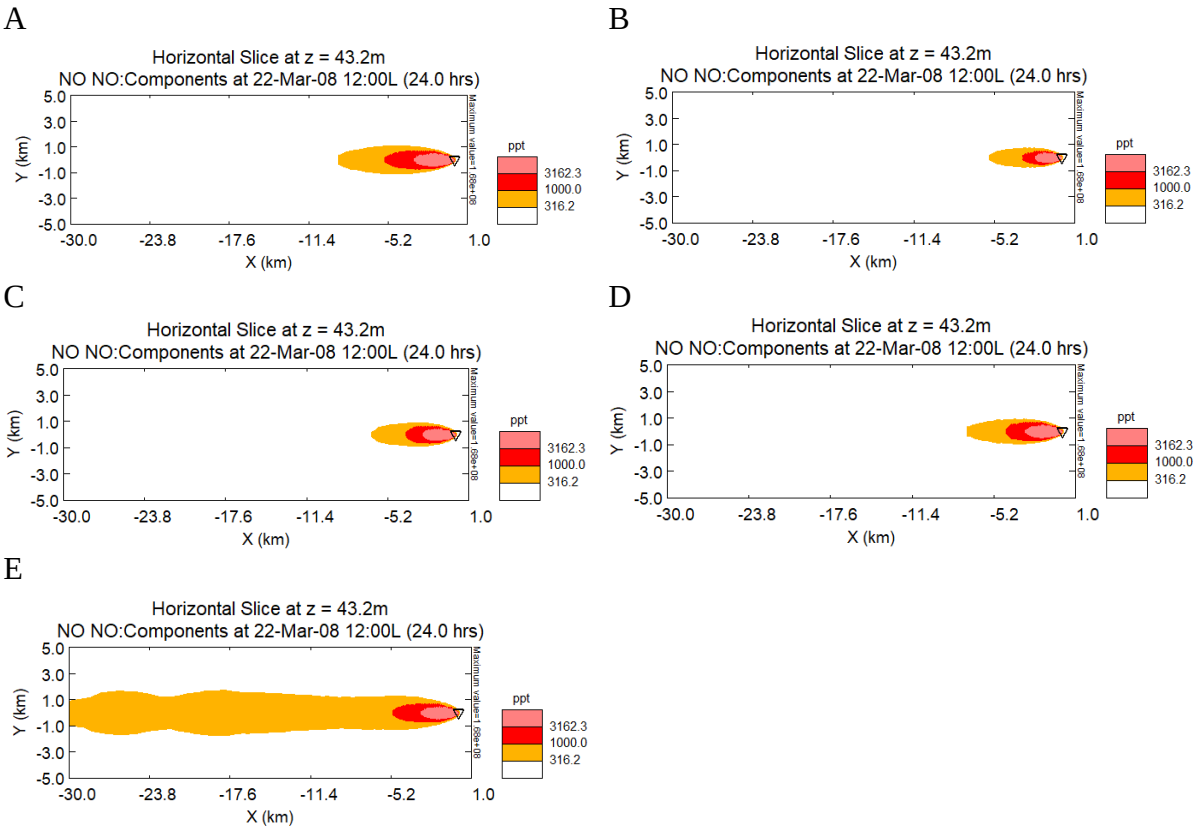

*Figure 10: NO fields modelled with SCICHEM and plotted with the SCICHEM GUI after emission of 33 g/s NO from a stack with a height of 43.2 m. The source location is indicated by the symbol ∇. Different background volume mixing ratios were applied in the multi-component file "fullchem_ae5_SW". **A)** Charlton-Perez et al. (2009) ambient volume mixing ratios (Table 1). **B)**: Default values from the multi-component input file. **C)** Florida ambient volume mixing ratios ("FL.amb"). **D)** Washington State volume mixing ratios ("WA.amb"). **E)** NILU-provided ambient volume mixing ratios (Table 16 in Appendix 3).*

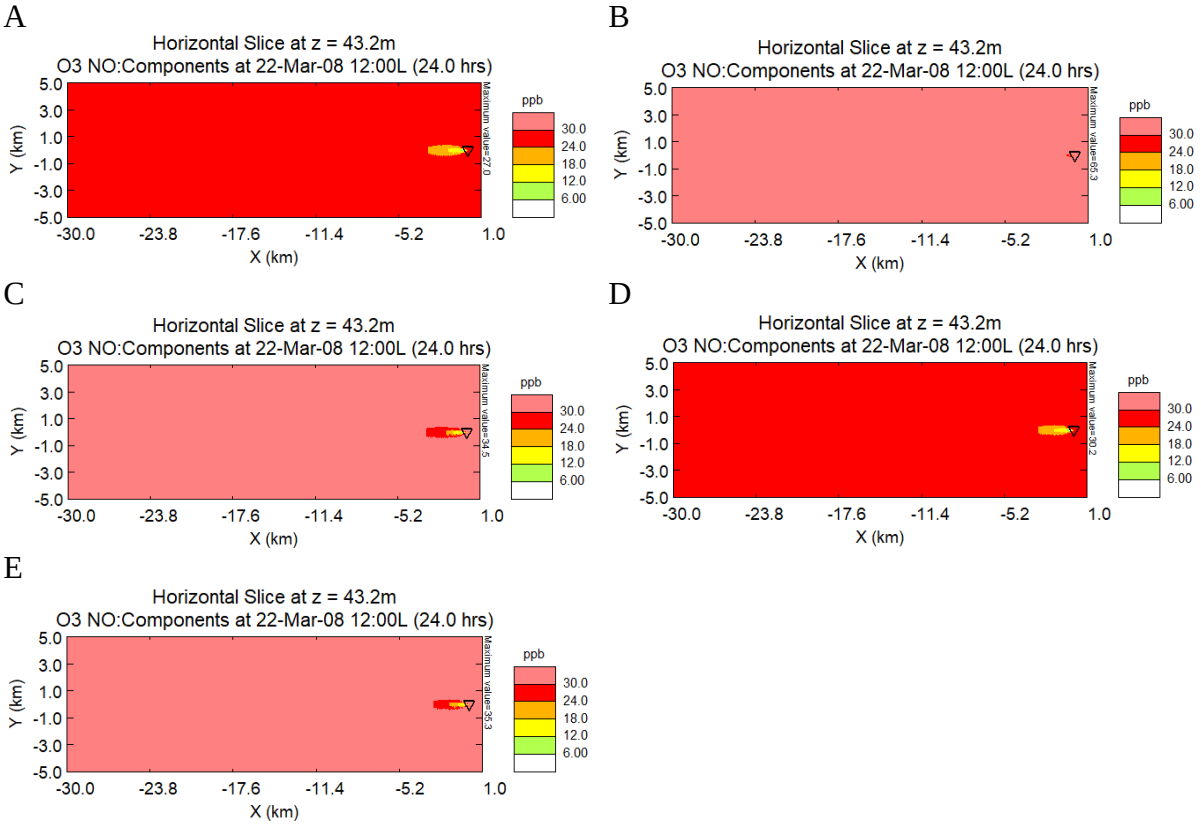

*Figure 11: O_3 fields modelled with SCICHEM and plotted with the SCICHEM GUI after emission of 33 g/s NO from a stack with a height of 43.2 m. The source location is indicated by the symbol ∇. Different background volume mixing ratios were applied in the multi-component file "fullchem_ae5_SW". **A)** Charlton-Perez et al. (2009) ambient volume mixing ratios (Table 1). **B)** Default values from the multi-component input file. **C)** Florida ambient volume mixing ratios ("FL.amb"). **D)** Washington State volume mixing ratios ("WA.amb"). **E)** NILU-provided ambient volume mixing ratios (Table 16 in Appendix 3).*

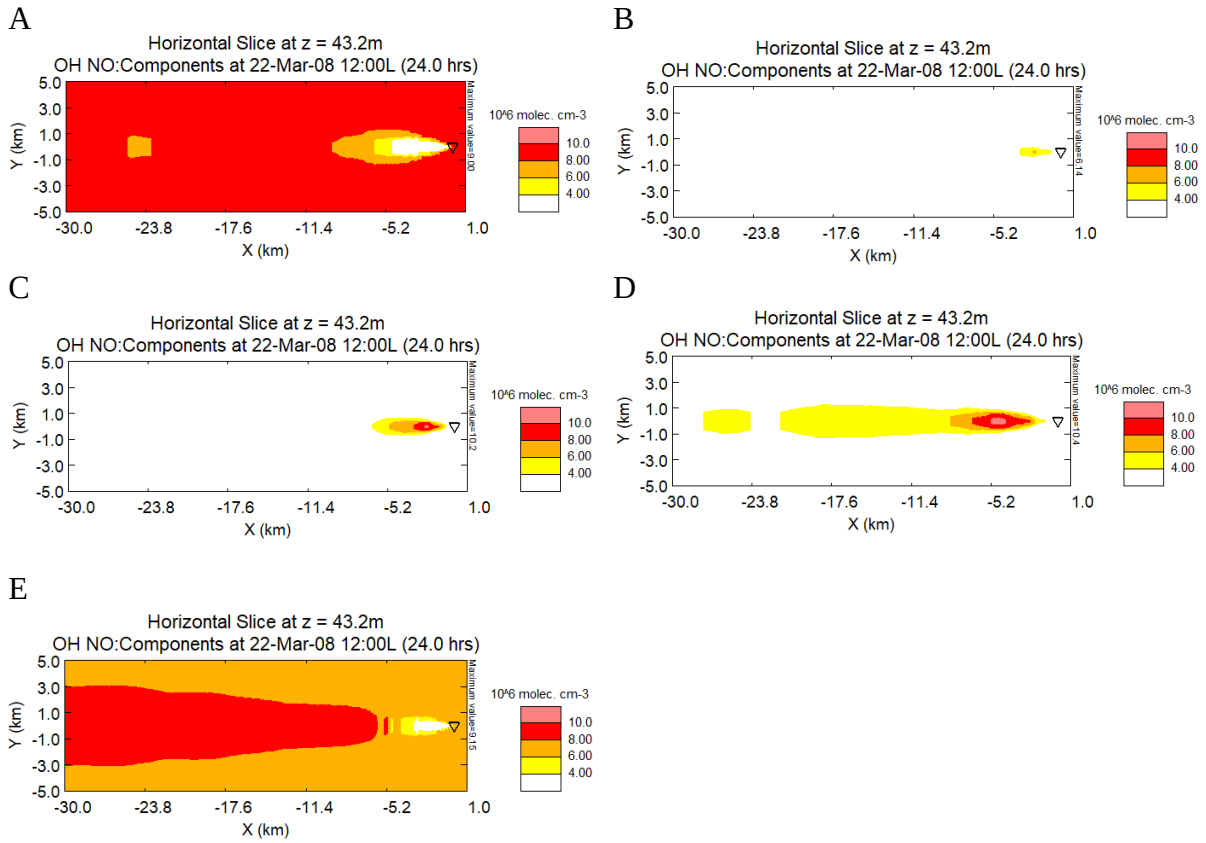

*Figure 12: OH fields modelled with SCICHEM and plotted with the SCICHEM GUI after emission of 33 g/s NO from a stack with a height of 43.2 m. The source location is indicated by the symbol ∇. Different background volume mixing ratios were applied in the multi-component file "fullchem_ae5_SW". **A)** Charlton-Perez et al. (2009) ambient volume mixing ratios (Table 1). **B)** Default values from the multi-component input file. **C)** Florida ambient volume mixing ratios ("FL.amb"). **D)** Washington State volume mixing ratios ("WA.amb"). **E)** NILU-provided ambient volume mixing ratios (Table 16 in Appendix 3).*

3.2.3 Effect of Reduced NO Emission on the OH Field

Figure 13A and B show the OH fields formed after emission of 33 and 3.3 g/s NO respectively. These fields were formed using the chemistry scheme and atmospheric background as described by Charlton-Perez et al. (2009) (Figure 42 in Appendix 2). It is shown that a reduction of the NO emission by a factor of 10 still results in OH depletion close to the source. However, the field length is a factor of 6.5 shorter. This can be explained by less NO being present near the source to deplete the O_3. Consequently, ambient O_3 concentrations are restored closer to the source. This enables OH formation closer to the source and a faster increase back to the ambient OH VMR as well (R5 and R7). Moreover, there is no area of total OH depletion when the NO emission has been reduced (Figure 13B), as was the case within the first 3 km downwind under higher NO emission (Figure 13A). This can be explained by the emitted NO not being enough to fully deplete the present O_3 (R5). As a result, OH formation will not be stopped completely close to the source (R7). Similar results, where the OH depletion area is smaller because of

reduced NO emission, are shown in Figure 14A and B (full SCICHEM chemistry scheme) as well as in Figure 15A and B (adapted EMEP chemistry scheme). As can be seen in Figure 14B, the OH depletion further downwind, which is a result of HNO_3 formation (R13), has been reduced as well. This can be explained by the fact that HNO_3 formation depends on the NO_2 concentration. NO is oxidized to NO_2 in the atmosphere (R8). If less NO is emitted, less NO_2 will be present in the field to react with OH and form HNO_3 (R13). Figure 15B shows, however, some areas of depletion further downwind which were not present when more NO was emitted (Figure 15A). These are depletions of maximum $0.1 \cdot 10^6$ molecules cm^{-3} (1%) in a background of $9 \cdot 10^6$ molecules cm^{-3}, and are therefore negligible.

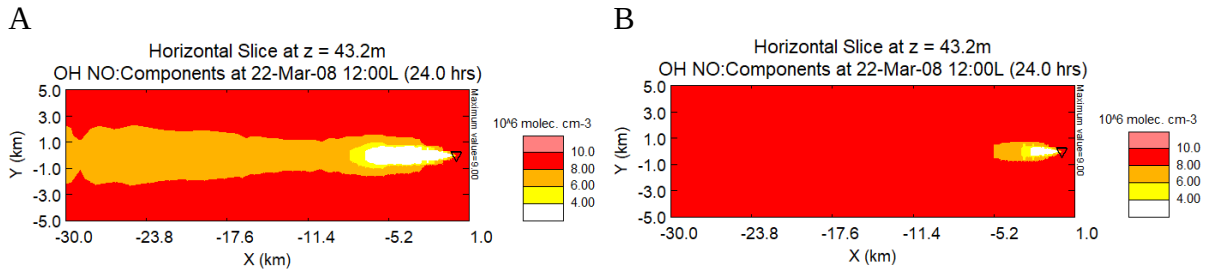

*Figure 13: OH fields modelled with SCICHEM and plotted with the SCICHEM GUI after emission of 33 g/s (**A**) and 3.3 g/s (**B**) NO from a stack with a height of 43.2 m. The source location is indicated by the symbol ∇. The multi-component input file as shown in Figure 42 in Appendix 2, i.e. the chemistry file and ambient concentrations as described by Charlton-Perez et al. (2009), was used..*

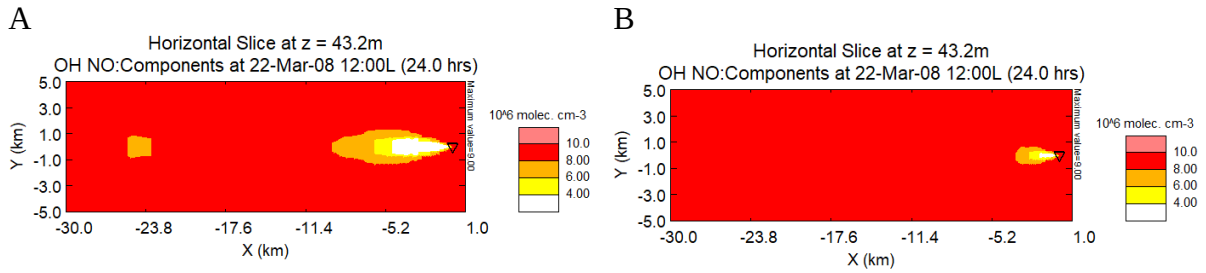

*Figure 14: OH fields modelled with SCICHEM and plotted with the SCICHEM GUI after emission of 33 g/s (**A**) and 3.3 g/s (**B**) NO from a stack with a height of 43.2 m. The source location is indicated by the symbol ∇. The full SCICHEM multi-component input file "fullchem_ae5_SW" was used with ambient concentrations by Charlton-Perez et al. (2009) as described in Table 1.*

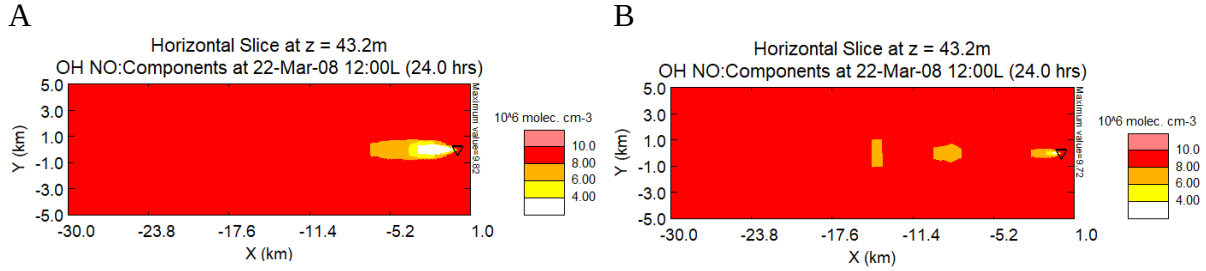

*Figure 15: OH fields modelled with SCICHEM and plotted with the SCICHEM GUI after emission of 33 g/s (**A**) and 3.3 g/s (**B**) NO from a stack with a height of 43.2 m height. The source location is indicated by the symbol ∇. The multi-component input file with the adapted EMEP chemistry scheme (Figure 43 in Appendix 2) with ambient concentrations by Charlton-Perez et al. (2009), as described in Table 1, was used.*

3.2.4 Summary Case Study 2

Case study 2 was used as a learning case to understand the influence of the atmospheric chemical background, the applied atmospheric chemistry scheme and NO emission strength on the chemical evolution of an isolated ship plume. Table 4 shows an overview of the results obtained for the NO, NO_2, O_3 and OH fields when using different chemistry schemes (i.e. the Charlton-Perez et al. (2009) chemistry scheme, the full SCICHEM chemistry scheme and the adapted EMEP chemistry scheme). Table 5 shows an overview of the results obtained by applying the full SCICHEM chemistry scheme ("fullchem_ae5_SW"), but with different background conditions (i.e. the Charlton-Perez et al. (2009) conditions as shown in Table 1, the default conditions in the full SCICHEM chemistry scheme, the Florida conditions, Washington State conditions and the NILU-provided conditions as shown in Table 16 in Appendix 3). High levels of background peroxy radicals (i.e. HO_2 and $CH_3C(O)O_2$) were found to lead to OH formation close to the source. Lower levels of peroxy radicals resulted in OH depletion close to the source.

Finally, regardless of the chemistry scheme applied, a reduced NO emission was found to cause shorter OH fields with less depletion as well.

Table 4: Overview of the results obtained after performing the simulation as described by Charlton-Perez et al. (2009) with ambient conditions as described in Table 1 but with different chemistry schemes applied: i.e. the chemistry scheme by Charlton-Perez (Figure 43 in Appendix 2), the full SCICHEM chemistry scheme ("fullchem_ae5_SW") and the adapted EMEP chemistry scheme (Figure 44 Appendix 2).

Chemistry scheme	**NO field**	**NO_2 field**	**O_3 field**	**OH field**
Charlton-Perez et al. (2009)	- Highest VMR close to the source.	- Highest VMR close to the source.	- Short field spanning a couple of km. - Depletion area close to the source.	- Long field spanning at least 30 km. - Depletion area close to the source.
Full SCICHEM	- Highest VMR close to the source.	- Highest VMR close to the source.	- Short field spanning a couple of km. - Depletion close to the source.	- Short field spanning approximately 10 km with an area of depletion close to the source. - Depletion area at 24 km downwind from the source.
Adapted EMEP	- Highest VMR close to the source. - Longer field compared to the other NO fields.	- Highest VMR close to the source. - Shorter field compared to the other NO_2 fields.	- Short field spanning a couple of km. - Depletion area close to the source.	- Short field spanning approximately 7 km. - Depletion area close to the source.

Table 5: Overview of the results obtained from the simulation as described by Charlton-Perez et al. (2009) but with the full SCICHEM chemistry scheme ("fullchem_ae5_SW") and different ambient conditions: Charlton-Perez et al. (2009) ambient conditions (Table 1), default ambient conditions from the full SCICHEM chemistry file, ambient conditions for Florida ("FL.amb") and Washington State ("WA.amb"), and NILU-provided ambient conditions (Charlton-Perez et al., 2009).

Background conditions	**NO field**	**NO_2 field**	**O_3 field**	**OH field**
Charlton-Perez et al. (2009)	- Short field with highest VMR close to the source.	- Lowest NO_2 ambient level. Resulting in a long NO_2 plume with highest VMR close to the source.	- Short field, with depletion area close to the source.	- Field spanning around 10 km. With OH depletion close to the source. - Another OH depletion at 24 km downwind.
Default	- Short field with highest VMR close to the source.	- High NO_2 ambient level leading to a short field with highest VMR close to the source.	- Very short O_3 field, with depletion area close to the source.	- Short field, spanning around 4 km with OH formation close to the source.
FL.amb	- Short field with highest VMR close to the source.	- High NO_2 ambient level leading to a short field with highest VMR close to the source.	- Short field, with depletion area close to the source.	- Field spanning approximately 6 km, with OH formation close to the source.

Background conditions	NO field	NO_2 field	O_3 field	OH field
WA.amb	- Short field with highest VMR close to the source.	- High NO_2 ambient level leading to a short field with highest VMR close to the source.	- Short field, with depletion area close to the source.	- Field spanning around 20 km with OH formation close to the source and another area of OH formation at 24 km downwind.
NILU	- Long field (spanning at least 30 km) with highest VMR close to the source.	- Higher NO_2 background level compared to Charlton-Perez conditions, but lower than the others. Results in a NO_2 field spanning approximately 7.5 km, with highest VMR close to the source.	- Short field, with depletion area close to the source.	- Field with OH depletion spanning a distance of approximately 5 km downwind from the source. - OH formation starting at 6 km downwind.

3.3 Case Study 3a: Waste-to-Energy Plant Plume Chemistry Simulations (without Amines)

Figure 16A and B show the NO_2 fields of the combustion plume at surface level and at 80.5 m above the surface, respectively. The NO_2 fields were formed at 14:00h local time after emission of 3.02 g/s NO at the WtE plant. Surface level was chosen because that is where human

exposure occurs. 80.5 m above the surface was determined to be the level at which the highest VMR of NO_x could be found. As a result, the reactions in which NO_x are involved are expected to lead to different results at surface level and at 80.5 m height. Both Figure 16A and B show the largest VMR, i.e. 3.02 ppb and 39.5 ppb, near the source, as a result of the reaction between O_3 and NO which forms NO_2 (R8). The largest VMR at surface level can be found at 0.8 km downwind and at 80.5 m height at 0.4 km downwind. It can also be seen that in the first couple of kilometers downwind from the source, the NO_2 field at 80.5 m height dilutes more rapidly than the NO_2 field at surface level. This is because the plume is already diluted when it reaches surface level after emission at stack height. Moreover, the surface acts as a barrier for the vertical dispersion. Therefore, the maximum mean concentration of a conserved scalar emitted by a moderately elevated source is found at surface level at a certain distance away from the source.

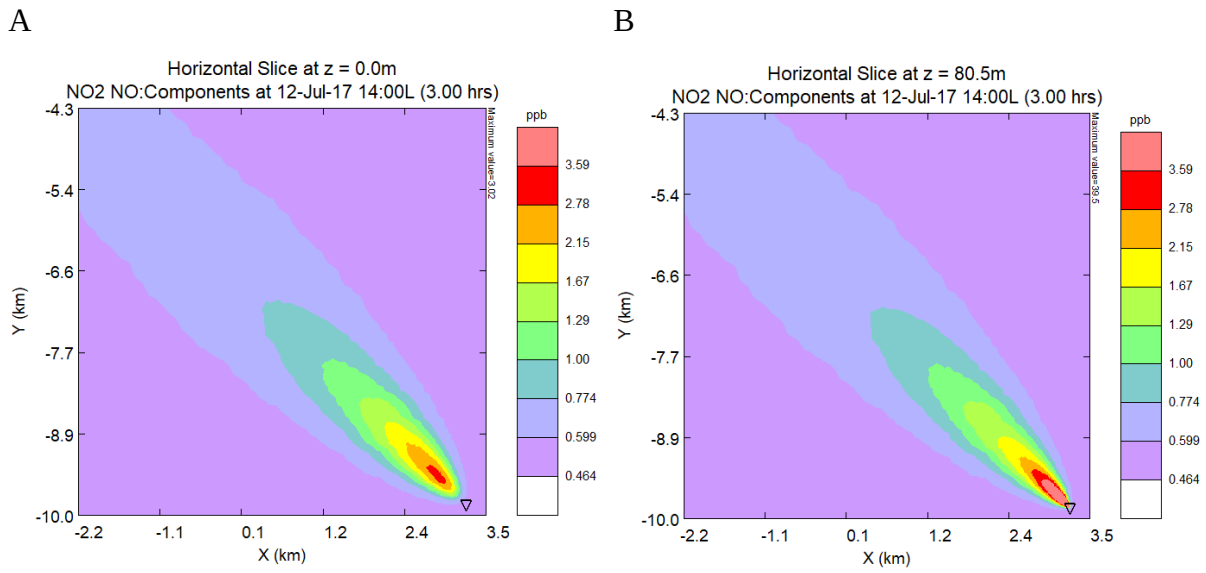

*Figure 16: NO_2 field modelled with SCICHEM and plotted with the SCICHEM GUI at surface level (**A**) and at a height of 80.5 m (**B**) at the WtE plant. The emission source, emitting 3.02 g/s NO at a stack height of 80 m, is indicated by the symbol ∇.The full SCICHEM chemistry file ("fullchem_ae5_SW") was used, with the atmospheric chemical background as described in Table 16 in Appendix 3.*

Figure 17A and B show the NO fields of the plume at surface level and at 80.5 m height, respectively. The largest VMR can be found near the source, i.e. 3.87 ppb (Figure 17A) and $3.21 \cdot 10^4$ ppb (Figure 17B). This can be explained by the fact that NO was emitted by the source and has not yet mixed well with the ambient air. The NO is mixed vertically, resulting in a VMR reduction by a factor of $8 \cdot 10^3$ near the source at surface level compared to 80.5 m height. The difference between the location of the largest VMR at surface level, i.e. at 0.6 km downwind, and at a height of 80.5 m, i.e. at 0.4 km downwind, can be explained by the emission

plume simultaneously spreading downwind and in vertical direction. As a result, the maximum NO VMR is found closer to the source near stack height (i.e. 80.5 m) than at surface level. Both the field on surface level (Figure 17A) as well as the field at 80.5 m height (Figure 17B) gradually decrease back to an ambient VMR of 0.167 ppb at 6 km downwind from the source. This indicates that, similarly to the NO_2 fields (Figure 16A-B), the NO field dilutes much more rapidly at 80.5 m height than at surface level. Comparing the NO field at surface level (Figure 17A) to the NO_2 field at surface level (Figure 16A), indicates that there is no strong NO field at surface level after 3.02 g/s NO emission. The maximum VMRs of NO and NO_2 are very similar (i.e. 3.87 and 3.02 ppb respectively). The difference is larger when looking at an 80.5 m height (Figure 16B and Figure 17B). The decreasing difference between the VMRs of NO and NO_2 with decreasing altitude can be explained by the time it takes to oxidize NO to NO_2. This oxidation is also limited by other reactants in the atmosphere. So, when NO is emitted from a stack and the plume spreads downwards, NO_2 is produced and NO is diluted.

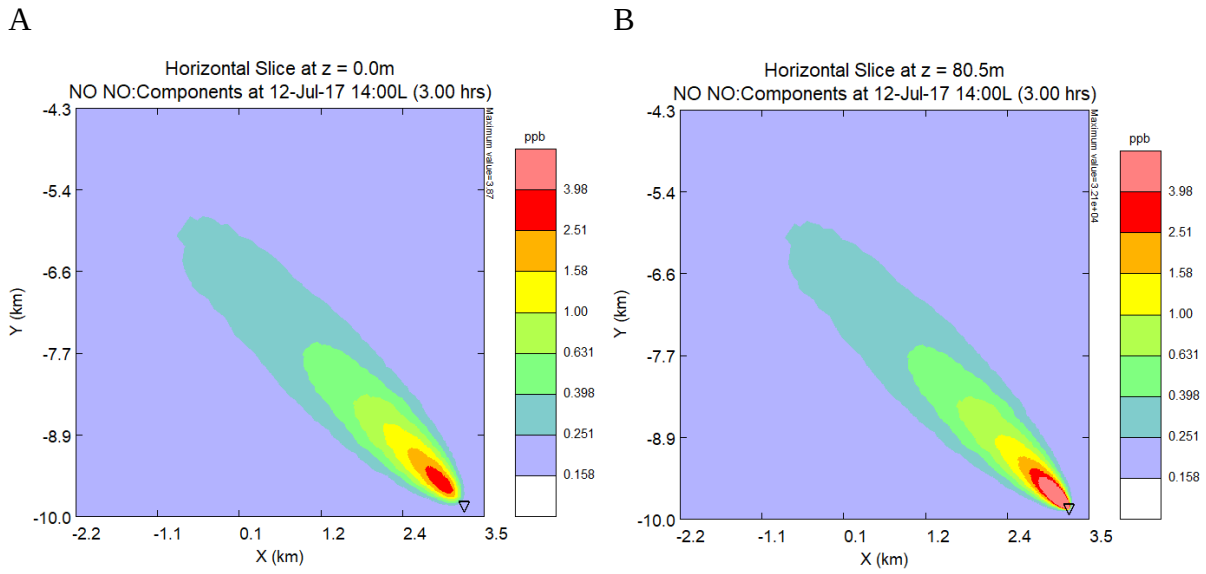

*Figure 17: NO field modelled with SCICHEM and plotted with the SCICHEM GUI at surface level (**A**) and at a height of 80.5 m (**B**) at the WtE plant. The emission source, emitting 3.02 g/s NO at a stack height of 80 m, is indicated by the symbol ∇.The full SCICHEM chemistry file ("fullchem_ae5_SW") was used, with the atmospheric chemical background as described in Table 16 in Appendix 3.*

Figure 18A and B show the O_3 fields within the plume at surface level and at 80.5 m height, respectively, formed at 14:00h local time after emission of 3.02 g/s NO at the WtE plant. Both Figure 18A and B show a short field, spanning approximately 3 kilometers in distance. It can be observed in both cases, that there is a depletion of O_3 near the source, before it gradually increases back to the ambient VMR. This depletion is expected, since O_3 present in the atmosphere near the source reacts with the emitted NO (R8). However, at surface level (Figure

18A) this is a small depletion, i.e. a maximum depletion of approximately 3.1 ppb (9.0%), compared to the ambient VMR of 34.4 ppb at 0.7 km downwind from the source. At an 80.5 m height (Figure 18B), there is a complete depletion (100%) of O_3 immediately at the source. This corresponds to the large difference between NO present at the source at surface level and at 80.5 m height (Figure 17A-B). At surface level, this amount of NO is not sufficient to fully deplete O_3 (R8), whereas it is sufficient at 80.5 m height. Moreover, it can be seen that the depletion area at surface level (Figure 18A) starts approximately 0.2 km further downwind than at a height of 80.5 m (Figure 18B), because NO is emitted at a stack height of 80 m and reaches the surface level further downwind from the source.

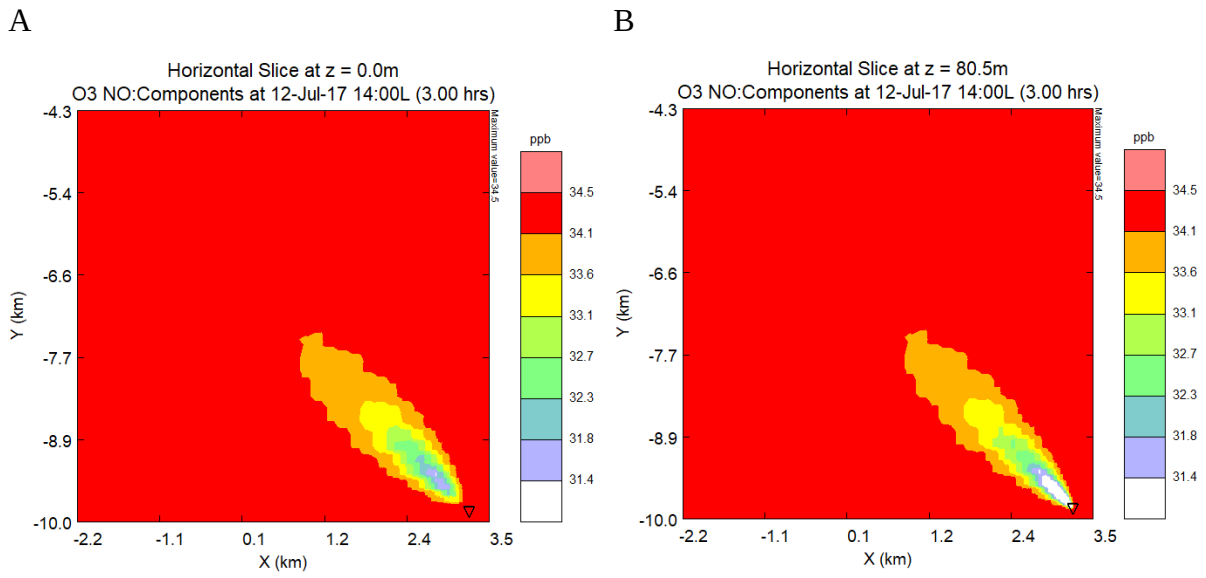

*Figure 18: O_3 field modelled with SCICHEM and plotted with the SCICHEM GUI at surface level (**A**) and at a height of 80.5 m (**B**) at the WtE plant. The emission source, emitting 3.02 g/s NO at a stack height of 80 m, is indicated by the symbol ∇.The full SCICHEM chemistry file ("fullchem_ae5_SW") was used, with the atmospheric chemical background as described in Table 16 in Appendix 3.*

Figure 19A and B show the plume's OH fields at surface level and at a height of 80.5 m, respectively. Figure 19A shows an OH depletion within the first 1.5 km, with maximum depletion occurring at 0.8 km downwind from the source. This is not a total depletion, but a depletion of maximum $1.39 \cdot 10^{-4}$ ppb (46%) compared to the ambient VMR of OH of $3.04 \cdot 10^{-4}$ ppb. However, contrary to what was expected based on the reactions included in the model (R5, R7 and R8), the highest OH VMR ($4.06 \cdot 10^{-4}$ ppb) can be found approximately 2.2 km downwind from the source. This formation relative to the ambient OH level results in an increase of $1.02 \cdot 10^{-4}$ ppb (34%) compared to the ambient OH VMR. Such an increase was unexpected, since ozone titration (R8) still occurs at this position downwind from the source (see Figure 18A). Based on reactions R5 and R7, an OH depletion was expected close to the

source. Figure 19B shows a similar field to Figure 19A, but with a total depletion within the first 1.5 km. The highest OH VMR, i.e. $3.97 \cdot 10^{-4}$ ppb, can be seen at 2.2 km downwind from the source. This is an increase of 31% compared to the ambient OH VMR. Comparison of the OH fields (Figure 19A-B) to the O_3 fields (Figure 18A-B), shows that in case of total O_3 depletion (Figure 18B), a total depletion of OH can be observed as well (Figure 19B). If there is not a total O_3 depletion, as at surface level (Figure 18A), there is not a total OH depletion either (Figure 19A). However, this shows that the conceptual picture (i.e. NO emission from a stack leads to ozone titration which results in total OH depletion close to the source, thereby stopping OH chemistry) is not entirely true under the conditions used in these simulations. Within 1.5 km downwind from the source, OH is depleted but it is not a total depletion throughout. Moreover, OH formation is observed around 2 km downwind from the source. The following sections focus on trying to understand this unexpected OH pattern.

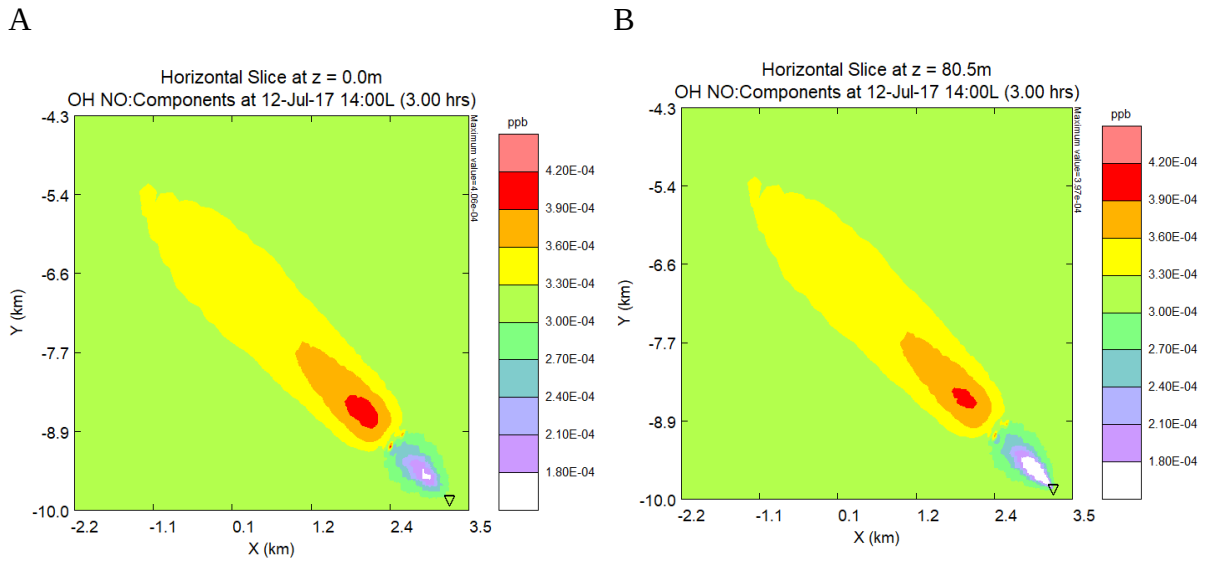

*Figure 19: OH field modelled with SCICHEM and plotted with the SCICHEM GUI at surface level (**A**) and at a height of 80.5 m (**B**) at the WtE plant. The emission source, emitting 3.02 g/s NO at a stack height of 80 m, is indicated by the symbol ∇.The full SCICHEM chemistry file ("fullchem_ae5_SW") was used, with the atmospheric chemical background as described in Table 16 in Appendix 3.*

3.3.1 Effect of Chemistry on the OH Field

The reaction between HO_2 and NO which forms OH and NO_2 (R12) was found to be responsible for the OH formation observed in Figure 19. Removing this reaction from the chemistry scheme used in the model results in an OH field where the OH is depleted compared to the background VMR. Ambient HO_2 was found to be the main source of HO_2 in R12. Reactions between HO_2 and O (R14) or O_3 (R15) were also found to play a role in the OH formation close to the source,

albeit to a much lesser extent than R12. The observed OH formation was found to be limited as a result of HNO_3 formation, where OH reacts with NO_2 forming HNO_3 (R13), and ozone titration, where O_3 reacts with NO forming NO_2 (R8). Both HNO_3 formation (R13) and ozone titration (R8) were also found to be responsible for most of the OH depletion observed. The formation of HONO (R16), where OH reacts with NO, was found to be responsible for the remaining OH depletion. An overview of the reactions that were determined to be important for the observed OH field (Figure 19) are shown in Figure 2 in section 1.2. It shows the main species causing OH formation and the main sinks of OH in the atmosphere. These reactions are extensively researched. Therefore, there are not many assumptions within these reactions or their reaction rates. If the model characterizes these chemical reactions properly, this will boost the confidence in the model results for near source OH. It is, however, important to note that these results are specific for the atmospheric chemical background used (Table 16 in Appendix 3). As was shown in section 3.2.2, different background conditions may result in different results. Moreover, the background conditions are not constant in reality, but were considered to be constant in these simulations.

3.3.2 Effect of Different Emissions on the OH Field

Figure 20 shows the OH fields at surface level (A) and at 80.5 m height (B) that are emitted at the WtE plant after increasing the NO emission from 3.02 g/s to 30.2 g/s. It can be seen that the area of depletion spans a longer distance downwind from the source compared to Figure 19A-B. Up to 2 km downwind from the source, there is a total depletion of OH, with OH VMRs of $1.0 \cdot 10^{-27}$ ppb. This total OH depletion did not occur at surface level when 3.02 g/s NO was emitted (Figure 19A) and the area of total OH depletion was smaller at surface level (Figure 20A) than at 80.5 m height (Figure 20B). The entire area of OH depletion shown in Figure 20A-B spans up to 5.2 km downwind from the source. OH formation does not take place before 6 km downwind. Comparison of the OH field after a 30.2 g/s NO emission (Figure 20A-B) to the OH field after 3.02 g/s NO was emitted (Figure 19A-B), leads to the observation that the area of formation has shifted downwind and spans a larger distance of at least 24 km. Similar to the 3.02 g/s NO emission case, the OH formation can be explained by the reaction between HO_2 and NO (R12). HNO_3 formation (R13), HONO formation (R16) and ozone titration (R8) were responsible for the observed OH depletion close to the source as well as for limiting the OH formation further downwind. This indicates that increasing the NO emission results in a larger

OH depletion close to the source. However, in reality more species are emitted than just NO. These species may influence the chemistry that takes place in the emission field as well.

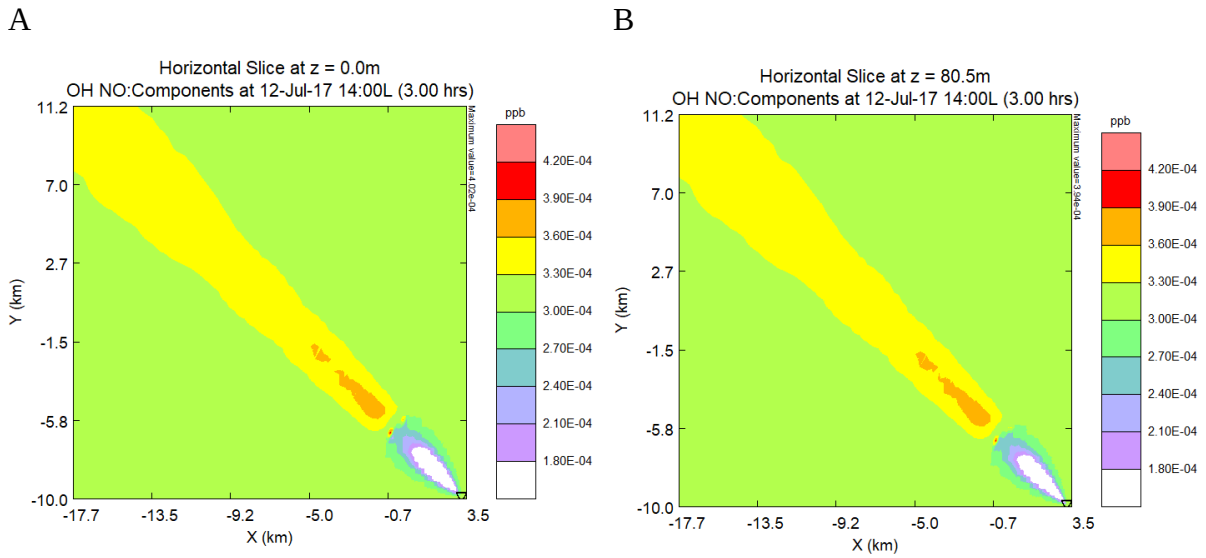

*Figure 20: OH field modelled with SCICHEM and plotted with the SCICHEM GUI at surface height (**A**) and at 80.5 m height (**B**) at the WtE plant. The emission source, emitting 30.2 g/s NO at a stack height of 80 m, is indicated by the symbol ∇. The full SCICHEM chemistry file ("fullchem_ae5_SW") was used, with the atmospheric chemical background described in Table 16 in Appendix 3.*

Emitting NO_2 (1% of total NO emission) reduced the OH formation further downwind, regardless of the amount of NO, i.e. 3.02 g/s (Figure 21A-B) or 30.2 g/s (Figure 22A-B), that was emitted. This was found to be the result of NO_2 reacting with OH and forming HNO_3 (R13), thereby acting as an OH sink. Moreover, emitting NO_2 resulted in less OH depletion close to the source. This was found to be the result of NO formation. Both the photolysis of NO_2 (R2) and the reaction between NO_2 and O (R1) were found to limit the OH depletion close to the source. The formed NO can react with the ambient HO_2, forming OH close to the source (R12). Moreover, the O formed in NO_2 photolysis (R2) can react forming O_3 (R3), which is an OH precursor (R5 and R7).

Emitting HONO (0.1% of total NO emission) in addition to NO (3.02 g/s) and NO_2 (1% of total NO emission), resulted in a restored OH formation further downwind (Figure 23A-B). This was found to be the result of the photolysis of HONO, during which OH and NO are formed (R17). This photolysis process only becomes important in the OH field when HONO is directly emitted from the stack. However, when the NO emission level is higher (i.e. 30.2 g/s), the OH that is formed as a result of HONO photolysis (R17), reacts immediately with the NO present, forming HONO again (R16, Figure 24A-B). Therefore, HONO emission would boost the OH concentration close to the source, provided that the NO emission level is low.

Another species that can be emitted is CH_3CHO. When emitting 0.016 g/s CH_3CHO in addition to 3.02 g/s NO (Figure 25A-B), it can be seen that the OH formation further downwind is reduced by approximately 8% compared to when only NO was emitted (Figure 19A-B), regardless of measuring height. This is the result of the CH_3CHO reacting with OH and acting as an additional OH sink (R9). Whereas previously ambient HO_2 was crucial in OH formation, the OH formation is now independent of the ambient HO_2. Instead, HO_2 formed from CH_3CHO now plays the key role. Since the OH precursor is emitted from the stack, it is pre-mixed in the plume. Consequently, the OH formation is independent of turbulent mixing with the background. When emitting 0.016 g/s CH_3CHO in addition to 30.2 g/s NO (Figure 26A-B), the OH formation further downwind decreases as well. However, the difference is smaller, i.e. a decrease of 0.2% at surface level and a decrease of 1.0% at 80.5 m height compared to the scenario when only NO was emitted (Figure 20A-B). This can be explained by OH still being depleted by NO further downwind, so there is less OH available to react with CH_3CHO, resulting in a smaller reduction in the OH formation. This indicates that it is not only important to use an accurate atmospheric background and chemistry scheme, but also to take into account all species that can be emitted from the stack.

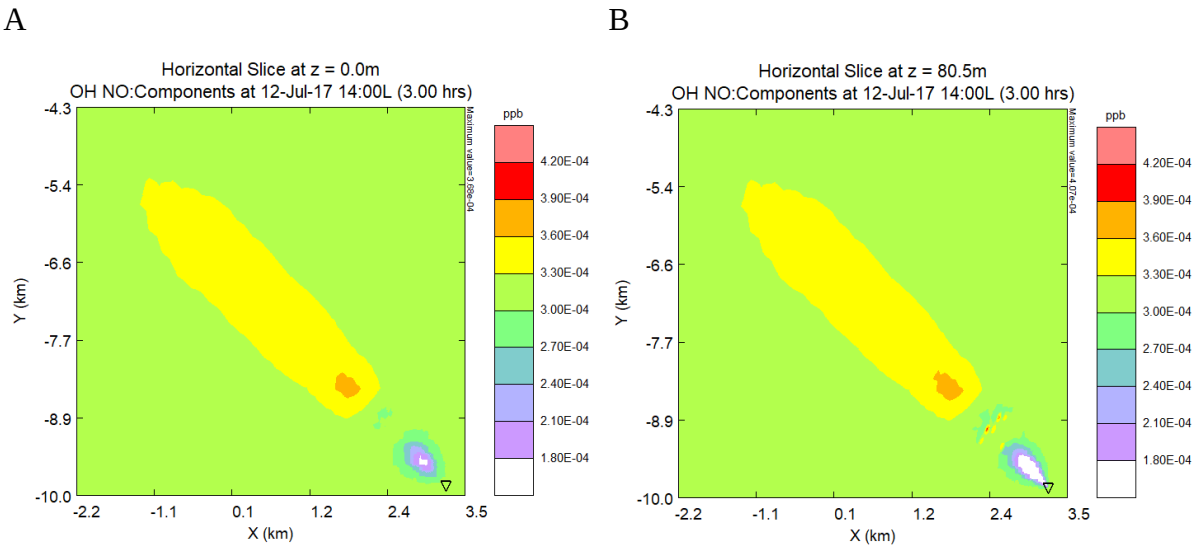

*Figure 21: OH field modelled with SCICHEM and plotted with the SCICHEM GUI at surface height (**A**) and at 80.5 m height (**B**) at the WtE plant. The emission source, emitting 3.02 g/s NO and $3.02 \cdot 10^{-2}$ g/s NO_2 at a stack height of 80 m, is indicated by the symbol ∇. The full SCICHEM chemistry file ("fullchem_ae5_SW") was used, with the atmospheric chemical background described in Table 16 in Appendix 3.*

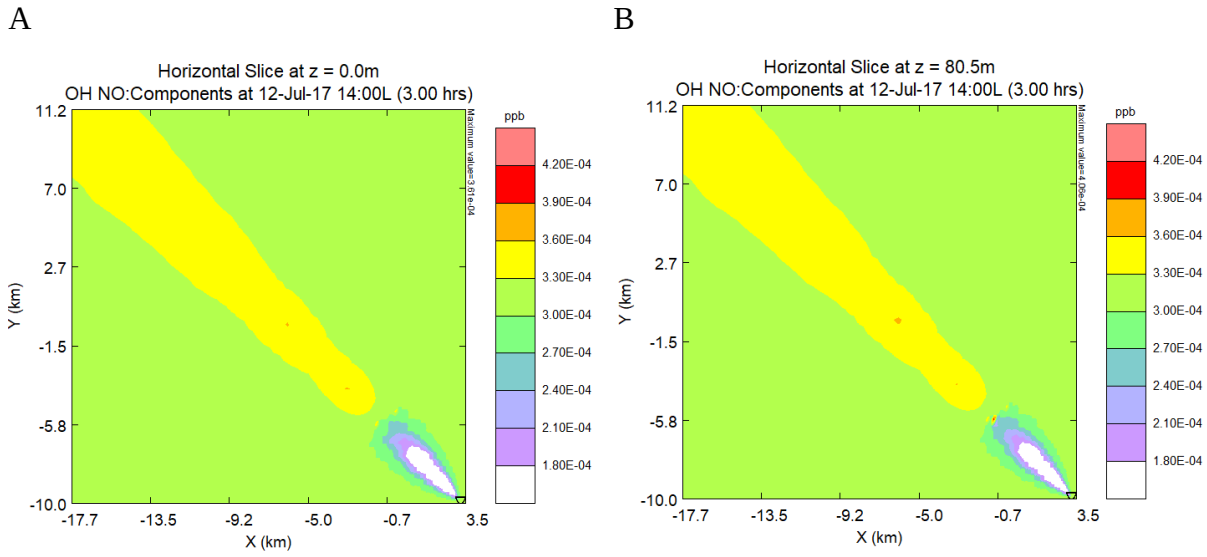

*Figure 22: OH field modelled with SCICHEM and plotted with the SCICHEM GUI at surface height (**A**) and at 80.5 m height (**B**) at the WtE plant. The emission source, emitting 30.2 g/s NO and $3.02 \cdot 10^{-1}$ g/s NO_2 at a stack height of 80 m, is indicated by the symbol ∇. The full SCICHEM chemistry file ("fullchem_ae5_SW") was used, with the atmospheric chemical background described in Table 16 in Appendix 3.*

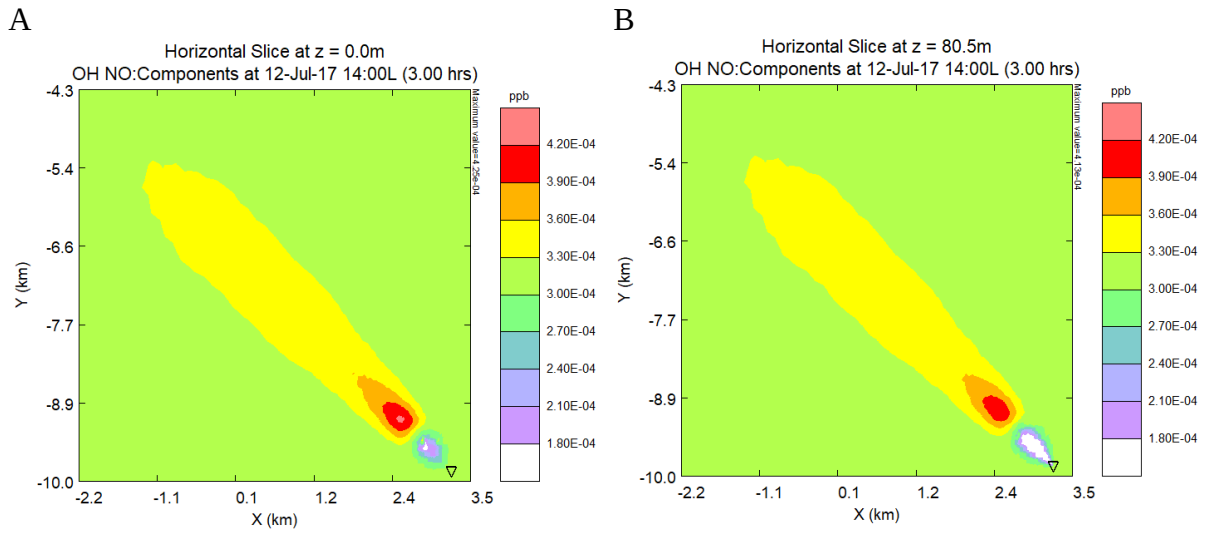

*Figure 23: OH field modelled with SCICHEM and plotted with the SCICHEM GUI at surface height (**A**) and at 80.5 m height (**B**) at the WtE plant. The emission source, emitting 3.02 g/s NO, $3.02 \cdot 10^{-2}$ g/s NO_2 and $3.02 \cdot 10^{-3}$ g/s HONO at a stack height of 80 m, is indicated by the symbol ∇. The full SCICHEM chemistry file ("fullchem_ae5_SW") was used, with the atmospheric chemical background described in Table 16 in Appendix 3.*

A

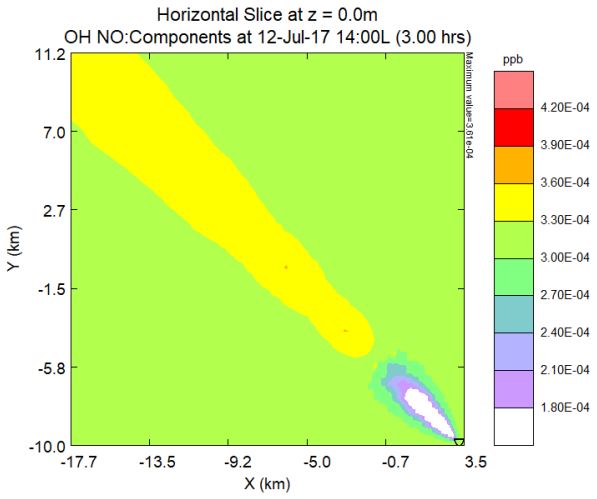

B

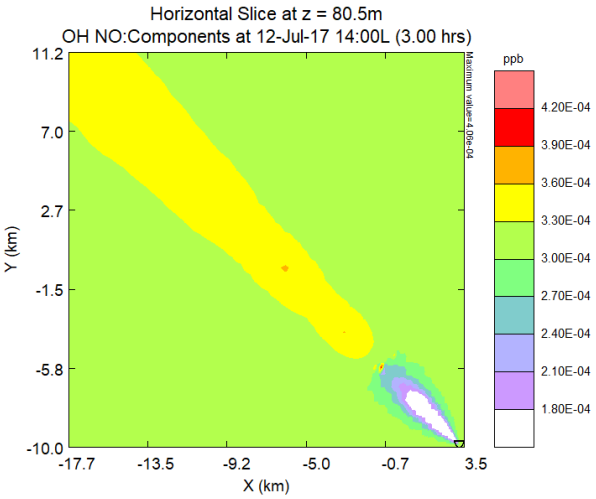

*Figure 24: OH field modelled with SCICHEM and plotted with the SCICHEM GUI at surface height (**A**) and at 80.5 m height (**B**) at the WtE plant. The emission source, emitting 30.2 g/s NO, $3.02 \cdot 10^{-1}$ g/s NO_2 and $3.02 \cdot 10^{-2}$ g/s HONO at a stack height of 80 m, is indicated by the symbol ∇. The full SCICHEM chemistry file ("fullchem_ae5_SW") was used, with the atmospheric chemical background described in Table 16 in Appendix 3.*

A

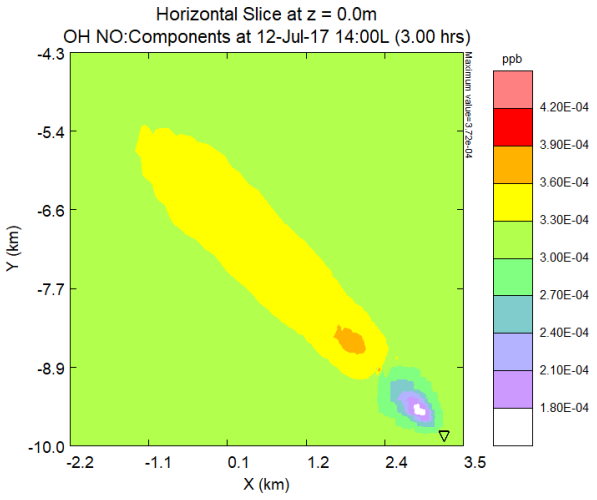

B

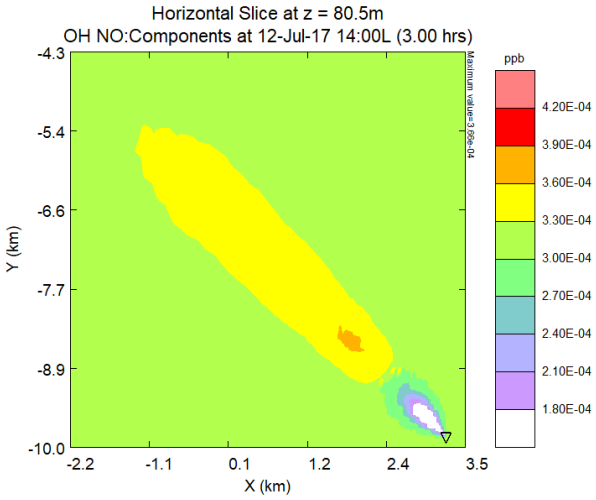

*Figure 25: OH field modelled with SCICHEM and plotted with the SCICHEM GUI at surface height (**A**) and at 80.5 m height (**B**) at the WtE plant. The emission source, emitting 3.02 g/s NO and 0.016 g/s CH_3CHO at a stack height of 80 m, is indicated by the symbol ∇. The full SCICHEM chemistry file ("fullchem_ae5_SW") was used, with the atmospheric chemical background described in Table 16 in Appendix 3.*

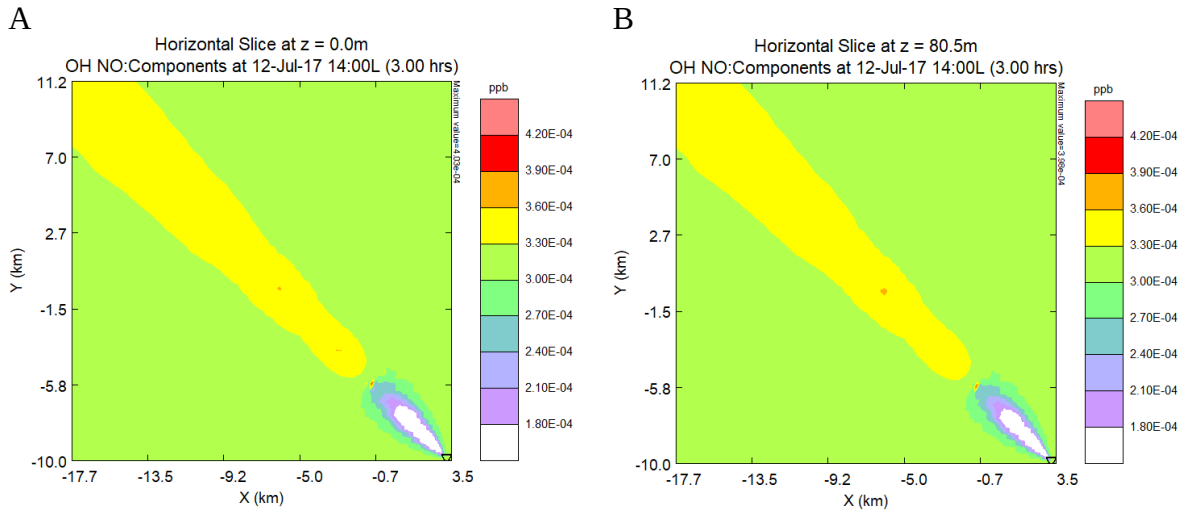

*Figure 26: OH field modelled with SCICHEM and plotted with the SCICHEM GUI at surface height (**A**) and at 80.5 m height (**B**) at the WtE plant. The emission source, emitting 30.2 g/s NO and 0.016 g/s CH_3CHO at a stack height of 80 m, is indicated by the symbol ∇. The full SCICHEM chemistry file ("fullchem_ae5_SW") was used, with the atmospheric chemical background described in Table 16 in Appendix 3.*

3.3.3 Summary Case Study 3a

Table 6 contains an overview of the NO_2, NO, O_3 and OH fields that were obtained in case study 3a after emission of 3.02 g/s NO from the WtE plant. It shows that the highest VMR of NO_2 and NO can be observed close to the source. For O_3 and OH, a depletion is observed close to the source. However, OH formation occurs close to the source as well. The different reactions and their roles in the formation of the observed OH field are shown in Table 7. Different emissions were found to result in different OH fields. An overview of the results obtained after changing the emissions is shown in Table 8.

Table 6: Overview of the NO_2, NO, O_3 and OH fields at surface level and 80.5 m height obtained after emission of 3.02 g/s NO at the WtE plant.

Field	Surface level	80.5 m height
NO_2	- Highest VMR (3.02 ppb) close to the source. - Field spanning a distance of 10 km.	- Highest VMR (39.5 ppb) close to the source. - Field spanning a distance of 10 km.
NO	- Highest VMR (3.87 ppb) close to the source. - Field spanning a distance of 6 km.	- Highest VMR ($3.21 \cdot 10^4$ ppb) close to the source. - Field spanning a distance of 6 km.
O_3	- A depletion area close to the source with a maximum depletion of 9% compared to ambient level.	- A depletion area close to the source with a maximum depletion of 100% compared to ambient level.
OH	- A depletion area close to the source with a maximum depletion of 46% compared to ambient level. - Area of formation close to the source with a maximum formation of 34% compared to ambient level.	- A depletion area close to the source with a maximum depletion of 100% compared to ambient level. - Area of formation close to the source with a maximum formation of 31% compared to ambient level.

Table 7: Reactions and their role found to be of importance for the OH field in the combustion plume at the WtE plant after emission of 3.02 g/s NO.

Reaction	**Role**
$HO_2 + NO \rightarrow OH + NO_2$ (R12)	Main part of OH formation
$HO_2 + O \rightarrow OH + O_2$ (R14)	OH formation
$HO_2 + O_3 \rightarrow OH + 2\ O_2$ (R15)	OH formation
$O_3 + NO \rightarrow NO_2 + O_2$ (R8)	Limit OH formation OH depletion
$OH + NO_2 + M \rightarrow HNO_3 + M$ (R13)	Limit OH formation OH depletion
$OH + NO + M \rightarrow HONO + M$ (R16)	OH depletion

Table 8: Overview of the OH fields at surface level and 80.5 m height obtained for different emission scenarios at the WtE plant.

Emissions (g/s)	**Surface level**	**80.5 m height**
NO: 3.02	- A depletion area close to the source with a maximum depletion of 46% compared to ambient level. - Area of formation close to the source with a maximum formation of 34% compared to ambient level.	- A depletion area close to the source with a maximum depletion of 100% compared to ambient level. - Area of formation close to the source with a maximum formation of 31% compared to ambient level.
NO: 3.02 **NO_2: 0.00302**	- Reduced OH formation further downwind. - Less OH depletion close to the source.	- Reduced OH formation further downwind. - Less OH depletion close to the source.
NO: 3.02 **NO_2: 0.00302** **HONO: 0.000302**	- More OH formation downwind compared to NO and NO_2 emission case.	- More OH formation downwind compared to NO and NO_2 emission case.
NO: 3.02 **CH_3CHO: 0.016**	- OH formation is reduced by 8% compared to NO emission case.	- OH formation is reduced by 8% compared to NO emission case.
NO: 30.2	- A depletion area close to the source with a maximum depletion of 100% compared to ambient level.	- A depletion area close to the source with a maximum depletion of 100% compared to ambient level.

Emissions (g/s)	Surface level	80.5 m height
	- Area of formation starting at 6 km downwind, spanning a larger distance.	- Area of formation starting at 6 km downwind, spanning a larger distance.
NO: 30.2 **NO_2: 0.0302**	- Reduced OH formation further downwind. - Less OH depletion close to the source.	- Reduced OH formation further downwind. - Less OH depletion close to the source.
NO: 30.2 **NO_2: 0.0302** **HONO: 0.00302**	- More OH formation downwind compared to NO and NO_2 emission case.	- No effect compared to the NO and NO_2 emission case.
NO: 30.2 **CH_3CHO: 0.016**	- OH formation is reduced by 0.2% compared to NO emission case.	- OH formation is reduced by 1.0% compared to NO emission case.

3.4 Case Study 3b: Waste-to-Energy Plant Plume Chemistry Simulations (with Amines)

Figure 27A and B show the NO_2 field of the plume at surface level and at 80.5 m height, respectively, after emission of 3.02 g/s NO, 0.016 g/s CH_3CHO and 0.032 g/s PZ. The two fields are similar with the biggest differences within the first kilometer downwind from the source. At surface level (Figure 27A), the maximum VMR is 3.45 ppb. At 80.5 m height (Figure 27B), the maximum VMR is an order of magnitude larger: 37.2 ppb. However, further downwind, starting at 1 km downwind from the source, both fields have the same VMR, regardless of the measuring height. A similar pattern can be seen when looking at Figure 27C (surface level) and D (80.5 m height), after 30.2 g/s NO has been emitted. The highest VMR can be found close to the source at both measuring levels, but at surface level the highest VMR is 19.2 ppb, whereas it is 117.6 ppb at 80.5 m height. Moreover, when more NO is emitted, the entire NO_2 field is more elongated, with areas of higher VMRs spanning longer distances downwind from the source. The highest VMR of NO_2 was expected close to the source, since it is formed there by the reaction between NO and O_3 (R8).

The NO fields, after emission of 3.02 g/s NO, 0.016 g/s CH_3CHO and 0.032 g/s PZ, at surface level and 80.5 m height can be seen in Figure 28A and B, respectively. As is the case with the NO_2 fields (Figure 27A-B), the biggest differences between the measuring levels can be observed within the first kilometer downwind from the source. At surface level, the highest VMR (3.83 ppb) can be observed close to the source. The same applies at 80.5 m height, but there the highest VMR is $3.07 \cdot 10^4$ ppb, which is a factor $8 \cdot 10^3$ higher than at surface level. Similarly, when emitting 30.2 g/s NO, at surface level (Figure 28C) a maximum VMR of 48.8 ppb is observed, while at 80.5 m height (Figure 28D), this is $3.07 \cdot 10^5$ ppb. The difference between the maximum VMRs at surface level and at 80.5 m height can be explained by the fact that NO is emitted from the stack, which is 80 m high. After emission, the field is diluted resulting in lower VMRs at surface level. After emitting 30.2 g/s NO, the field does not dilute back to ambient levels within the 30 km distance considered (Figure 28C and D), whereas ambient VMRs are restored within 6 km downwind from the source when 3.02 g/s NO is emitted (Figure 28A and B). This is the result of only increasing the NO emission, while keeping the emission and background levels of all other species the same.

Figure 29A and B show the O_3 fields at surface level and 80.5 m height, respectively, after emission of 3.02 g/s NO, 0.016 g/s CH_3CHO and 0.032 g/s PZ. At both measuring levels, a depletion can be seen close to the source spanning a distance of 3.2 km downwind. At surface level (Figure 29A) the field is depleted down to 32 ppb, which is 2.4 ppb (7%) lower than the ambient VMR of 34.4 ppb. This depletion is the result of ozone titration, where the emitted NO reacts with O_3 forming NO_2 (R8). Further downwind, starting at 8.5 km downwind from the source, a formation of O_3 can be observed. However, this is an increase of 0.1 ppb (0.3%) compared to the ambient VMR. This slight increase can be explained by NO being more well-mixed with the background air, allowing O_3 formation. A similar field is formed at a height of 80.5 m. In this case O_3 is depleted to 15 ppb close to the source (i.e. 56% depletion relative to ambient O_3). This increased depletion can also be explained by ozone titration, since more NO is present to react with O_3. When looking at the O_3 fields at surface level (Figure 29C) and 80.5 m height (Figure 29D) after 30.2 g/s NO emission, fields with depletion near the source and formation further downwind can be observed again. However, as a result of the increased ozone titration (R8) due to the increased NO emission, the O_3 depletion spans a longer distance of 9.2 km. At surface level, the minimum VMR is 17 ppb (a 50% decrease relative to ambient O_3). At 80.5 m height a total O_3 depletion can be observed. Moreover, because it takes longer for the increased NO emission to be well-mixed with the ambient air, the formation of O_3 (i.e. 0.3 ppb (0.9%) increase compared to ambient levels) starts at 17 km downwind from the source.

Figure 30A and B show the OH fields at surface level and at 80.5 m height, respectively, after emission of 3.02 g/s NO, 0.016 g/s CH_3CHO and 0.032 g/s PZ. In both Figure 30A and B, a depletion of OH can be observed within 1.5 km downwind from the source. At surface level (Figure 30A), this is a depletion to $1.3 \cdot 10^{-4}$ ppb. This constitutes a 57% decrease relative to the ambient OH VMR of $3.04 \cdot 10^{-4}$ ppb. At 80.5 m height, a total depletion of OH can be observed, but this total depletion only spans a small area. This corresponds to the O_3 fields shown in Figure 29A and B, where only at 80.5 m height a total depletion occurs. A total O_3 depletion causes a total OH depletion, since O_3 is the most important precursor for OH close to the source (R5 and R7). At 1.8 km downwind from the source, OH formation can be observed over a distance of 5.4 km. This was found to be the result of HO_2 reacting with NO forming OH and NO_2 (R12). When increasing the NO emission to 30.2 g/s (Figure 30C and D), the OH depletion spans a longer distance of 6 km, since more O_3 is depleted over a longer distance as well (Figure 29C and D). Moreover, regardless of the measuring height, there are areas of total OH depletion. The area of formation starts at 7 km downwind from the source and spans at least 23 km

downwind from the source. This can be explained by the NO field also spanning a much larger distance (Figure 28C and D). The NO reacts with HO_2 forming OH (R12).

The PZNO fields are shown in Figure 31A-D. After emission of 3.02 g/s NO, 0.016 g/s CH_3CHO and 0.032 g/s PZ, fields spanning a distance of approximately 9 km can be observed, both at surface level (Figure 31A) and at 80.5 m height (Figure 31B). At surface level, the maximum VMR of PZNO is 0.207 ppt. At 80.5 m height, this is approximately a factor of 2 higher: 0.442 ppt. This difference is caused by the NO VMR being higher directly at the source at 80.5 m height (Figure 28B) than at surface level (Figure 28A). At surface level, the highest PZNO VMR can be observed at 1.2 km downwind from the source. At 80.5 m height, the highest VMR is found directly at the source. When emitting more NO (30.2 g/s), the maximum VMR of PZNO decreases to 0.0568 ppt at surface level (Figure 31C) and 0.0519 ppt at 80.5 m height (Figure 31D). This can be explained by the increased OH depletion which is caused by the higher NO emission (Figure 30C and D). OH is necessary for forming PZNR, which is the precursor in PZNO formation. The maximum PZNO VMR is therefore found further downwind from the source, at 1.5 km, regardless of the measuring height. The increased NO levels (Figure 28C and D) result in the area of PZNO formation spanning a larger distance downwind from the source. Due to the increased area of OH depletion, less PZNO can be formed near the source. The emitted PZ is therefore able to travel further downwind before all PZ has been converted into PZNO.

The $PZNO_2$ fields are shown in Figure 32A-D. After emission of 3.02 g/s NO, 0.016 g/s CH_3CHO and 0.032 g/s PZ, $PZNO_2$ fields spanning a distance of 16 km downwind from the source can be observed. At surface level (Figure 32A), the highest VMR of 0.134 ppt can be found at 1.6 km downwind from the source. At 80.5 m height (Figure 32B), the highest VMR can be found at 2.3 km downwind, but it has decreased to 0.126 ppt. This slight decrease could be the result of NO and NO_2 competing to react with PZNR. Since the NO/NO_2 ratio is much higher at 80.5 m height than at surface level, less $PZNO_2$ is formed at that 80.5 m height. When increasing the NO emission to 30.2 g/s, the maximum VMR of $PZNO_2$ decreases to 0.0500 ppt at surface level (Figure 32C) and 0.0499 ppt at 80.5 m height (Figure 32D). Moreover, the formation of $PZNO_2$ starts further downwind and the maximum VMR can be observed at 3.5 km downwind from the source, regardless of the measuring height. As was the case for PZNO, this can be explained by more OH being depleted as a result of increased NO emission.

Under the NO emission conditions (i.e. 3.02 g/s) assumed for the WtE plant, it was found that after a PZ emission of 0.032 g/s a maximum of 0.97 ng/m^3 nitrosamine and 0.72 ng/m^3 nitramines was formed at surface level at 1.2 and 1.6 km downwind from the source, respectively. Appendix 4 contains the conversions from volume mixing ratio (in ppt) to concentration (in ng/m^3). Under this scenario and the assumption that the concentrations determined represent a yearly average, the limit of 0.3 ng/m^3 for nitrosamines and nitramines set by the Norwegian Institute of Public Health is exceeded (Norwegian Institute of Public Health, 2016). However, ambient concentrations of background species do not remain constant over time, as is assumed in these simulations. Therefore, VMRs may be higher or lower in reality than the modelled VMRs. Most important is, however, that the wind is not constant throughout the year and the variation in wind speed and direction, as well as other meteorological factors, are likely to cause more dispersion of PZ. Therefore, the assumption that the simulated values reported above for PZNO and $PZNO_2$ represent an annual average is unlikely and the actual meteorology will probably result in lower PZNO and $PZNO_2$ concentrations.

Under low NO emissions, the highest PZNO and $PZNO_2$ VMRs are observed at 1 to 1.5 km downwind from the source. However, PZNO can also be directly emitted from the stack in addition to being formed in the field (Tønnesen, 2011). This could result in a build-up of PZNO near the source. When $2.1 \cdot 10^{-4}$ g/s PZNO is emitted in addition to 3.02 g/s NO, 0.016 g/s CH_3CHO and 0.032 g/s PZ, the highest PZNO VMR of 0.327 ppt (i.e. 1.54 ng/m^3, see Appendix 4 for the conversion from volume mixing ratio to concentration) can be found at approximately 1 km downwind from the source at surface level (Figure 33A). If looking at a height of 80.5 m (Figure 33B), a maximum VMR of 557.5 ppt can be observed. This shows that the emitted PZNO becomes diluted vertically by a factor of $1.7 \cdot 10^3$. However, near the source, the concentration at surface level is still close to the limit set by the Norwegian Institute of Public Health (Norwegian Institute of Public Health, 2016).

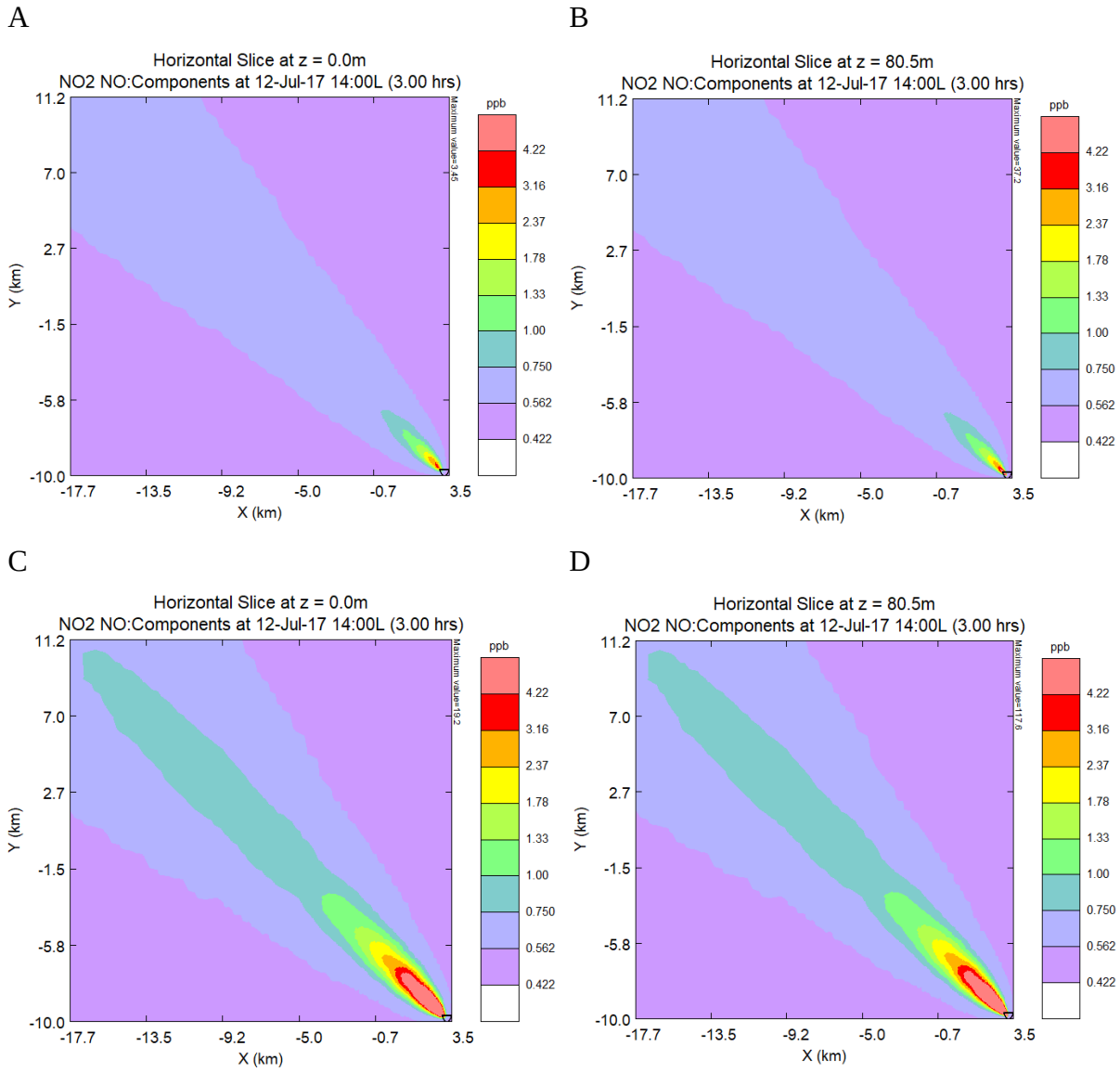

*Figure 27: NO_2 fields modelled with SCICHEM and plotted with the SCICHEM GUI after emission of 0.032 g/s PZ, 0.016 g/s CH_3CHO and either 3.02 g/s NO (**A** and **B**) or 30.2 g/s NO (**C** and **D**) at the WtE plant. Simulated at surface height (**A** and **C**) and at 80.5 m height (**B** and **D**). The emission source is indicated by the symbol ∇. The full SCICHEM chemistry file ("fullchem_ae5_SW") was used, with the atmospheric chemical background described in Table 16 in Appendix 3.*

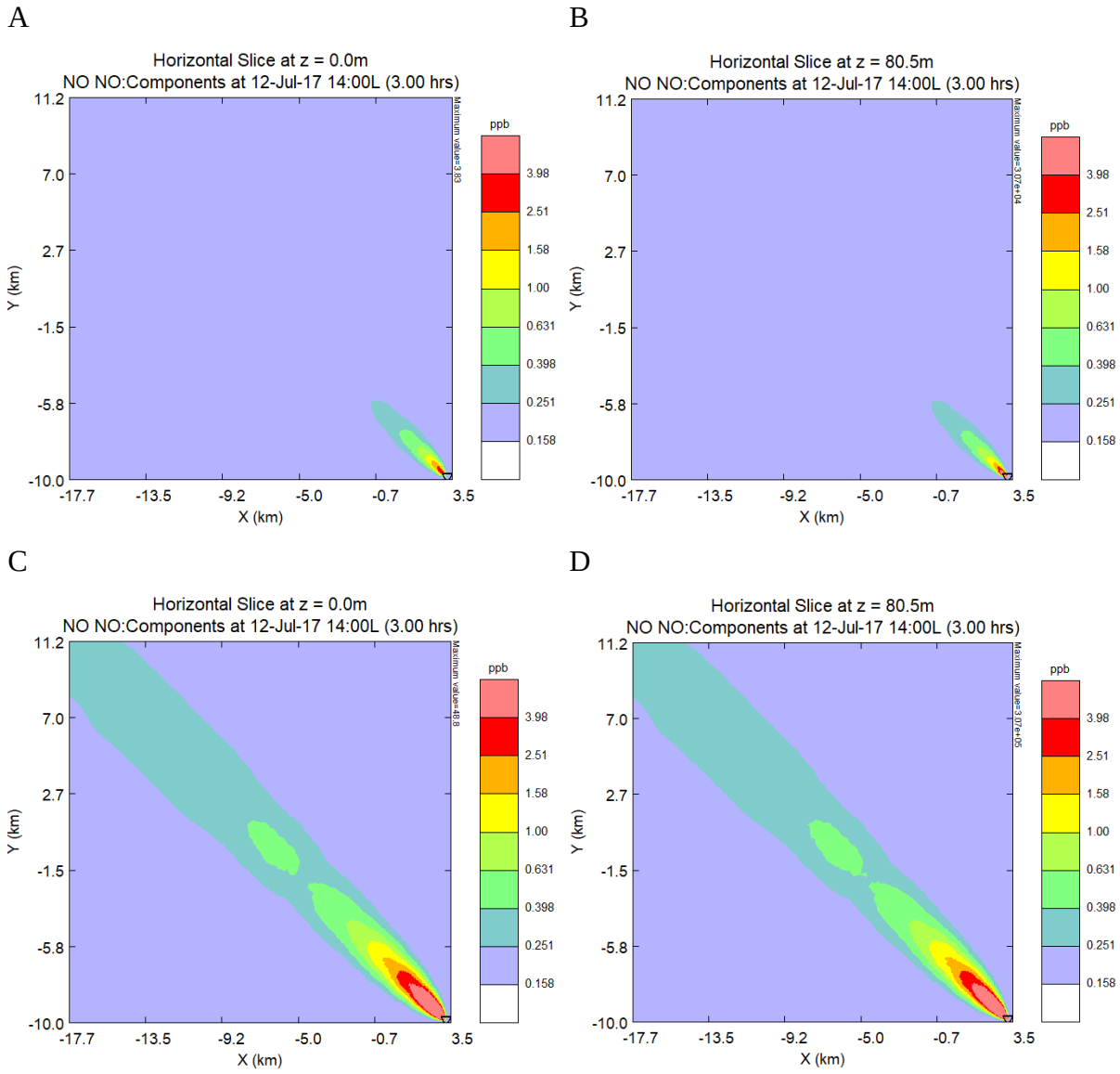

*Figure 28: NO fields modelled with SCICHEM and plotted with the SCICHEM GUI after emission of 0.032 g/s PZ, 0.016 g/s CH_3CHO and either 3.02 g/s NO (**A** and **B**) or 30.2 g/s NO (**C** and **D**) at the WtE plant. Simulated at surface height (**A** and **C**) and at 80.5 m height (**B** and **D**). The emission source is indicated by the symbol ∇. The full SCICHEM chemistry file ("fullchem_ae5_SW") was used, with the atmospheric chemical background described in Table 16 in Appendix 3.*

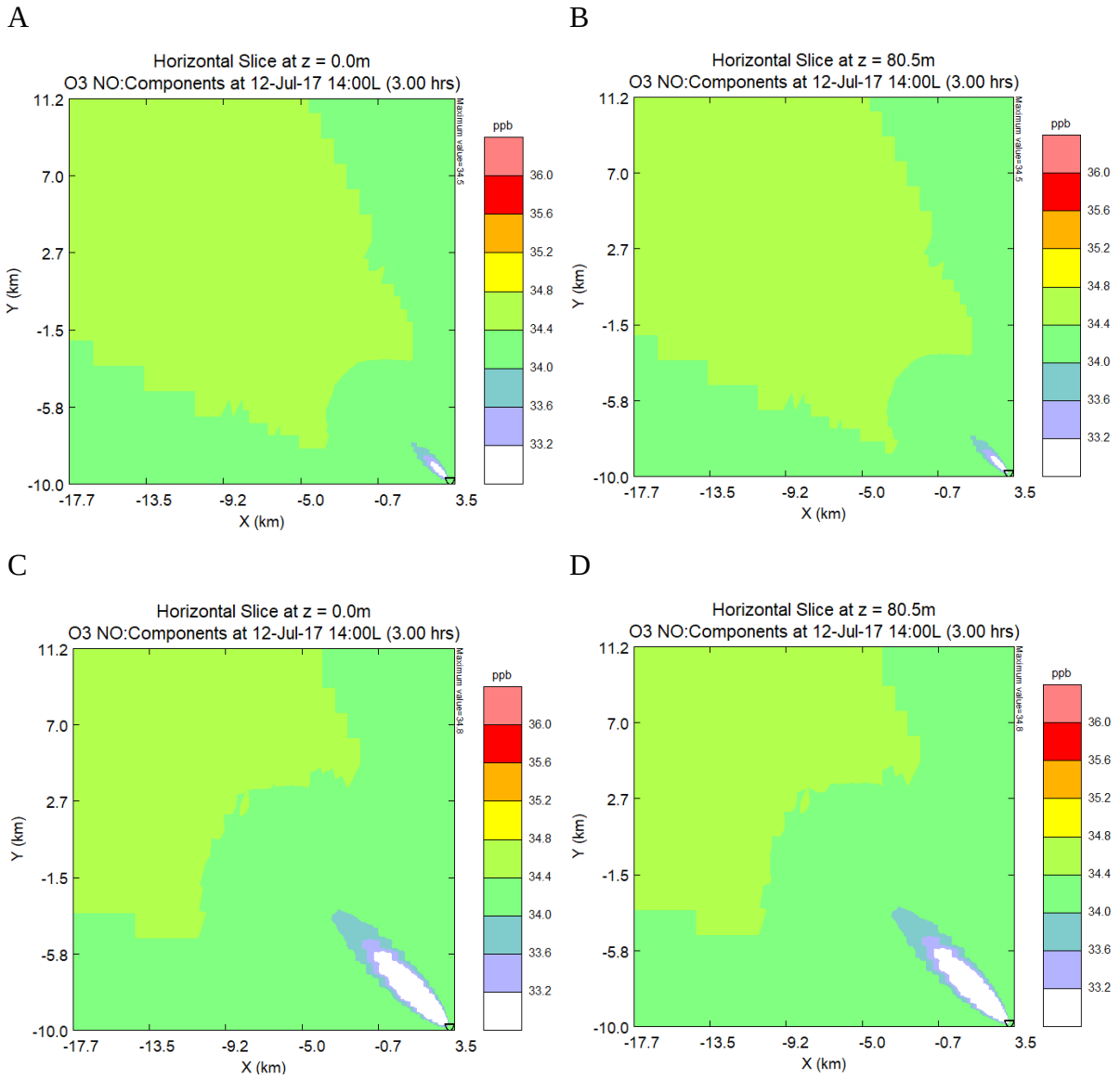

*Figure 29: O_3 fields modelled with SCICHEM and plotted with the SCICHEM GUI after emission of 0.032 g/s PZ, 0.016 g/s CH_3CHO and either 3.02 g/s NO (**A** and **B**) or 30.2 g/s NO (**C** and **D**) at the WtE plant. Simulated at surface height (**A** and **C**) and at 80.5 m height (**B** and **D**). The emission source is indicated by the symbol ∇. The full SCICHEM chemistry file ("fullchem_ae5_SW") was used, with the atmospheric chemical background described in Table 16 in Appendix 3.*

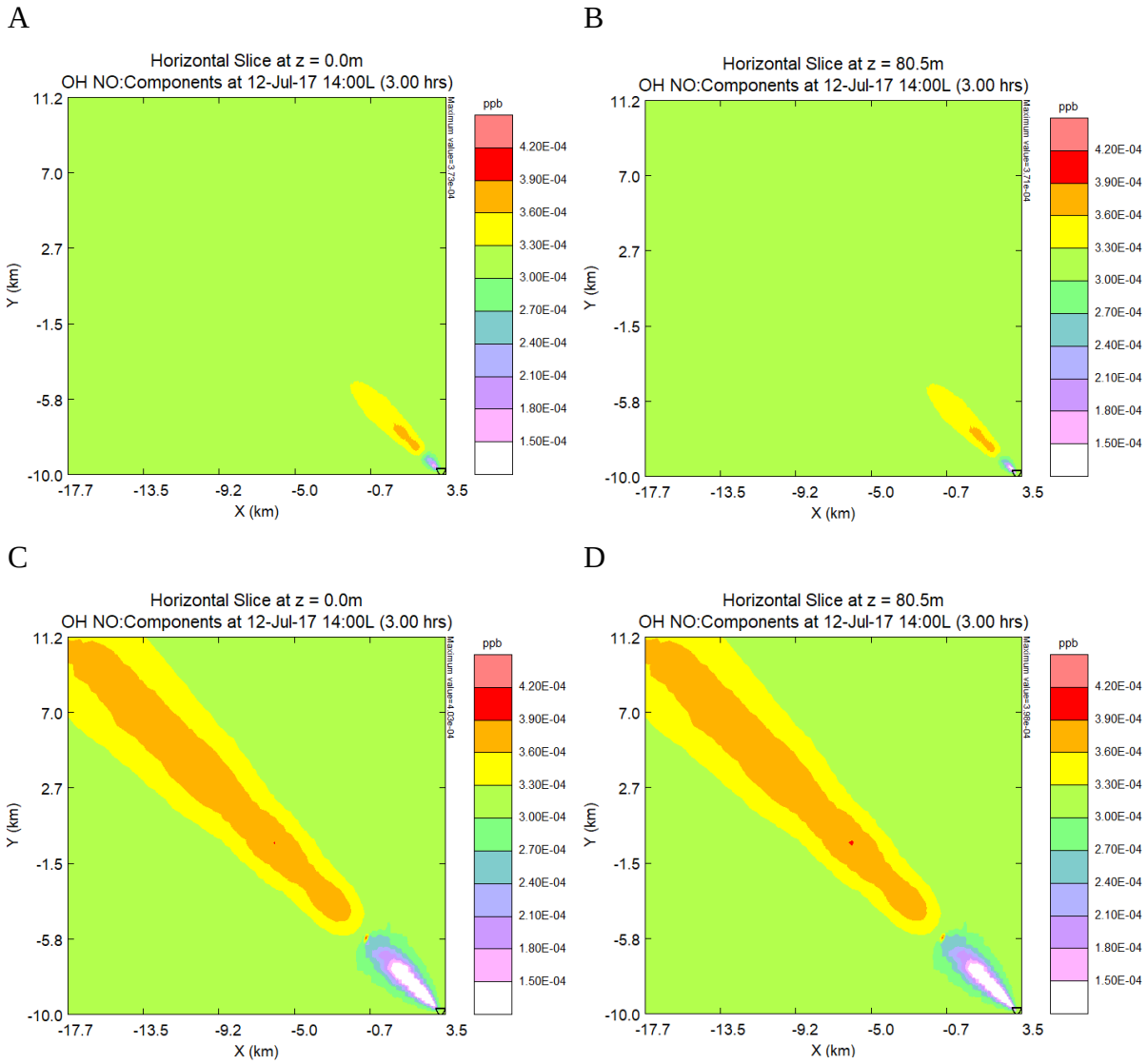

*Figure 30: OH fields modelled with SCICHEM and plotted with the SCICHEM GUI after emission of 0.032 g/s PZ, 0.016 g/s CH_3CHO and either 3.02 g/s NO (**A** and **B**) or 30.2 g/s NO (**C** and **D**) at the WtE plant. Simulated at surface height (**A** and **C**) and at 80.5 m height (**B** and **D**). The emission source is indicated by the symbol ∇. The full SCICHEM chemistry file ("fullchem_ae5_SW") was used, with the atmospheric chemical background described in Table 16 in Appendix 3.*

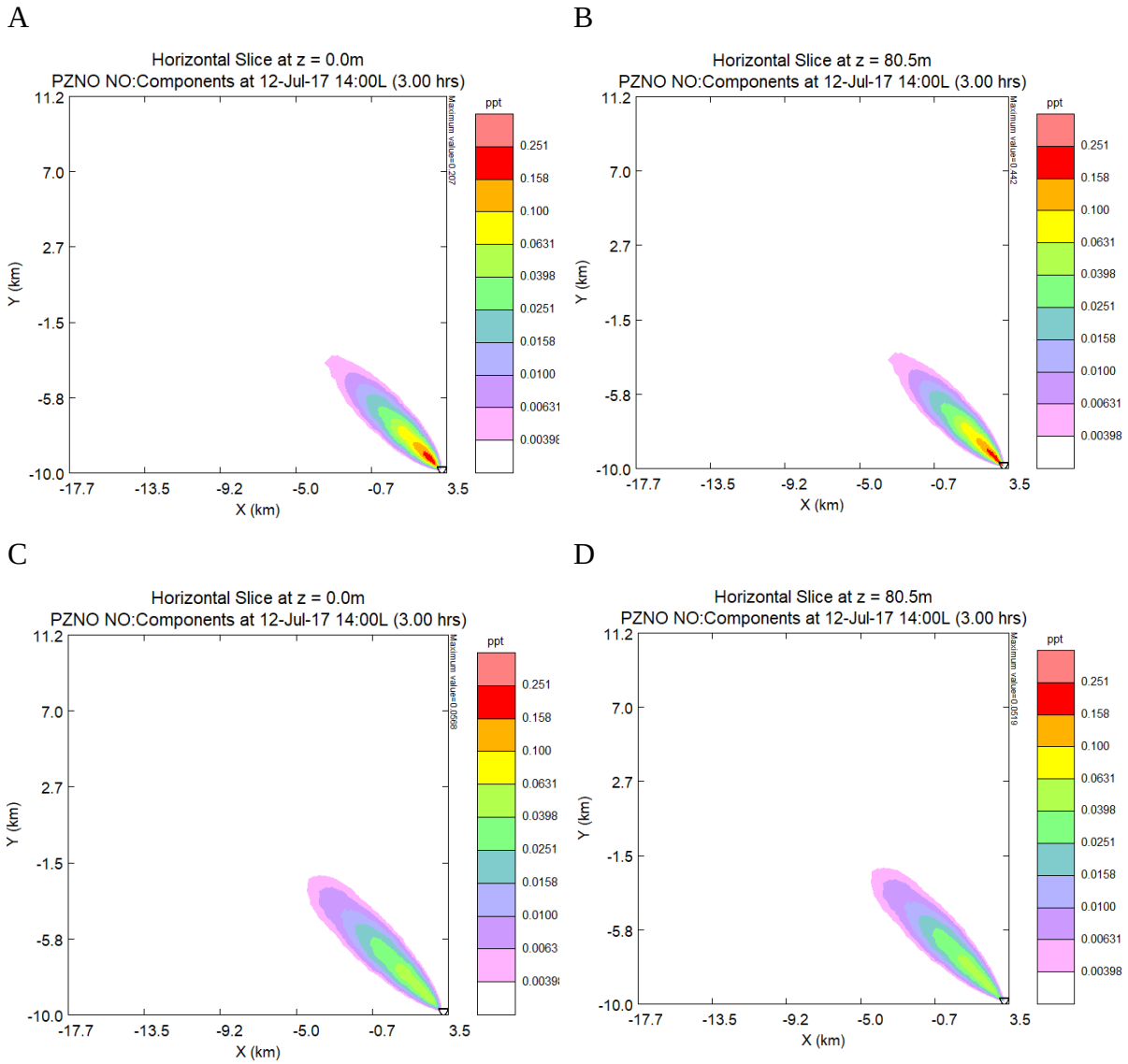

*Figure 31: Piperazine nitrosamine (PZNO) fields modelled with SCICHEM and plotted with the SCICHEM GUI after emission of 0.032 g/s PZ, 0.016 g/s CH_3CHO and either 3.02 g/s NO (**A** and **B**) or 30.2 g/s NO (**C** and **D**) at the WtE plant. Simulated at surface height (**A** and **C**) and at 80.5 m height (**B** and **D**). The emission source is indicated by the symbol ∇. The full SCICHEM chemistry file ("fullchem_ae5_SW") was used, with the atmospheric chemical background described in Table 16 in Appendix 3.*

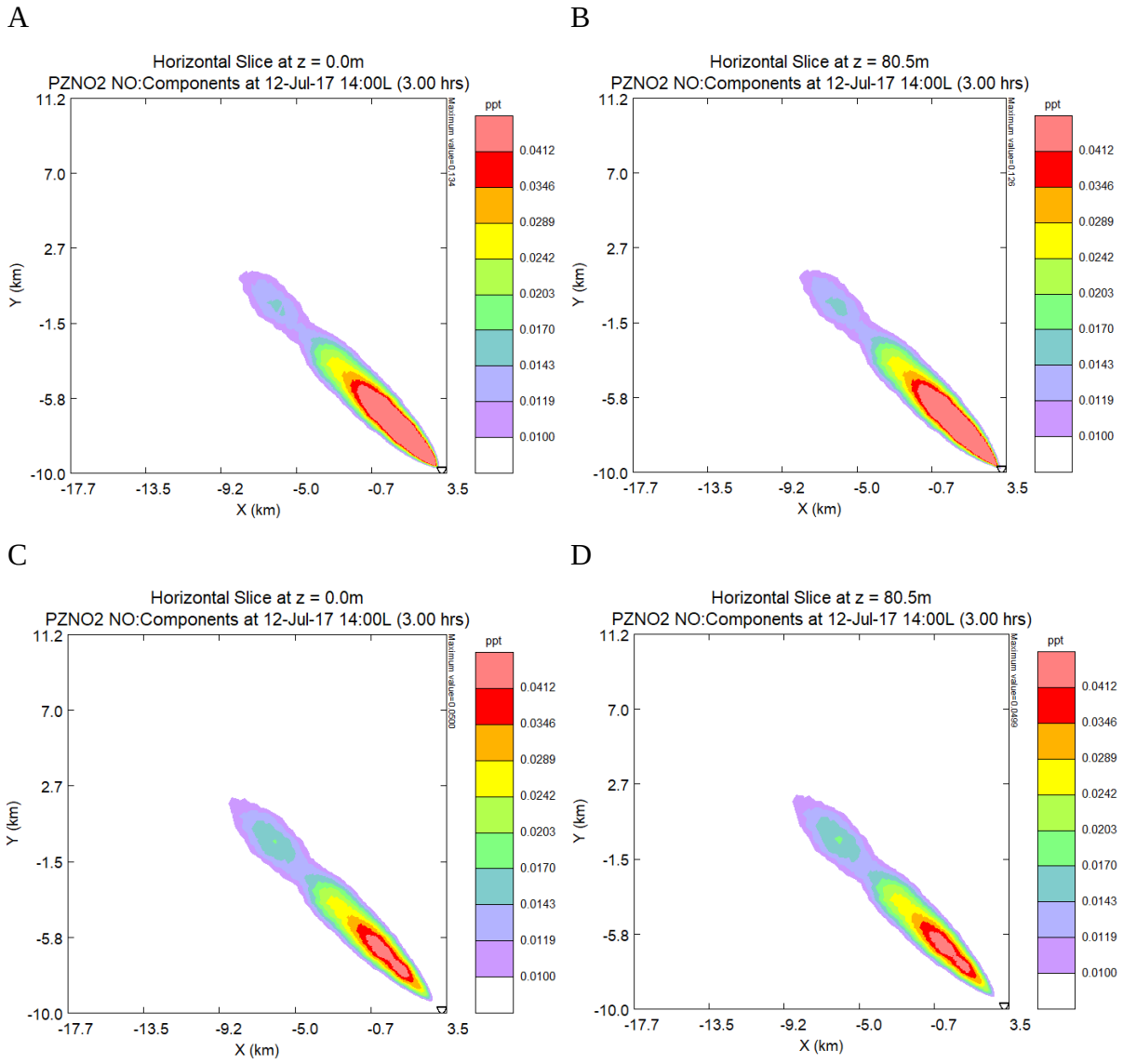

*Figure 32: Piperazine nitramine ($PZNO_2$) fields modelled with SCICHEM and plotted with the SCICHEM GUI after emission of 0.032 g/s PZ, 0.016 g/s CH_3CHO and either 3.02 g/s NO (**A** and **B**) or 30.2 g/s NO (**C** and **D**) at the WtE plant. Simulated at surface height (**A** and **C**) and at 80.5 m height (**B** and **D**). The emission source is indicated by the symbol ∇. The full SCICHEM chemistry file ("fullchem_ae5_SW") was used, with the atmospheric chemical background described in Table 16 in Appendix 3.*

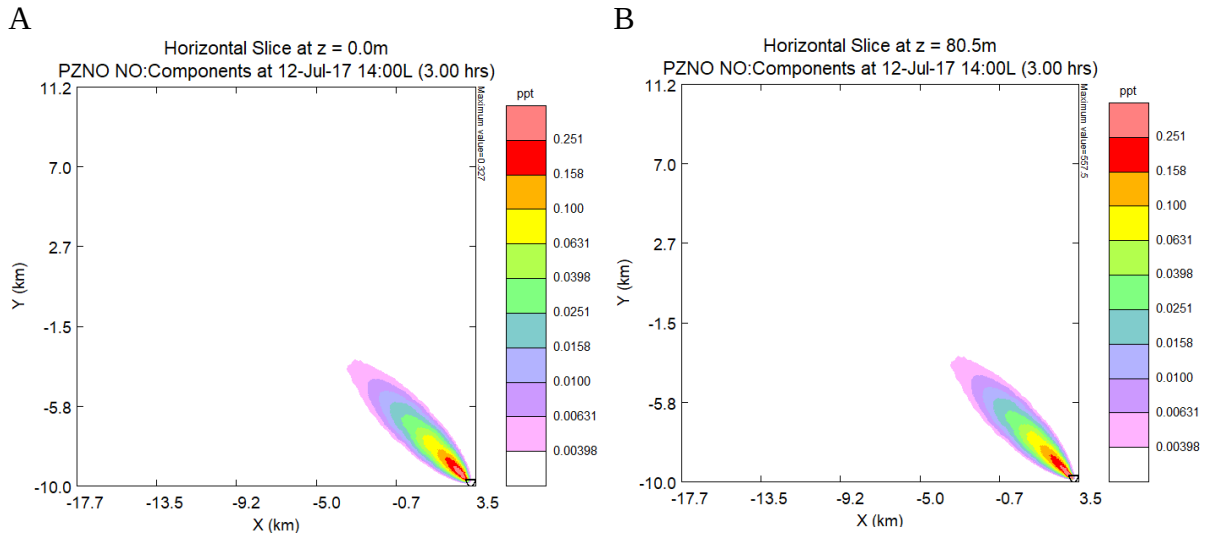

*Figure 33: Piperazine nitrosamine (PZNO) fields modelled with SCICHEM and plotted with the SCICHEM GUI after emission of 0.032 g/s PZ, 0.016 g/s CH_3CHO, 3.02 g/s NO and $2.1 \cdot 10^{-4}$ g/s PZNO at the WtE plant. Simulated at surface height (**A**) and at a height of 80.5 m (**B**). The emission source is indicated by the symbol ∇. The full SCICHEM chemistry file ("fullchem_ae5_SW") was used, with the atmospheric chemical background described in Table 16 in Appendix 3.*

3.4.1 Summary Case Study 3b

Table 9 shows an overview of the NO_2, NO, O_3 and OH fields that were obtained in case study 3b after emission of 3.02 g/s NO and 0.032 g/s PZ from the WtE plant. It shows that the highest VMR of NO_2 and NO can be observed close to the source. A depletion of O_3 and OH is observed immediately near the source. However, OH formation is also observed shortly after the depletion area and still relatively close to the source. A similar observation can be made looking at Table 10, where the NO emission has been increased to 30.2 g/s. Finally, Table 11 shows an overview of the maximum VMRs of PZNO and $PZNO_2$ under different emission scenarios. It shows that the highest VMRs of PZNO and $PZNO_2$ can be found near the source and that these values are close to the limit set by the Norwegian Institute of Public Health (Norwegian Institute of Public Health, 2016).

Table 9: Overview of the NO_2, NO, O_3 and OH fields at surface level and 80.5 m height obtained after emission of 3.02 g/s NO and 0.032 g/s PZ at the WtE plant.

Field	Surface level	80.5 m height
NO_2	- Highest VMR (3.45 ppb) close to the source.	- Highest VMR (37.2 ppb) close to the source.
NO	- Highest VMR (3.83 ppb) close to the source.	- Highest VMR ($3.07 \cdot 10^4$ ppb) close to the source.
O_3	- A depletion area close to the source with a maximum depletion of 7% compared to ambient level.	- A depletion area close to the source with a maximum depletion of 56% compared to ambient level.
OH	- A depletion area close to the source with a maximum depletion of 57% compared to ambient level. - Subsequent area of formation immediately after the depletion.	- A depletion area close to the source with a maximum depletion of 100% compared to ambient level. - Subsequent area of formation immediately after the depletion.

Table 10: Overview of the NO_2, NO, O_3 and OH fields at surface level and 80.5 m height obtained after emission of 30.2 g/s NO and 0.032 g/s PZ at the WtE plant.

Field	Surface level	80.5 m height
NO_2	- Highest VMR (19.2 ppb) close to the source. - More elongated field.	- Highest VMR (117.6 ppb) close to the source. - More elongated field.
NO	- Highest VMR (48.8 ppb) close to the source.	- Highest VMR ($3.07 \cdot 10^5$ ppb) close to the source.
O_3	- A depletion area close to the source with a maximum depletion of 50% compared to ambient level.	- A depletion area close to the source with a maximum depletion of 100% compared to ambient level.
OH	- A depletion area close to the source with a maximum depletion of 100% compared to ambient level. - Subsequent area of formation immediately after the depletion.	- A depletion area close to the source with a maximum depletion of 100% compared to ambient level. - Subsequent area of formation immediately after the depletion.

Table 11: Overview of the maximum volume mixing ratios (in ppt) and concentrations (in ng/m^3) if applicable, that were obtained from the PZNO and $PZNO_2$ fields at surface level and at 80.5 m height obtained for different emission scenarios at the WtE plant.

Emissions (g/s)	**PZNO surface level**	**PZNO 80.5 m height**	**$PZNO_2$ surface level**	**$PZNO_2$ 80.5 m height**
NO: 3.02 **CH_3CHO: 0.016** **PZ: 0.032**	- Maximum VMR: 0.207 ppt (= 0.97 ng/m^3) at 1.2 km downwind.	- Maximum VMR: 0.442 ppt directly at the source.	- Maximum VMR: 0.134 ppt (= 0.27 ng/m^3) at 1.3 km downwind.	- Maximum VMR: 0.126 ppt at 2.3 km downwind.
NO: 30.2 **CH_3CHO: 0.016** **PZ: 0.032**	- Maximum VMR: 0.0568 ppt at 1.5 km downwind.	- Maximum VMR: 0.0519 ppt at 1.5 km downwind.	- Maximum VMR: 0.0500 ppt at 3.5 km downwind	- Maximum VMR: 0.0499 ppt at 3.5 km downwind.
NO: 3.02 **CH_3CHO: 0.016** **PZ: 0.032** **PZNO: $2.1 \cdot 10^{-4}$**	- Maximum VMR: 0.327 ppt (= 1.54 ng/m^3) around 1 km downwind.	- Maximum VMR: 557.5 ppt around 1 km downwind.	-	-

3.5 SCICHEM and Volumetric Particle Approach Model Comparison

Figure 34A shows the NO_2 field in $\mu g/m^3$ which was modelled using the Volumetric Particle Approach (VPA) Model. This field is a spatial average over the distance between surface level and 50 m height. It shows that close to the source, the highest concentration of NO_2 can be found. This can be explained by the rapid conversion of NO (in reaction with O_3) to NO_2 (R8). The area with a high NO_2 concentration spans approximately 4 km, before the NO_2 concentration decreases again. The VPA model can only produce spatially averaged fields as output. SCICHEM, on the other hand, is not able to do this. Therefore, the NO_2 fields have been plotted at surface level (wind speed 4.38 m/s), as can be seen in Figure 34B, as well as at 25 m height (wind speed 5.2 m/s) and at 50 m height (wind speed 6.10 m/s), which can be seen in Figure 34C and Figure 34D, respectively. Averaging the highest concentrations in Figure 34B-D results in an average highest concentration of approximately 2.96 $\mu g/m^3$. This is a factor of 2.7 lower than the average highest concentration of 8 $\mu g/m^3$ determined using the VPA model, which can be seen in Figure 34A. The field from the VPA model shows that the highest concentration can be found at around 2 km downwind from the source (Figure 34A). In the fields formed using SCICHEM, however, the highest concentration can be found immediately at the source (Figure 34B-D). Moreover, the fields formed using SCICHEM (Figure 34B-D) are diluting much more quickly than the field from the VPA model (Figure 34A). The average concentration calculated from Figure 34B-D at 2 km downwind was found to be approximately 1.8 $\mu g/m^3$, at 4 km downwind the average decreased to 1.4 $\mu g/m^3$ and at 6 km downwind the average was down to 1.2 $\mu g/m^3$. By contrast, the concentrations shown in Figure 34A are approximately 7 $\mu g/m^3$ at 2 km downwind, 8 $\mu g/m^3$ at 4 km downwind and 6 $\mu g/m^3$ at 6 km downwind. This can be explained by the fact that the VPA model does not start mixing immediately at the source, but at a certain distance downwind. Consequently, in the VPA model the reaction between NO and O_3 which forms NO_2 is delayed. SCICHEM, on the other hand, appears to start mixing at the source, and therefore NO reacts immediately with O_3 forming NO_2 (R8). It can be observed that the VPA data visualization by MATLAB gradually decreases concentrations, as it has a range of colors between two concentration levels. The SCICHEM GUI is not able to do this and has very distinct transitions between the concentration levels, reducing the level of detail. In the VPA model the background is separately but continuously evolved by a three-dimensional grid-based Eulerian model with a horizontal grid resolution of

1 km^2 and it is therefore changing slowly along the wind direction. In SCICHEM, the background is assumed to be completely constant.

A

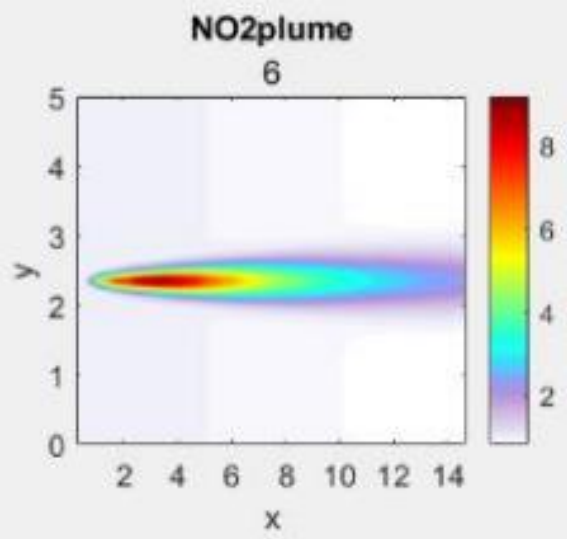

B

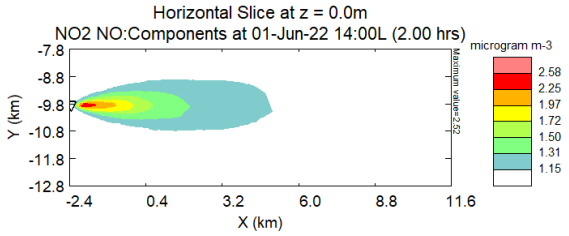

C

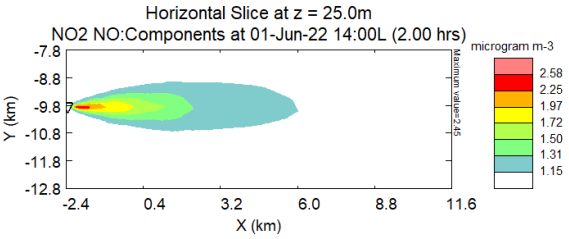

D

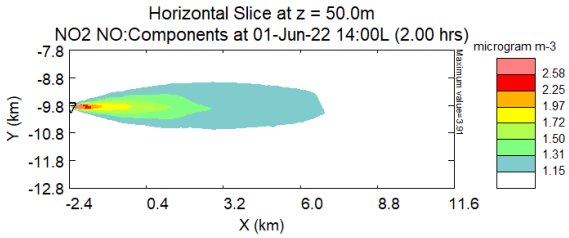

Figure 34: NO_2 fields (in $\mu g/m^3$) at 14:00 h local time, after emission of 3.013 g/s NO at stack height of 75 m at the WtE plant. ***A****) field modelled using the Volumetric Particle Approach model. This field is a spatially averaged field over the distance from surface level to 50 m height.* ***B****) field modelled with SCICHEM and plotted with the SCICHEM GUI at surface level.* ***C****) same as B) but at 25 m height.* ***D****) same as B) but at 50 m height. For the fields shown in B-D, the multi-component input file as shown in Figure 43 in Appendix 2 was used. Note the difference in the color bars between the field modelled using the Volumetric Particle Approach model (A) and the fields modelled using SCICHEM (B-D).*

Figure 35A shows the NO field modelled by Dr. Massimo Cassiani using the VPA model. It shows that the highest concentration, i.e. approximately 15 $\mu g/m^3$, can be found close to the source. This is as expected, since NO is emitted at a rate of 3.013 g/s by the source. Moreover, NO is quickly oxidized to NO_2 in the atmosphere, therefore leading to a rapid decrease of the NO concentration (United States Environmental Protection Agency, 1999). Because the field shown in Figure 35A is an average over the distance from surface level to 50 m height, it is compared to the average of the fields from SCICHEM at surface level, 25 m height and 50 m height as shown in Figure 35B-D, respectively. The fields formed using SCICHEM all show the highest concentration close to the source as well. The average highest concentration was found to be 11.78 $\mu g/m^3$, which is a factor 1.3 lower than the highest value found using the VPA model. This difference can be explained by the fact that SCICHEM appears to start mixing the emission and the background air immediately at the source, whereas the VPA model starts mixing further away. Therefore, SCICHEM assumes that NO reacts immediately at the source (e.g. with O_3 forming NO_2 (R8)) resulting in a lower NO concentration. The field formed using the VPA model (Figure 35A) changes rapidly and the concentration is between 3 and 4 $\mu g/m^3$ at approximately 5 km downwind. Afterwards, the NO concentration is low and slowly varying between approximately 2 $\mu g/m^3$ on the plume centerline at 6 km and about 0.5 $\mu g/m^3$ at 14 km and fading towards the background (about 0.18 $\mu g/m^3$) at the plume edges. The SCICHEM GUI is not able to gradually change concentration levels and this means that within one concentration level, e.g. from 0.178 to 0.316 $\mu g/m^3$, it is not possible to see whether the concentration approaches 0.178 or 0.316 $\mu g/m^3$. This also means that the SCICHEM GUI is not able to show a field as soon as it has dropped in the lowest concentration range on the scale, even though there might still be a perturbation compared to the ambient concentration. The average concentration at 2 km downwind in the SCICHEM fields (Figure 35B-D) was determined to be approximately 1.9 $\mu g/m^3$. At 4 km it was determined to be approximately 0.5 $\mu g/m^3$ and at 6 km downwind, it was approximately 0.3 $\mu g/m^3$. In the field simulated using the VPA model (Figure 35A), these concentrations were found to be approximately 8 $\mu g/m^3$ at 2 km downwind, 4 $\mu g/m^3$ at 4 km downwind and 2 $\mu g/m^3$ at 6 km downwind. This is higher than what SCICHEM predicts, which can again be explained by the fact that SCICHEM starts mixing the emitted gases and the background air earlier than the VPA model.

A

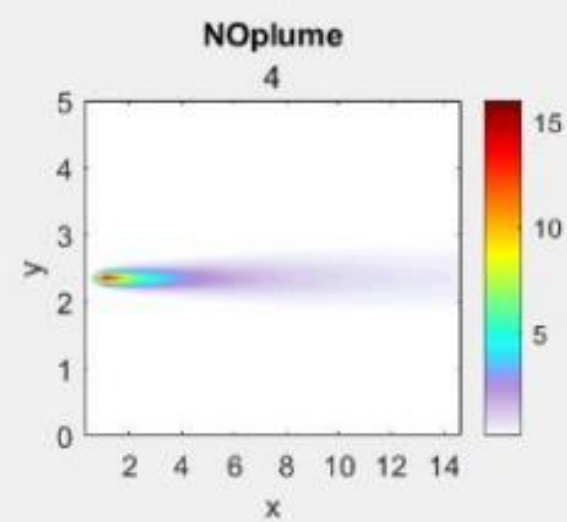

B

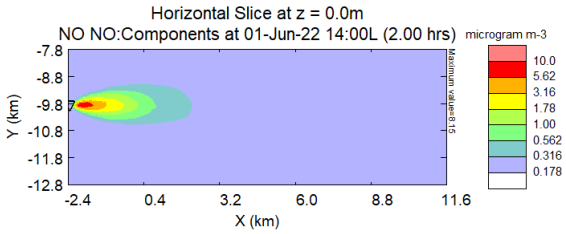

C

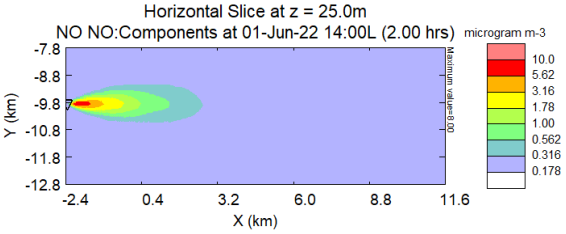

D

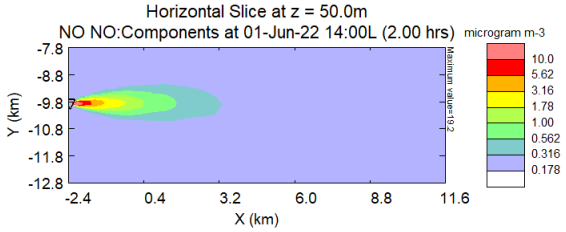

Figure 35: NO fields (in µg/m^3) at 14:00 h local time, after emission of 3.013 g/s NO at stack height of 75 m at the WtE plant. ***A****) field modelled using the Volumetric Particle Approach model. This field is a spatially averaged field over the distance from surface level to 50 m height.* ***B****) field modelled with SCICHEM and plotted with the SCICHEM GUI at surface level.* ***C****) same as B) but at 25 m height.* ***D****) same as B) but at 50 m height. For the fields shown in B-D, the multi-component input file as shown in Figure 43 in Appendix 2 was used. Note the difference in the color bars between the field modelled using the Volumetric Particle Approach model (A) and the fields modelled using SCICHEM (B-D).*

Figure 36A shows the O_3 field that was formed using the VPA model. It shows a relative depletion to less than 60 $\mu g/m^3$ O_3 between 2 to 4 km downwind from the source. Then the concentration gradually increases again to approximately 68 $\mu g/m^3$ at 14 km downwind from the source. By comparing this to the fields formed using SCICHEM (Figure 36B-D), it can be observed that the relative depletion in the SCICHEM fields is much less, at most 3 $\mu g/m^3$, compared to the ambient concentration. Moreover, the depletion occurs immediately at the source in the fields formed using SCICHEM (Figure 36B-D), whereas it takes place at 2 km downwind in the field from the VPA model (Figure 36A). This corresponds to the results found for NO and NO_2. SCICHEM modelled the highest concentrations of NO_2 (Figure 34B-D) and NO (Figure 35B-D) close to the source. The VPA model also modelled the highest NO (Figure 35A) close to the source. However, it modelled the highest NO_2 (Figure 34A) concentration at approximately 2 km downwind. The highest NO concentration at the source location is as expected since NO is emitted there and is then quickly oxidized to NO_2 (United States Environmental Protection Agency, 1999). SCICHEM appears to start mixing the emitted gases and the background air immediately upon emission. Consequently, the emitted NO reacts quickly with O_3 forming NO_2, as was described in R8. As a result, NO_2 is predominantly formed near the source, where O_3 depletion occurs. As the field travels further downwind and becomes more thoroughly mixed with the background, less NO reacts with O_3 forming NO_2. Then the NO_2 concentrations decrease, whereas the O_3 concentrations increase. The VPA model does something similar, the difference being that the VPA model does not start mixing immediately, but further downwind. Hence, the highest NO_2 concentration and the O_3 depletion shift further downwind. Looking at the average O_3 concentrations at several distances downwind in the SCICHEM fields (Figure 36B-D), it can be observed that at 2 km downwind the concentration is 69.3 $\mu g/m^3$, and at 4 and 6 km downwind the concentration is back up to 69.6 $\mu g/m^3$, which resembles the ambient concentration. The VPA field (Figure 36A) shows a distinctly different pattern: the concentration is depleted to approximately 61 $\mu g/m^3$ at 2 km, it is less than 60 $\mu g/m^3$ at 4 km and has increased back to approximately 63 $\mu g/m^3$ at 6 km downwind. This difference could be explained by the two models starting to mix the emitted and ambient gases at different times. As can be seen in Figure 36A, the O_3 field modelled using the VPA model shows O_3 formation on the edges of the field. The SCICHEM GUI is not able to simulate such plume edge details (Figure 36B-D). The formation of O_3 at the edges of the field is, however, important, because it also affects the OH field. Therefore, accurate plume simulations require a model that can clearly simulate plume edge details.

A

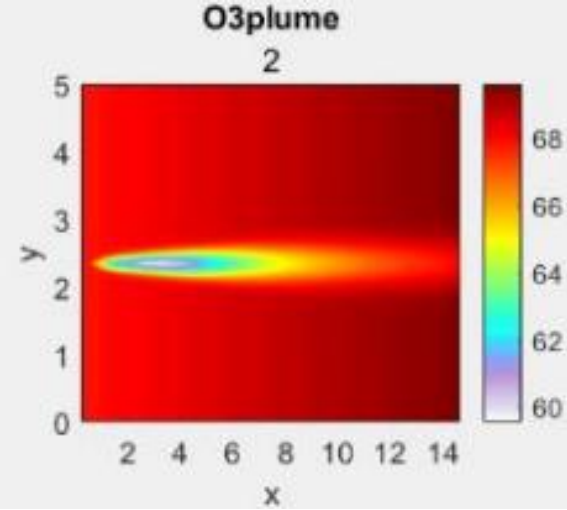

B

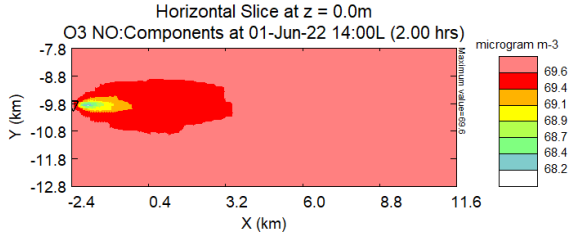

C

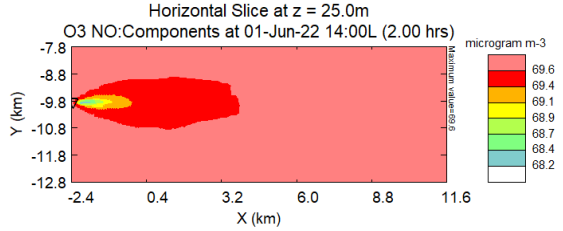

D

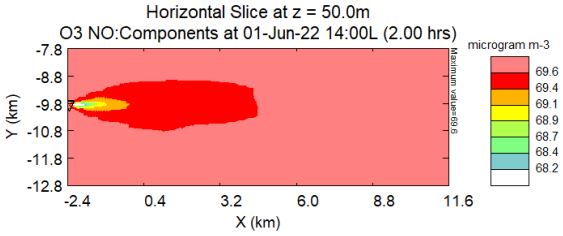

Figure 36: O_3 fields (in µg/m^3) at 14:00 h local time, after emission of 3.013 g/s NO at stack height of 75 m at the WtE plant. ***A****) field modelled using the Volumetric Particle Approach model. This field is a spatially averaged field over the distance from surface level to 50 m height.* ***B****) field modelled with SCICHEM and plotted with the SCICHEM GUI at surface level.* ***C****) same as B) but at 25 m height.* ***D****) same as B) but at 50 m height. For the fields shown in B-D, the multi-component input file as shown in Figure 43 in Appendix 2 was used. Note the difference in the color bars between the field modelled using the Volumetric Particle Approach model (A) and the fields modelled using SCICHEM (B-D).*

Figure 37A shows the OH field that was modelled using the VPA model. It shows an increase of OH relative to the ambient OH concentration directly at the source. Further downwind, from 4 to 8 km away from the source, a depletion in OH is modelled in the center of the field. From 6 kilometers downwind onwards, a wing-like pattern of increasing OH concentrations can be seen, where the increase of OH at the edges of the field is more pronounced than in the middle. The highest concentration of OH modelled is $3 \cdot 10^{-4}$ $\mu g/m^3$ and the area of depletion contains concentrations of less than $1.5 \cdot 10^{-4}$ $\mu g/m^3$. Comparing the VPA field (Figure 37A) to the fields simulated using SCICHEM (Figure 37B-D), a different pattern can be observed. SCICHEM does not predict any increase near the source location, but models the depletion close to the source. This is also different compared to what was predicted for OH in the previous WtE plant simulation (Figure 19), which first modelled a depletion followed by a formation close to the source. Since the changed parameters are not expected to have such a big influence and the ambient conditions are the same, the difference is most likely due to different chemical reactions being included in the chemistry schemes used. The increase that has been modelled by the VPA model is not expected and needs further investigation, especially since the VPA model does not simulate an increase in O_3 (Figure 36A), which is the precursor for OH (R5 and R7). The average highest concentration that is modelled by SCICHEM is $2.18 \cdot 10^{-4}$ $\mu g/m^3$, which is a factor 1.4 lower than the highest value modelled by the VPA model. The concentration in the area of depletion, however, is modelled by both the VPA model and SCICHEM as being less than $1.5 \cdot 10^{-4}$ $\mu g/m^3$. The SCICHEM fields (Figure 37B-D) span a distance of approximately 3 km, before the ambient concentration is restored. The field formed by the VPA model (Figure 37A), however, spans a distance of more than 14 km. Both the different position of the area of depletion as well as the difference in field length could be explained by SCICHEM mixing the emitted gases and the ambient air very quickly after emission, allowing the emitted NO to immediately react with O_3 forming NO_2 (R8). Consequently, O_3 is depleted near the source, preventing OH formation and causing an OH depletion near the source (R5 and R7). The immediate mixing of emitted and ambient gases also causes the NO to be more evenly mixed with the ambient atmosphere at a shorter distance away from the source, resulting in a ‘restoration’ of the ambient levels closer to the source and thus leading to a shorter field. The VPA model does not start mixing until a certain distance away from the source. This results in an area of depletion further downwind and a longer field. Moreover, because of the rapid mixing in SCICHEM, the depletion areas in the OH fields from SCICHEM (Figure 37B-D) are much smaller than in the VPA OH field (Figure 37A).

Comparing the average OH concentrations of the SCICHEM fields (i.e. at 2 km downwind: $2.0 \cdot 10^{-4}$ $\mu g/m^3$, at 4 km downwind: $2.1 \cdot 10^{-4}$ $\mu g/m^3$ and at 6 km downwind: $2.1 \cdot 10^{-4}$ $\mu g/m^3$) to the concentrations in the VPA model field (i.e. at 2 km downwind: $2.5 \cdot 10^{-4}$ $\mu g/m^3$, at 4 km downwind: $1.7 \cdot 10^{-4}$ $\mu g/m^3$ and at 6 km downwind: $1.5 \cdot 10^{-4}$ $\mu g/m^3$ or less) clearly shows the difference in the two field patterns. Similarly to what can be seen in the O_3 field (Figure 36A), the OH field modelled using the VPA model (Figure 37A) shows OH formation at the edges. SCICHEM cannot simulate such plume edge details (Figure 37B-D). Accurate simulation of the OH field is, however, essential, because of the important role of OH in atmospheric chemistry, and with respect to CCS facilities, because of the role OH plays in forming carcinogenic nitrosamines and nitramines (see section 1.1).

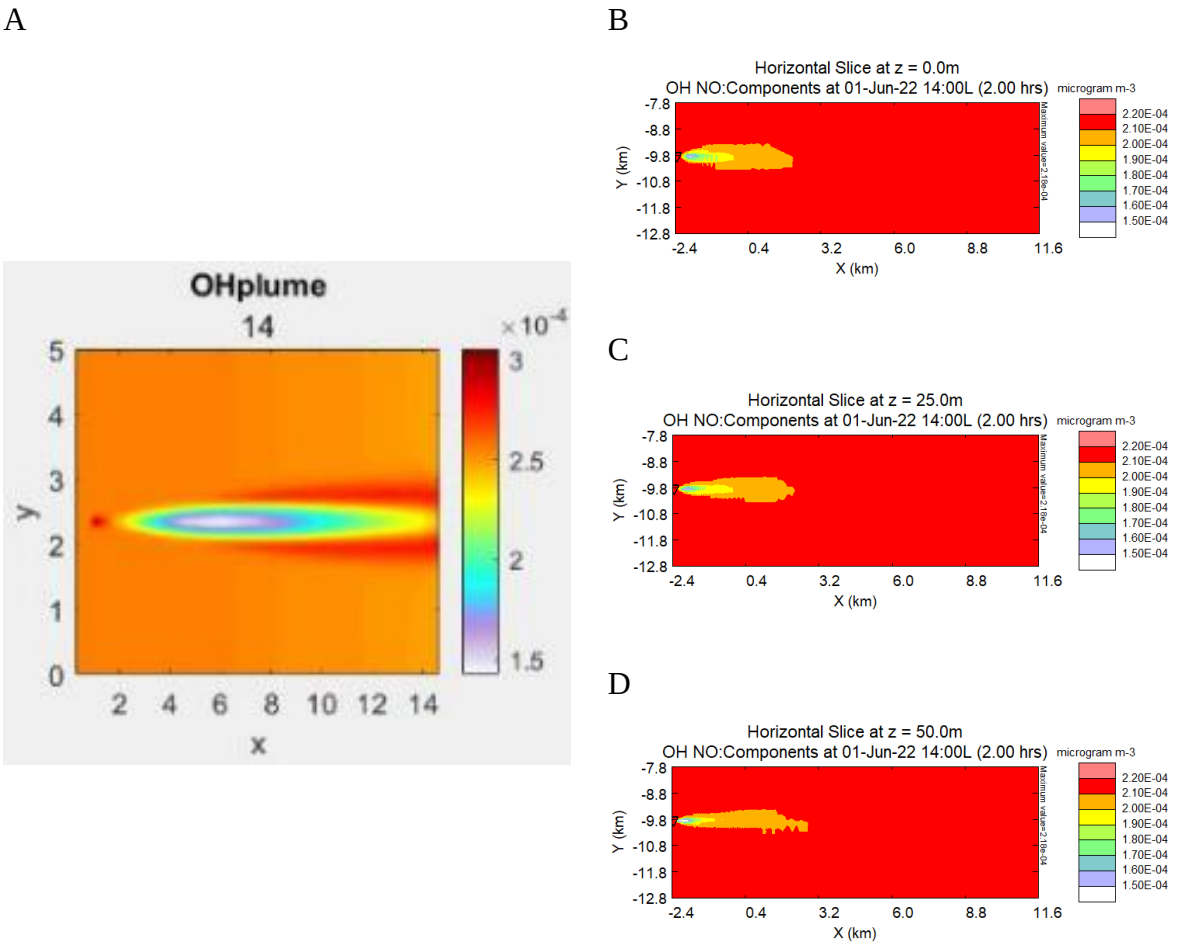

Figure 37: OH fields (in $\mu g/m^3$) at 14:00 h local time, after emission of 3.013 g/s NO at stack height of 75 m at the WtE plant. ***A****) field modelled using the Volumetric Particle Approach model. This field is a spatially averaged field over the distance from surface level to 50 m height.* ***B****) field modelled with SCICHEM and plotted with the SCICHEM GUI at surface level.* ***C****) same as B) but at 25 m height.* ***D****) same as B) but at 50 m height. For the fields shown in B-D, the multi-component input file as shown in Figure 43 in Appendix 2 was used. Note the difference in the color bars between the field modelled using the Volumetric Particle Approach model (A) and the fields modelled using SCICHEM (B-D).*

Since the same release and chemical parameters were applied in both the SCICHEM and VPA models, the main differences between the results of the two models can be attributed to the difference in the treatment of mixing and physical parameters. It seems that the VPA model starts mixing at a distance further from the source than SCICHEM. Physical parameters, such as turbulence, are much more detailed in the VPA model, whereas in the SCICHEM simulations, these were simplified and kept constant. It is important to note that the VPA model is still being developed and has not been verified using empirical data yet. It has improved turbulence and mixing modules compared to SCICHEM and as a result it creates more detailed fields. It is expected that the VPA model, when optimized and fully validated with experimental data, will improve the modelling of reactive plumes.

3.5.1 Effect of Different NO Emission

Figure 38A shows the NO_2 field in $\mu g/m^3$ that was modelled using the VPA model for the scenario where the NO emission from the power plant was increased by a factor of 10 to 30.13 g/s. This field is an average over the distance from surface level to 50 m height. It shows that the highest NO_2 concentration can be found between 4 and 8 km downwind from the source. This constitutes a shift by approximately 2 km downwind compared to the NO_2 field formed with an NO emission of 3.013 g/s (Figure 34A). This downwind shift can be explained by a higher NO emission by the source. NO_2 is formed as a result of the reaction between NO and O_3 (R8). Since more NO is emitted, and mixing does not start immediately at the source location, the NO spreads further before it reacts with O_3 forming NO_2. As explained above, three fields were plotted, because SCICHEM cannot plot an average field over a certain height. One at surface level (wind speed 4.38 m/s), one at 25 m height (wind speed 5.2 m/s) and one at 50 m height (wind speed 6.0 m/s). These fields can be seen in Figure 38B-D, respectively. The average of the highest concentrations shown in the SCICHEM fields is 14.5 $\mu g/m^3$, which is more than a factor of 2 lower than the highest concentration in the VPA field (Figure 38A), i.e. 30 $\mu g/m^3$. The SCICHEM fields (Figure 38B-D) also show that the highest concentration of NO_2 can be found close to the source, contrary to the prediction of the VPA model (Figure 38A). The SCICHEM fields (Figure 38B-D) show average NO_2 concentrations of 4.4 $\mu g/m^3$ at 2 km downwind, 2.5 $\mu g/m^3$ at 4 km downwind and 2.1 $\mu g/m^3$ at 6 km downwind. In the VPA field (Figure 38A) the NO_2 concentrations are: 10 $\mu g/m^3$ at 2 km downwind, 25 $\mu g/m^3$ at 4 km downwind and 30 $\mu g/m^3$ at 6 km downwind. The difference between the models could be explained by SCICHEM mixing the emitted species in the field and the ambient air immediately at the source location, whereas the VPA model starts mixing at a certain distance downwind from the source. This means that NO does not immediately react with O_3 forming NO_2 (R8) in the VPA model, whereas it does in SCICHEM.

A

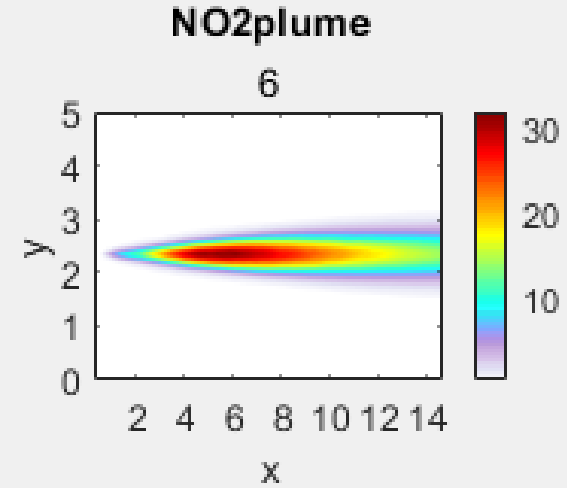

B

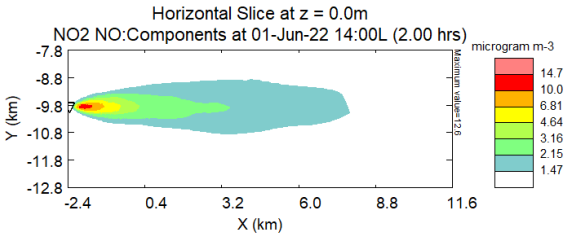

C

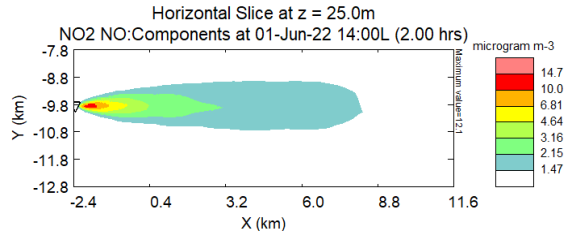

D

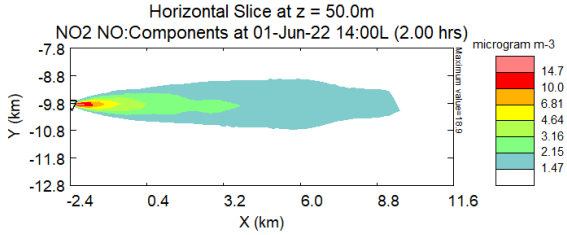

Figure 38: NO_2 fields (in µg/m^3) at 14:00 h local time, after emission of 30.13 g/s NO at stack height of 75 m at the WtE plant. ***A****) field modelled using the Volumetric Particle Approach model. This field is a spatially averaged field over the distance from surface level to 50 m height.* ***B****) field modelled with SCICHEM and plotted with the SCICHEM GUI at surface level.* ***C****) same as B) but at 25 m height.* ***D****) same as B) but at 50 m height. For the fields shown in B-D, the multi-component input file as shown in Figure 43 in Appendix 2 was used. Note the difference in the color bars between the field modelled using the Volumetric Particle Approach model (A) and the fields modelled using SCICHEM (B-D).*

Figure 39A shows the NO field modelled by Dr. Massimo Cassiani using the VPA model. It shows the highest concentration of approximately 150 $\mu g/m^3$ within the first 2 km downwind from the source. This is as expected, since NO is emitted from the source at 30.13 g/s. The highest concentration is a factor 10 higher than in case of a 3.013 g/s NO emission (Figure 35A). Similarly to the NO field shown in Figure 35A, the highest concentration in Figure 39A occurs close to the source. Since NO is rapidly oxidized to NO_2, the highest concentration was indeed expected to be near the source location (United States Environmental Protection Agency, 1999). However, by comparing the VPA field after a 3.013 g/s NO emission (Figure 35A) to the VPA field after a 30.13 g/s NO emission (Figure 39A), it can be observed that the high NO concentrations are spread over a larger distance when more NO is emitted: the emitted NO is oxidized less quickly. For this reason, the NO_2 formation by the reaction between NO and O_3 (R8) is also spread out more, causing the downwind shift of the highest NO_2 concentration in Figure 38A compared to Figure 34A. To enable comparison between the VPA and SCICHEM models, three fields at different heights (surface level, 25 m, 50 m) were made using SCICHEM (Figure 39B-D). The concentrations of these fields were subsequently averaged and compared to the VPA field. The fields in Figure 39B-D all show the highest NO concentration close to the source, similar to what the VPA model predicted (Figure 39A). The average highest concentration determined using the SCICHEM fields (Figure 39B-D) is 120.2 $\mu g/m^3$. This is comparable to what the VPA model predicted, which is a factor 1.2 lower. The SCICHEM fields (Figure 39B-D) however, dilute much quicker than the VPA field (Figure 39A). At 2 km downwind, the SCICHEM fields shown an average concentration of 21.8 $\mu g/m^3$, at 4 km downwind 5.7 $\mu g/m^3$ and at 6 km downwind the average concentration is down to 2.0 $\mu g/m^3$. Comparison to the concentrations in the VPA field (130 $\mu g/m^3$ at 2 km downwind, 50 $\mu g/m^3$ at 4 km downwind and 25 $\mu g/m^3$ at 6 km downwind), led to the observation that, especially close to the source, SCICHEM dilutes the field quicker. This is the result of the two models having different turbulence parameterizations. The SCICHEM parameterizations forecast a faster crosswind spread.

A

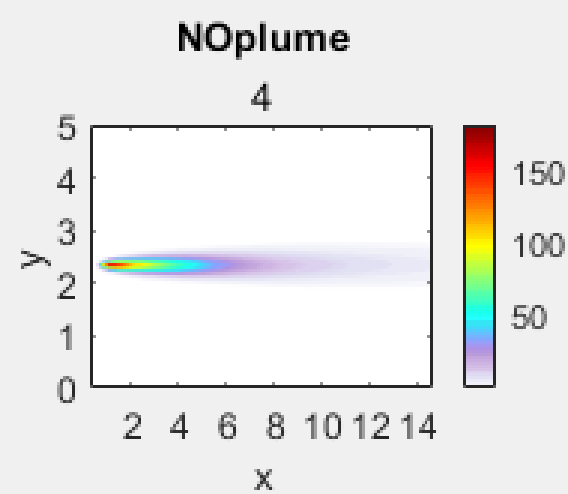

B

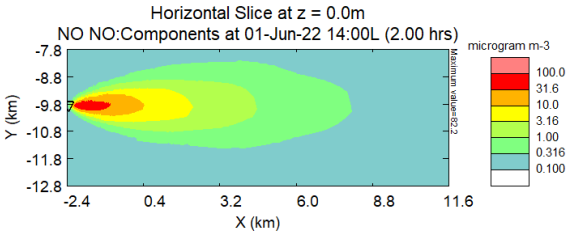

C

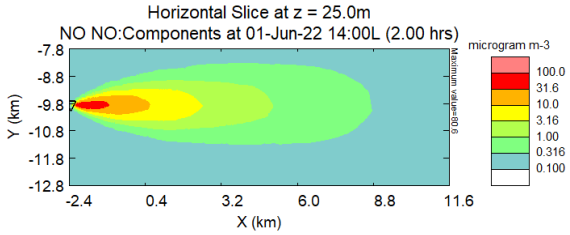

D

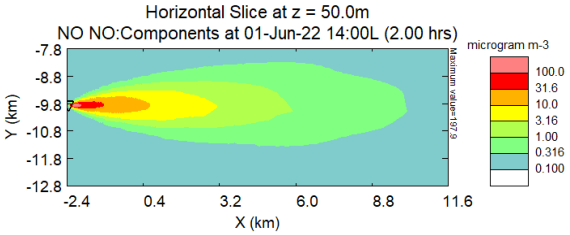

Figure 39: NO fields (in µg/m^3) at 14:00 h local time, after emission of 30.13 g/s NO at stack height of 75 m at the WtE plant. ***A****) field modelled using the Volumetric Particle Approach model. This field is a spatially averaged field over the distance from surface level to 50 m height.* ***B****) field modelled with SCICHEM and plotted with the SCICHEM GUI at surface level.* ***C****) same as B) but at 25 m height.* ***D****) same as B) but at 50 m height. For the fields shown in B-D, the multi-component input file as shown in Figure 43 in Appendix 2 was used. Note the difference in the color bars between the field modelled using the Volumetric Particle Approach model (A) and the fields modelled using SCICHEM (B-D).*

Figure 40 contains the O_3 field that was simulated by Dr. Massimo Cassiani using his VPA model with an emission of 30.13 g/s NO from the stack. Compared to the background air, it shows a gradual O_3 depletion downwind from the source until a depletion of less than 40 $\mu g/m^3$ occurs between 4 and 8 km downwind from the source. This area of depletion correlates with the area of the highest concentration in the NO_2 field (Figure 38A), because of the reaction between O_3 and NO forming NO_2 (R8). After the depletion, the O_3 concentration increases gradually back to 55 $\mu g/m^3$ at 14 km downwind. Compared to the O_3 field from the VPA model after a 3.013 g/s NO emission (Figure 36A), O_3 is depleted more strongly (40 $\mu g/m^3$ versus 60 $\mu g/m^3$), but the area of depletion has shifted approximately 2 km downwind. This can be linked to the observations for NO_2 and NO (Figure 38A and Figure 39A) and is caused by the increased NO emission. By comparing the O_3 field in Figure 40A to the average of the SCICHEM fields at surface level, 25 m height and 50 m height (Figure 40B-D), it can be observed that SCICHEM predicts the depletion immediately at the source and not several kilometers downwind from the source. The explanation for this could be that SCICHEM mixes the emitted plume and the background air immediately at the source. As expected from the reaction between NO and O_3 forming NO_2 (R8), this observation also corresponds to the SCICHEM results for NO_2 (Figure 38B-D) and NO (Figure 39B-D), i.e. the highest concentrations occur close to the source. However, the concentrations predicted by SCICHEM are higher than those predicted by the VPA model, which can again be linked to the different points in time at which the models start mixing emitted and ambient gases. Another effect of the early mixing in SCICHEM is that the SCICHEM fields are diluted much faster. Compared to the O_3 field from the VPA model (Figure 40A), the O_3 fields by SCICHEM (Figure 40B-D) are shorter. The SCICHEM fields show an average concentration of 65.9 $\mu g/m^3$ at 2 km downwind, 68.7 $\mu g/m^3$ at 4 km downwind and 69.3 at 6 km downwind. The VPA field shows concentrations of 55 $\mu g/m^3$ at 2 km downwind, 45 $\mu g/m^3$ at 4 km downwind and less than 40 $\mu g/m^3$ at 6 km downwind. This indicates that the O_3 field from the VPA model predicts the area of depletion at 6 km downwind, whereas the O_3 fields from SCICHEM predict a concentration almost equal to the background concentration of 69.6 $\mu g/m^3$.

A

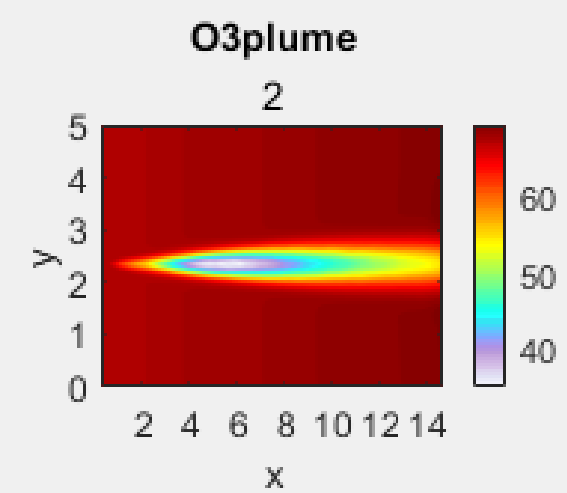

B

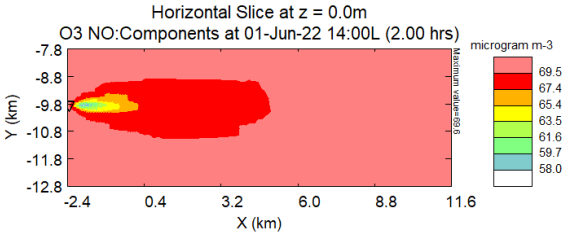

C

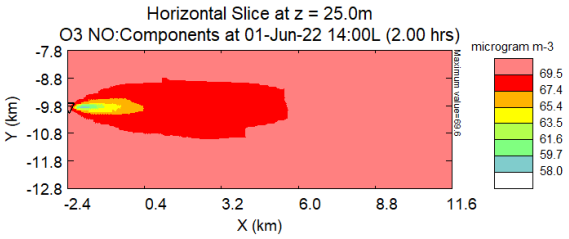

D

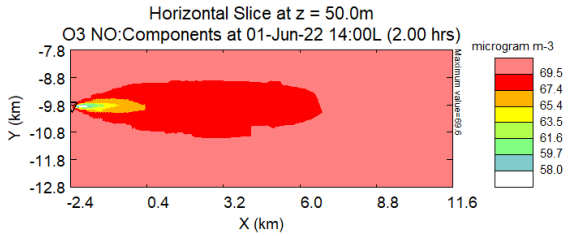

Figure 40: O_3 fields (in µg/m^3) at 14:00 h local time, after emission of 30.13 g/s NO at stack height of 75 m at the WtE plant. ***A****) field modelled using the Volumetric Particle Approach model. This field is a spatially averaged field over the distance from surface level to 50 m height.* ***B****) field modelled with SCICHEM and plotted with the SCICHEM GUI at surface level.* ***C****) same as B) but at 25 m height.* ***D****) same as B) but at 50 m height. For the fields shown in B-D, the multi-component input file as shown in Figure 43 in Appendix 2 was used. Note the difference in the color bars between the field modelled using the Volumetric Particle Approach model (A) and the fields modelled using SCICHEM (B-D).*

Figure 41A contains the OH field from the VPA model. It shows an increase of OH relative to the background at around 2 km downwind from the source, before a depletion of OH occurs from 6 km downwind onwards. As outlined above, the area of increased OH close to the source in the VPA model needs further investigation. From 10 km onwards, a clear formation of OH can be observed at the edges of the field. The highest OH concentration is modelled to be $4 \cdot 10^{-4}$ $\mu g/m^3$ and the area of depletion has concentrations below $1 \cdot 10^{-4}$ $\mu g/m^3$. Compared to the OH field after an NO emission of 3.013 g/s (Figure 37A), a larger area of depletion can be seen in the 30.13 g/s NO emission scenario (Figure 41A). Furthermore, the area of formation is larger with higher concentrations and there is a shift downwind. Comparison of the OH field modelled by the VPA model (Figure 41A) and the average of the OH fields at surface level, 25 m height and 50 m height modelled using SCICHEM (Figure 41B-D) resulted in the observation that SCICHEM does not predict any OH increase relative to the background, neither close to the source nor further downwind. Instead, SCICHEM predicts the OH depletion to occur close to the source, with the lowest concentration area spanning only a few hundred meters. The VPA model, on the other hand, predicts OH depletion at several kilometers as shown in Figure 41A. The position and size of the area of depletion in the SCICHEM fields (Figure 41B-D) could be explained by SCICHEM mixing the emitted plume with the background air immediately at the source. NO then reacts immediately with O_3 forming NO_2 (R8), thus stopping the formation of OH close to the source (R5 and R7). This is reflected in the NO_2 (Figure 38B-D), NO (Figure 39B-D) and O_3 (Figure 40B-D) fields. This also results in NO being more strongly diluted closer to the source, allowing OH to be formed from the remaining O_3 (R5 and R7) and making the area of OH depletion shorter than predicted by the VPA model. Comparing the concentrations at several distances downwind reveals the difference in the OH fields modelled by the SCICHEM and VPA models. SCICHEM (Figure 41B-D) predicts an average concentration of $8.8 \cdot 10^{-5}$ $\mu g/m^3$ at 2 km downwind, $1.6 \cdot 10^{-4}$ $\mu g/m^3$ at 4 km downwind and $1.8 \cdot 10^{-4}$ $\mu g/m^3$ at 6 km downwind. The VPA model (Figure 41A), on the other hand, predicts a concentration of $4 \cdot 10^{-4}$ $\mu g/m^3$ at 2 km downwind, $2.5 \cdot 10^{-4}$ $\mu g/m^3$ at 4 km downwind and $1.5 \cdot 10^{-4}$ $\mu g/m^3$ at 6 km downwind. So, whereas SCICHEM predicts an increase from 2 to 6 km downwind from the source, the VPA model predicts a decrease. Once again, clear OH formation can be observed at the edges of the field simulated by the VPA model (Figure 41A), highlighting the suitability of the VPA model, once fully validated, for near-source combustion plume simulations.

A

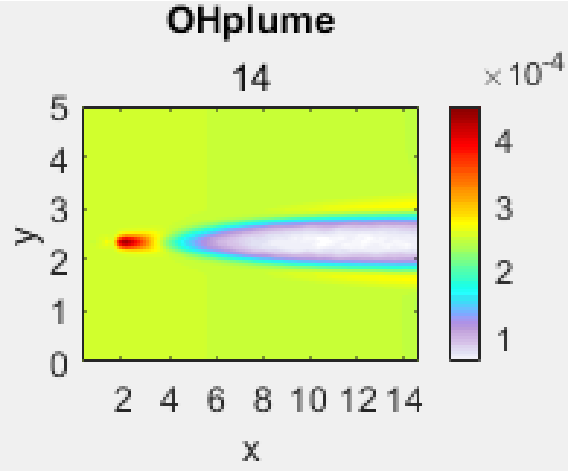

B

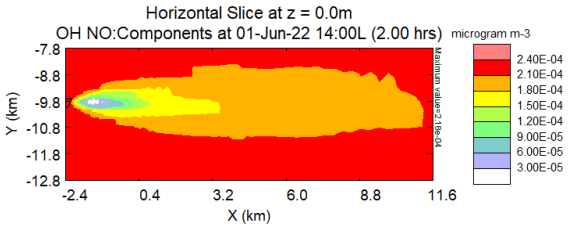

C

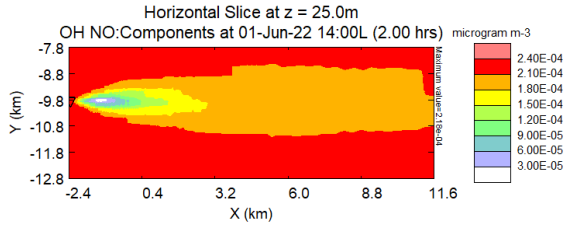

D

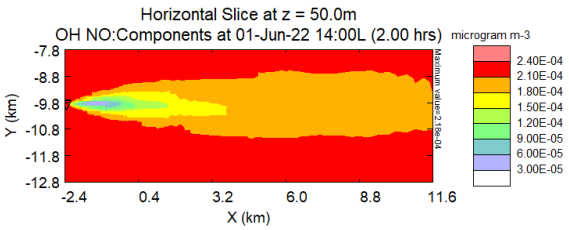

Figure 41: OH fields (in µg/m^3) at 14:00 h local time, after emission of 30.13 g/s NO at stack height of 75 m at the WtE plant. ***A****) field modelled using the Volumetric Particle Approach model. This field is a spatially averaged field over the distance from surface level to 50 m height.* ***B****) field modelled with SCICHEM and plotted with the SCICHEM GUI at surface level.* ***C****) same as B) but at 25 m height.* ***D****) same as B) but at 50 m height. For the fields shown in B-D, the multi-component input file as shown in Figure 43 in Appendix 2 was used. Note the difference in the color bars between the field modelled using the Volumetric Particle Approach model (A) and the fields modelled using SCICHEM (B-D).*

To summarize, increasing the NO emission results in a larger area of OH depletion in the SCICHEM fields and in the VPA field. However, the area of depletion is much larger in the VPA field. Moreover, the area of depletion has shifted several kilometers downwind in the VPA field due to the increased NO emission, whereas SCICHEM keeps the area of depletion close to the source. This could be explained by SCICHEM mixing emitted and ambient gases more thoroughly and earlier than the VPA model. Since the VPA model has not been verified against actual measurements, field measurements are required to verify which of the two models simulates reality more accurately.

4 Conclusion

To understand the NO_x, O_3 and OH chemistry in combustion plumes, four case studies were performed.

In case study 1 the power plant plume simulation as presented by Zheng et al. (2020) was repeated. Zheng et al. (2020) employed the Fluidity-Chem model, which is verified against measurement data. Since there was adequate agreement between the results from Zheng et al. (2020) and the results of the SCICHEM simulation, it can be concluded that SCICHEM is a good reactive plume model, achieving reliable results. However, this case study clearly shows that, contrary to the Fluidity-Chem model, the SCICHEM GUI cannot capture the fine details at the edges of the plume. This emphasizes the need for the VPA model, which is able to simulate these details.

In case study 2, the simulation of an isolated ship plume as presented by Charlton-Perez et al. (2009) was performed and the scenario was used to test the influence of the model set up on the results. This case was used to determine:

1. The influence of the applied atmospheric chemistry scheme.
2. The influence of the atmospheric chemical background.
3. The influence of NO emission strength.

The main conclusions from case study 2 are:

- Both the applied chemistry scheme and the atmospheric chemical background play an important role in achieving reliable modelling results. Using a very clean background or a simplified atmospheric chemistry scheme may lead to inaccurate results.
- Ambient levels of peroxy radicals, e.g. $CH_3C(O)O_2$ and HO_2, determine whether OH formation or OH depletion occurs close to the source.
- Different treatment of HNO_3 in the used atmospheric chemical schemes is responsible for differences in the simulated OH fields.

- Reducing the NO emission by a factor of 10 results in shorter areas of depletion in the OH field, as well as a lesser reduction of the OH VMR.

Simulating NO, NO_2, O_3 and OH fields within the WtE plant plume (as described in case study 3a) resulted in the following observations:

- The highest VMRs of NO and NO_2 were found close to the source.
- Both O_3 and OH were depleted close to the source.
    - At 80.5 m height, there was a total OH depletion. At surface level, only a 46% depletion relative to the ambient OH level occurred.
- At 2.2 km downwind from the source, OH formation was observed, both at surface level and at a height of 80.5 m.

The observations about the OH field show that the conceptual picture that NO depletes O_3 and therefore indirectly also depletes OH near the source is not valid. Under low NO emission conditions (i.e. 3.02 g/s) as at the WtE plant, the OH chemistry starts close to the source. The OH field near the source can be explained by the following observations:

- OH formation was found to be the result of ambient HO_2 reacting with the emitted NO: $HO_2 + NO \rightarrow OH + NO_2$.
- OH depletion near the source was found to be the combined result of:
    - Ozone titration: $O_3 + NO \rightarrow O_2 + NO_2$
    - HNO_3 formation: $OH + NO_2 + M \rightarrow HNO_3 + M$
    - HONO formation: $OH + NO + M \rightarrow HONO + M$
- Increasing the NO emission by a factor of 10 to 30.2 g/s resulted in increased ozone titration and HONO formation, and subsequently in more OH depletion. Therefore, it pushed the OH formation further downwind from the source.
- Emission of different nitrogen-containing species, such as NO_2 and HONO, was found to be important for the OH field as well.

- NO_2 emission resulted in less OH depletion close to the source and less OH formation further downwind. Near the source, NO_2 reacted or photolyzed forming NO, which in turn can react with HO_2 forming OH. Further downwind, NO_2 reacted with OH forming HNO_3, thereby acting as an OH sink.

- Emitted HONO acted as a source of OH, resulting in an increase of the OH VMR further downwind. However, when 30.2 g/s NO was emitted, the formed OH immediately reacted with the emitted NO forming HONO again.

- After emission of CH_3CHO in addition to NO, the OH formation no longer used the background HO_2. Instead, CH_3CHO became the main source of HO_2.

  - This also reduced the importance of turbulence in the model, since the emitted species were already pre-mixed in the emission plume.

  - CH_3CHO acted as an OH sink further downwind, reducing the OH formation downwind.

The above-mentioned observations highlight the importance of having accurate emission levels for the relevant species and of using a reliable atmospheric chemistry scheme. In order to accurately simulate OH fields within combustion plumes, the chemistry scheme should therefore at least include:

- Ozone titration
- HONO formation
- HNO_3 formation
- The reaction between HO_2 and NO forming OH and NO_2.

In case study 3b, the amine PZ was added to the emission scenario for the WtE plant. This resulted in the highest PZNO and $PZNO_2$ concentrations close to the source:

- Concentrations of 0.97 ng/m^3 PZNO and 0.72 ng/m^3 $PZNO_2$ were found at approximately 1.5 km downwind from the source at surface level.

    - Both concentrations exceed the guideline value of 0.3 ng/m^3 set by the Norwegian Institute of Public Health.

- An additional direct emission of 1 ppb of PZNO led to PZNO build-up near the source, up to levels of 1.54 ng/m^3.

- It was found that increasing the NO emission by a factor of 10 resulted in lower maximum PZNO and $PZNO_2$ VMRs, which were found further downwind from the source.

    - The increased NO emission resulted in more OH depletion and therefore limited the formation of PZNR, which is the precursor for PZNO and $PZNO_2$.

Comparison of the fields at the WtE plant from the SCICHEM and VPA models suggests that the main difference between the two models lies in the mixing modules. SCICHEM appears to start mixing closer to the source than the VPA model, thus leading to different results near the source. However, the VPA model is still being developed and has not yet been verified against measurements. For that reason, aircraft measurements should be performed to determine whether the SCICHEM or the VPA model is more accurate. Once the VPA model has been improved, it will most likely be a superior model to simulate near source emissions, since it includes better turbulence and mixing modules and can simulate plumes in more detail, especially towards the plume edge.

However, it is important to remark that some simplifications were made in the simulations:

- In all simulations, default landscape and meteorology parameters were used that were kept constant throughout the run.

    - Further simulations should be performed with accurate parameters, which change over time if applicable, in order to determine the effect of landscape and meteorology emission plumes.

- A constant background level was used for all species involved in the WtE plant simulations (case study 3a and 3b), but in reality, these levels change during the course of a day and they can affect the emission plume concentrations.

- Therefore, future work should also focus on obtaining accurate background levels that vary diurnally for the area of interest.

Due to the simplifications mentioned, the PZNO and $PZNO_2$ concentrations will likely be lower in reality. However, the calculated PZNO and $PZNO_2$ concentrations approach the limit set by the Norwegian Institute of Public Health. This highlights the need for careful assessment of the surrounding area before building future CCS facilities.

References

Abdul-Wahab, S., Sappurd, A., & Al-Damkhi, A. (2011). Application of California Puff (CALPUFF) Model: a Case Study for Oman. *Clean Technologies and Environmental Policy*, *13*(1), 177-189. https://doi.org/10.1007/s10098-010-0283-7

Albrecht, S. R., Novelli, A., Hofzumahaus, A., Kang, S., Baker, Y., Mentel, T., Wahner, A., & Fuchs, H. (2019). Measurements of Hydroperoxy Radicals (HO_2) at Atmospheric Concentrations Using Bromide Chemical Ionisation Mass Spectrometry. *Atmospheric Measurement Techniques*, *12*(2), 891-902. https://doi.org/10.5194/amt-12-891-2019

Alicke, B., Geyer, A., Hofzumahaus, A., Holland, F., Konrad, S., Pätz, H. W., Schäfer, J., Stutz, J., Volz-Thomas, A., & Platt, U. (2003). OH Formation by HONO Photolysis During the BERLIOZ Experiment. *Journal of Geophysical Research: Atmospheres*, *108*(D4), PHO 3-1-PHO 3-17. https://doi.org/10.1029/2001JD000579

Benkovitz, C. M., Scholtz, M. T., Pacyna, J., Tarrasón, L., Dignon, J., Voldner, E. C., Spiro, P. A., Logan, J. A., & Graedel, T. E. (1996). Global Gridded Inventories of Anthropogenic Emissions of Sulfur and Nitrogen. *Journal of Geophysical Research-Atmospheres*, *101*(D22), 29239-29253. https://doi.org/10.1029/96JD00126

Brasseur, G. P., & Jacob, D. J. (2017). *Modeling of Atmospheric Chemistry*. Cambridge University Press. https://doi.org/10.1017/9781316544754

Breeze Technologies. (2021). *Air Pollution - How to Convert between mg/m^3, µg/m^3 and ppm, ppb*. Retrieved 23-03-2023 from https://www.breeze-technologies.de/blog/air-pollution-how-to-convert-between-mgm3-µgm3-ppm-ppb/

Brock, C. A., Washenfelder, R. A., Trainer, M., Ryerson, T. B., Wilson, J. C., Reeves, J. M., Huey, L. G., Holloway, J. S., Parrish, D. D., Hübler, G., & Fehsenfeld, F. C. (2002). Particle Growth in the Plumes of Coal-Fired Power Plants. *Journal of Geophysical Research-Atmospheres*, *107*(D12), 1-14, Article 4155. https://doi.org/10.1029/2001jd001062

Brown, R. J., & Bilger, R. W. (1998). Experiments on a Reacting Plume - 1. Conventional Concentration Statistics [Article]. *Atmospheric Environment*, *32*(4), 611-628. https://doi.org/10.1016/s1352-2310(97)00294-x

Brune, W. H., Baier, B. C., Thomas, J., Ren, X., Cohen, R. C., Pusede, S. E., Browne, E. C., Goldstein, A. H., Gentner, D. R., Keutsch, F. N., Thornton, J. A., Harrold, S., Lopez-Hilfiker, F. D., & Wennberg, P. O. (2016). Ozone Production Chemistry in the Presence of Urban Plumes. *Faraday Discussions*, *189*(0), 169-189. https://doi.org/10.1039/C5FD00204D

Canpolat, B. R., Atimtay, A. T., Munlafalioglu, I., Kalafatoglu, E., & Ekinci, E. (2002). Emission Factors of Cement Industry in Turkey. *Water, Air and Soil Pollution*, *138*(1-4), 235-252. https://doi.org/10.1023/a:1015502131180

Cassiani, M. (2013). The Volumetric Particle Approach for Concentration Fluctuations and Chemical Reactions in Lagrangian Particle and Particle-grid Models. *Boundary-Layer Meteorology*, *146*(2), 207-233. https://doi.org/10.1007/s10546-012-9752-3

Cassiani, M., Bertagni, M. B., Marro, M., & Salizzoni, P. (2020). Concentration Fluctuations from Localized Atmospheric Releases. *Boundary-Layer Meteorology*, *177*(2-3), 461-510. https://doi.org/10.1007/s10546-020-00547-4

Cassiani, M., Franzese, P., & Giostra, U. (2005). A PDF Micromixing Model of Dispersion for Atmospheric Flow. Part 1: Development of the Model, Application to Homogeneous Turbulence and to Neutral Boundary Layer. *Atmospheric Environment*, *39*(8), 1457-1469. https://doi.org/10.1016/j.atmosenv.2004.11.020

Cassiani, M., Stohl, A., & Eckhardt, S. (2013). The Dispersion Characteristics of Air Pollution from the World's Megacities. *Atmospheric Chemistry and Physics*, *13*(19), 9975-9996. https://doi.org/10.5194/acp-13-9975-2013

CCS Norway. (2022). *The Longship CCS Project*. Retrieved 04-05-2023 from https://ccsnorway.com/full-scale-capture-transport-and-storage

Chandan, P. A., Remias, J. E., Neathery, J. K., & Liu, K. (2013). Morpholine Nitrosation To Better Understand Potential Solvent Based CO_2 Capture Process Reactions [Article]. *Environmental Science & Technology*, *47*(10), 5481-5487. https://doi.org/10.1021/es4003108

Charlton-Perez, C. L., Evans, M. J., Marsham, J. H., & Esler, J. G. (2009). The Impact of Resolution on Ship Plume Simulations with NO_x Chemistry. *Atmospheric Chemistry and Physics*, *9*(19), 7505-7518. https://doi.org/10.5194/acp-9-7505-2009

Chen, Q., Hu, X., & Xie, D. (2022). Collaborative control of branching ratio in the $O + HO_2 \rightarrow OH + O_2$ reaction via vibrational and rotational excitation. *Journal of the Chinese Chemical Society*, *70*(3), 521-527. https://doi.org/10.1002/jccs.202200404

Cheng, L., Peake, E., Rogers, D., & Davis, A. (1986). Oxidation of Nitric-Oxide Controlled by Turbulent Mixing in Plumes from Oil Sands Extraction Plants [Article]. *Atmospheric Environment*, *20*(9), 1697-1703. https://doi.org/10.1016/0004-6981(86)90117-4

Chowdhury, B., Karamchandani, P. K., Sykes, R. I., Henn, D. S., & Knipping, E. (2015). Reactive Puff Model SCICHEM: Model Enhancements and Performance Studies. *Atmospheric Environment*, *117*, 242-258. https://doi.org/10.1016/j.atmosenv.2015.07.012

Chu, H., & Wang, M. (2014). The Definition of Point Sources: Point Charge, Mass Point and Heat Point Source—A Generalized Sternberg Definition of Concentrated Forces. *Journal of Applied Mechanics*, *81*(1). https://doi.org/10.1115/1.4024075

Cohen, E. R., & Taylor, B. N. (1987). The 1986 Adjustment of the Fundamental Physical Constants. *Reviews of modern physics*, *59*(4), 1121-1148. https://doi.org/10.1103/RevModPhys.59.1121

Davis, D. D. (1977). *OH Radical Measurements: Impact on Power Plant Plume Chemistry. Final Report.* osti.gov/servlets/purl/5196152

Day, M., & Chenoweth, S. (2013). 6.14 Surface Roughness of Karst Landscapes. In J. F. Shroder (Ed.), *Treatise on Geomorphology* (Vol. 6, pp. 157-163). Academic Press. https://doi.org/10.1016/B978-0-12-374739-6.00108-1

De Koeijer, G., Talstad, V. R., Nepstad, S., Tønnessen, D., Falk-Pedersen, O., Maree, Y., & Nielsen, C. (2013). Health Risk Analysis for Emissions to Air from CO_2 Technology Centre Mongstad [Article]. *International Journal of Greenhouse Gas Control*, *18*, 200-207. https://doi.org/10.1016/j.ijggc.2013.07.010

Dignon, J. (1992). NO_x and SO_x Emissions from Fossil Fuels: A Global Distribution. *Atmospheric Environment Part a-General Topics*, *26*(6), 1157-1163. https://doi.org/10.1016/0960-1686(92)90047-O

EPRI. (2021). *SCICHEM (Version 3.3)*. In [Computer Program]. https://github.com/epri-dev/SCICHEM/releases

European Chemicals Bureau. (2005). *European Union Risk Assessment Report: Piperazine*. https://echa.europa.eu/documents/10162/35f9602c-cb84-448f-9383-250e1a5ad350

European Commission. (2012). *Final Report Summary - CESAR (CO_2) Enhanced Separation and Recovery*. Retrieved 08-05-2023 from https://cordis.europa.eu/project/id/213569/reporting

European Commission. (2019). *Climate and Air Impacts - EMEP*. Retrieved 29-03-2023 from https://ec.europa.eu/environment/archives/air/models/emep.htm

European Monitoring and Evaluation Programme. (2021). *EMEP*. Retrieved 29-03-2023 from https://www.emep.int

Farmer, K. (2018). *Evaluation of Concentrated Piperazine for CO_2 Capture from Coal-Fired Flue Gas - NCCC Report*. https://www.nationalcarboncapturecenter.com/wp-content/uploads/2021/01/AECOM-and-University-of-Texas-at-Austin-Evaluation-of-Concentrated-Piperazine-for-CO2-Capture-from-Coal-Fired-Flue-Gas-2019.pdf

Federal Aviation Administration. (2008). *Wind Shear*. https://www.faasafety.gov/files/gslac/library/documents/2011/aug/56407/faa%20p-8740-40%20windshear%5Bhi-res%5D%20branded.pdf

Freeman, S. A., Dugas, R., Van Wagener, D. H., Nguyen, T., & Rochelle, G. T. (2010). Carbon Dioxide Capture with Concentrated, Aqueous Piperazine. *International Journal of Greenhouse Gas Control*, *4*(2), 119-124. https://doi.org/10.1016/j.ijggc.2009.10.008

Gaspar, J., Von Solms, N., Thomsen, K., & Fosbøl, P. L. (2016). Multivariable Optimization of the Piperazine CO_2 Post-Combustion Process. *Energy Procedia*, *86*, 229-238. https://doi.org/10.1016/j.egypro.2016.01.024

Georgopoulos, P. G., & Seinfeld, J. H. (1986). Mathematical Modeling of Turbulent Reacting Plumes - 1. General Theory and Model Formulation. *Atmospheric Environment*, *20*(9), 1791-1807. https://doi.org/10.1016/0004-6981(86)90128-9

Gibbins, J., & Chalmers, H. (2008). Carbon Capture and Storage. *Energy Policy*, *36*(12), 4317-4322. https://doi.org/10.1016/j.enpol.2008.09.058

Gillani, N. V., Meagher, J. F., Valente, R. J., Imhoff, R. E., Tanner, R. L., & Luria, M. (1998). Relative Production of Ozone and Nitrates in Urban and Rural Power Plant Plumes: 1. Composite Results Based on Data from 10 Field Measurement Days. *Journal of Geophysical Research: Atmospheres*, *103*(D17), 22593-22615. https://doi.org/10.1029/98JD00966

Goldman, M. J., Fine, N. A., & Rochelle, G. T. (2013). Kinetics of N-Nitrosopiperazine Formation from Nitrite and Piperazine in CO_2 Capture [Article]. *Environmental Science & Technology*, *47*(7), 3528-3534. https://doi.org/10.1021/es304640f

Guziana, B., Song, H., Thorin, E., Dotzauer, E., & Yan, J. (2014). Policy Based Scenarios for Waste-to-Energy Use: Swedish Perspective. *Waste and Biomass Valorization*, *5*(4), 679-688. https://doi.org/10.1007/s12649-013-9262-7

Haikola, S., Hansson, A., & Anshelm, J. (2019). From Polarization to Reluctant Acceptance–Bioenergy with Carbon Capture and Storage (BECCS) and the Post-Normalization of the Climate Debate. *Journal of Integrative Environmental Sciences*, *16*(1), 45-69. https://doi.org/10.1080/1943815X.2019.1579740

Hamer, P. D., Walker, S.-E., Sousa-Santos, G., Vogt, M., Vo-Thanh, D., Lopez-Aparicio, S., Schneider, P., Ramacher, M. O. P., & Karl, M. (2020). The Urban Dispersion Model EPISODE v10.0 - Part 1: An Eulerian and Sub-Grid-Scale Air Quality Model and its Application in Nordic Winter Conditions. *Geoscientific Model Development*, *13*(9), 4323-4353. https://doi.org/10.5194/gmd-13-4323-2020

Hennig, F., Sugiri, D., Tzivian, L., Fuks, K., Moebus, S., Jöckel, K. H., Vienneau, D., Kuhlbusch, T. A. J., De Hoogh, K., Memmesheimer, M., Jakobs, H., Quass, U., & Hoffmann, B. (2016). Comparison of Land-Use Regression Modeling with Dispersion and Chemistry Transport Modeling to Assign Air Pollution Concentrations within the Ruhr Area. *Atmosphere*, *7*(3), 48. https://doi.org/10.3390/atmos7030048

Hewitt, C. N. (2001). The Atmospheric Chemistry of Sulphur and Nitrogen in Power Station Plumes. *Atmospheric Environment*, *35*(7), 1155-1170. https://doi.org/10.1016/s1352-2310(00)00463-5

IPCC. (2014). *Climate Change 2014: Synthesis Report. Contribution of Working Groups I, II and III to the Fifth Assessment Report of the Intergovernmental Panel on Climate Change [Core Writing Team, R.K. Pachauri and L.A. Meyer (eds.)]. IPCC, Geneva, Switzerland, 151 pp*.

Janssen, L. H. J. M., Van Haren, F., Bange, P., & Van Duuren, H. (1991). Measurements and Modelling of Reactions of Nitrogen Oxides in Power-Plant Plumes at Night [Article]. *Atmospheric Environment Part a-General Topics*, *25*(5-6), 829-840. https://doi.org/10.1016/0960-1686(91)90126-r

Joos, E., Mendonca, A., & Seigneur, C. (1967). Evaluation of a Reactive Plume Model with Power Plant Plume Data-Application to the Sensitivity Analysis of Sulfate and Nitrate Formation. *Atmospheric Environment (1967)*, *21*(6), 1331-1343. https://doi.org/10.1016/0004-6981(67)90080-7

Kamal, A., Ali, U., Ramay, M. I., Younis, S. M. Z., Sumbal, S., Malik, R. N., & Rashid, A. (2017). Principle Component Analysis of Flue Gas Exhaust and Health Risk Estimates for the Population around a Functional Incinerator in the Vicinity of Rawalpindi Pakistan. *Arabian Journal of Chemistry*, *10*, S2302-S2306. https://doi.org/10.1016/j.arabjc.2013.08.006

Karamchandani, P., Morris, R., Yarwood, G., Brashers, B., Henn, D., Sykes, I., Knipping, E., & Kumar, N. (2018). SCICHEM: An Alternative Photochemical Model to Calculate Single Source Impacts on Ozone and Fine Particulate Matter. *EM Magazine*. https://www.awma.org/emoct18

Karamchandani, P., Santos, L., Sykes, I., Zhang, Y., Tonne, C., & Seigneur, C. (2000). Development and Evaluation of a State-of-the-Science Reactive Plume Model. *Environmental Science & Technology*, *34*(5), 870-880. https://doi.org/10.1021/es990611v

Karamchandani, P., Seigneur, C., Vijayaraghavan, K., & Wu, S.-Y. (2002). Development and Application of a State-of-the-Science Plume-in-Grid Model. *Journal of Geophysical Research: Atmospheres*, *107*(D19), ACH 12-11-ACH 12-13. https://doi.org/10.1029/2002JD002123

Karamchandani, P., Vennam, P., Shah, T., Henn, D., Alvarez-Gomez, A., Yarwood, G., Morris, R., Brashers, B., Knipping, E., & Kumar, N. (2020). Single Source Impacts on Secondary Pollutants using a Lagrangian Reactive Puff Model: Comparison with Photochemical Grid Models. *Atmospheric Environment*, *237*, 117664. https://doi.org/10.1016/j.atmosenv.2020.117664

Karamchandani, P., Vijayaraghavan, K., & Yarwood, G. (2011). Sub-Grid Scale Plume Modeling. *Atmosphere*, *2*(3), 389-406. https://doi.org/10.3390/atmos2030389

Khan, M. A. H., Cooke, M. C., Utembe, S. R., Archibald, A. T., Derwent, R. G., Jenkin, M. E., Morris, W. C., South, N., Hansen, J. C., Francisco, J. S., Percival, C. J., & Shallcross, D. E. (2015). Global Analysis of Peroxy Radicals and Peroxy Radical-Water Complexation using the STOCHEM-CRI Global Chemistry and Transport Model. *Atmospheric Environment*, *106*, 278-287. https://doi.org/10.1016/j.atmosenv.2015.02.020

Kim, H. S., Kim, Y. H., Han, K. M., Kim, J., & Song, C. H. (2016). Ozone Production Efficiency of a Ship-Plume: ITCT 2K2 Case Study. *Chemosphere*, *143*, 17-23. https://doi.org/10.1016/j.chemosphere.2015.05.022

Kim, Y. H., Kim, H. S., & Song, C. H. (2017). Development of a Reactive Plume Model for the Consideration of Power-Plant Plume Photochemistry and its Applications. *Environmental Science & Technology*, *51*(3), 1477-1487. https://doi.org/10.1021/acs.est.6b03919

Knipping, E. (2021a). *SCICHEM Version 3.3 Technical Documentation 3002022845*.

Knipping, E. (2021b). *SCICHEM VERSION 3.3 User's Guide 3002022845*.
Languille, B., Drageset, A., Mikoviny, T., Zardin, E., Benquet, C., Ullestad, Ø., Aronson, M., Romslo Kleppe, E., & Wisthaler, A. (2021, 15th - 18th March). *Atmospheric Emissions of Amino-Methyl-Propanol, Piperazine and their Degradation Products during the 2019-20 ALIGN-CCUS Campaign at the Technology Centre Mongstad.* 15th International Conference on Greenhouse Gas Control Technologies, GHGT-15, Abu Dhabi, UAE. https://papers.ssrn.com/sol3/papers.cfm?abstract_id=3812139
Lee, J., Lee, S., Son, H., & Yi, W. H. (2021). Development of PUFF–Gaussian Dispersion Model for the Prediction of Atmospheric Distribution of Particle Concentration. *Scientific Reports*, *11*(1), 6456. https://doi.org/10.1038/s41598-021-86039-y
Lu, Y., & Khalil, M. A. K. (1992). Model Calculations of Night-Time Atmospheric OH. *Tellus B: Chemical and Physical Meteorology*, *44*(2), 106-113. https://doi.org/10.1034/j.1600-0889.1992.t01-1-00003.x
Luria, M., Valente, R. J., Tanner, R. L., Gillani, N. V., Imhoff, R. E., Mueller, S. F., Olszyna, K. J., & Meagher, J. F. (1999). The Evolution of Photochemical Smog in a Power Plant Plume. *Atmospheric Environment*, *33*(18), 3023-3036. https://doi.org/10.1016/S1352-2310(99)00072-2
Manzoor, S., Karl, M., Simperler, A., & Korre, A. (2017). Model Study on the Influence of Plant Design, Photochemistry and Meteorology on Atmospheric Concentrations of Nitrosamines and Nitramines in Vicinity of an Amine-Based CO_2 Capture Facility. *International Journal of Greenhouse Gas Control*, *65*, 203-217. https://doi.org/10.1016/j.ijggc.2017.07.013
Manzoor, S., Korre, A., Durucan, S., & Simperler, A. (2014). Atmospheric Chemistry Modelling of Amine Emissions from Post Combustion CO_2 Capture Technology. *Energy Procedia*, *63*, 822-829. https://doi.org/https://doi.org/10.1016/j.egypro.2014.11.093
Martinez, M., Harder, H., Kovacs, T. A., Simpas, J. B., Bassis, J., Lesher, R., Brune, W. H., Frost, G. J., Williams, E. J., Stroud, C. A., Jobson, B. T., Roberts, J. M., Hall, S. R., Shetter, R. E., Wert, B., Fried, A., Alicke, B., Stutz, J., Young, V. L., . . . Zamora, R. J. (2003). OH and HO_2 Concentrations, Sources, and Loss Rates During the Southern Oxidants Study in Nashville, Tennessee, Summer 1999. *Journal of Geophysical Research: Atmospheres*, *108*(D19). https://doi.org/10.1029/2003JD003551
Mazari, S. A., Alaba, P., & Saeed, I. M. (2019). Formation and Elimination of Nitrosamines and Nitramines in Freshwaters Involved in Post-Combustion Carbon Capture Process. *Journal of Environmental Chemical Engineering*, *7*(3), Article 103111. https://doi.org/10.1016/j.jece.2019.103111
McDonald, J. D., Kracko, D., Doyle-Eisele, M., Garner, C. E., Wegerski, C., Senft, A., Knipping, E., Shaw, S., & Rohr, A. (2014). Carbon Capture and Sequestration: An Exploratory Inhalation Toxicity Assessment of Amine-Trapping Solvents and their Degradation Products. *Environmental Science & Technology 48*(18), 10821-10828. https://doi.org/10.1021/es5009505
Mitch, W. (2019). *Literature Review of Nitrosamine and Nitramine Formation Chemistry Relevant to Carbon Capture*. ccsnorway.com/app/uploads/sites/6/2019/10/nitrosamineandnitramineformationchemistry_yale-1.pdf
Müller, M., Anderson, B. E., Beyersdorf, A. J., Crawford, J. H., Diskin, G. S., Eichler, P., Fried, A., Keutsch, F. N., Mikoviny, T., Thornhill, K. L., Walega, J. G., Weinheimer, A. J., Yang, M., Yokelson, R. J., & Wisthaler, A. (2016). In Situ Measurements and Modeling of Reactive Trace Gases in a Small Biomass Burning Plume. *Atmospheric Chemistry and Physics*, *16*(6), 3813-3824. https://doi.org/10.5194/acp-16-3813-2016

Nanni, A., Tinarelli, G., Solisio, C., & Pozzi, C. (2022). Comparison between Puff and Lagrangian Particle Dispersion Models at a Complex and Coastal Site. *Atmosphere*, *13*(4), 508. https://www.mdpi.com/2073-4433/13/4/508

National Aeronautics and Space Administration. (2023). *Carbon Dioxide*. Retrieved 19-04-2023 from https://climate.nasa.gov/vital-signs/carbon-dioxide/

National Library of Medicine *National Center for Biotechnology Information*. (2022). *PubChem Compound Summary for CID 4837, Piperazine*. Retrieved 31-10-2022 from https://pubchem.ncbi.nlm.nih.gov/compound/Piperazine

Neuman, J. A., Trainer, M., Brown, S. S., Min, K. E., Nowak, J. B., Parrish, D. D., Peischl, J., Pollack, I. B., Roberts, J. M., Ryerson, T. B., & Veres, P. R. (2016). HONO Emission and Production Determined from Airborne Measurements over the Southeast U.S. *Journal of Geophysical Research: Atmospheres*, *121*(15), 9237-9250. https://doi.org/10.1002/2016JD025197

Nielsen, C. (2019). *Attachment 6: Klemetsrud CCS Pilot NO_x-Intercomparison*. https://hss.miljodirektoratet.no/api/1/publisert/hoering/vedlegg/16831

Nielsen, C. J., D'Anna, B., Bossi, R., Bunkan, A. J. C., Dithmer, L., Glasius, M., Hallquist, M., Hansen, A. M. K., Lutz, A., Salo, K., Maguta, M. M., Nguyen, Q., Mikoviny, T., Müller, M., Skov, H., Sarrasin, E., Stenstrøm, Y., Tang, Y., Westerlund, J., & Wisthaler, A. (2012). *Atmospheric Degradation of Amines (ADA). Summary Report from Atmospheric Chemistry Studies of Amines, Nitrosamines, Nitramines and Amides* (978-82-992954-7-5). https://www.duo.uio.no/handle/10852/12744

Nielsen, C. J., Herrmann, H., & Weller, C. (2012). Atmospheric Chemistry and Environmental Impact of the Use of Amines in Carbon Capture and Storage (CCS). *Chemical Society Reviews*, *41*(19), 6684-6704. https://doi.org/10.1039/C2CS35059A

Norwegian Institute of Public Health. (2016). *CO_2 Capture: Health Effects of Amines and their Derivatives*. NIPH. Retrieved 31-10-2022 from https://www.fhi.no/en/publ/2011/co2-capture-health-effects-of-amine/

Obermoser, M., Fellner, J., & Rechberger, H. (2009). Determination of Reliable CO_2 Emission Factors for Waste-to-Energy Plants. *Waste Management & Research*, *27*(9), 907-913. https://doi.org/10.1177/0734242x09349763

Onel, L., Brennan, A., Seakins, P. W., Whalley, L., & Heard, D. E. (2017). A New Method for Atmospheric Detection of the CH_3O_2 Radical. *Atmospheric Measurement Techniques*, *10*(10), 3985-4000. https://doi.org/10.5194/amt-10-3985-2017

Onel, L., Dryden, M., Blitz, M. A., & Seakins, P. W. (2014). Atmospheric Oxidation of Piperazine by OH has a Low Potential to Form Carcinogenic Compounds. *Environmental Science & Technology Letters*, *1*(9), 367-371. https://doi.org/10.1021/ez5002159

Paltsev, S., Morris, J., Kheshgi, H., & Herzog, H. (2021). Hard-to-Abate Sectors: The role of Industrial Carbon Capture and Storage (CCS) in Emission Mitigation. *Applied Energy*, *300*, 117322. https://doi.org/10.1016/j.apenergy.2021.117322

Pope, S. B. (1985). PDF Methods for Turbulent Reactive Flows. *Progress in Energy and Combustion Science*, *11*(2), 119-192. https://doi.org/10.1016/0360-1285(85)90002-4

Price, C., & Borgnes, D. (2020). *Dispersion and Deposition Modelling NO_2, Nitrosamines and Nitramines Klemetsrud Carbon Capture Plant*. https://hoering.miljodirektoratet.no/LastNedVedlegg/16833

Putrus, G., & Bentley, E. (2016). 20 - Integration of Distributed Renewable Energy Systems into the Smart Grid. In M. H. Rashid (Ed.), *Electric Renewable Energy Systems* (pp. 487-518). Academic Press. https://doi.org/https://doi.org/10.1016/B978-0-12-804448-3.00020-7

Queensland Government. (2022). *Nitrogen Oxides*. Retrieved 12-01-2023 from https://www.qld.gov.au/environment/management/monitoring/air/air-pollution/pollutants/nitrogen-oxides

Ravnum, S., Rundén-Pran, E., Fjellsbø, L. M., & Dusinska, M. (2014). Human Health Risk Assessment of Nitrosamines and Nitramines for Potential Application in CO_2 Capture. *Regulatory Toxicology and Pharmacology*, *69*(2), 250-255. https://doi.org/10.1016/j.yrtph.2014.04.002

Reynolds, A. J., Verheyen, T. V., Adeloju, S. B., Meuleman, E., & Feron, P. (2012). Towards Commercial Scale Postcombustion Capture of CO_2 with Monoethanolamine Solvent: Key Considerations for Solvent Management and Environmental Impacts. *Environmental Science & Technology*, *46*(7), 3643-3654. https://doi.org/10.1021/es204051s

Ryerson, T. B., Buhr, M. P., Frost, G. J., Goldan, P. D., Holloway, J. S., Hübler, G., Jobson, B. T., Kuster, W. C., McKeen, S. A., Parrish, D. D., Roberts, J. M., Sueper, D. T., Trainer, M., Williams, J., & Fehsenfeld, F. C. (1998). Emissions Lifetimes and Ozone Formation in Power Plant Plumes. *Journal of Geophysical Research: Atmospheres*, *103*(D17), 22569-22583. https://doi.org/10.1029/98JD01620

Ryerson, T. B., Trainer, M., Holloway, J. S., Parrish, D. D., Huey, L. G., Sueper, D. T., Frost, G. J., Donnelly, S. G., Schauffler, S., Atlas, E. L., Kuster, W. C., Goldan, P. D., Hübler, G., Meagher, J. F., & Fehsenfeld, F. C. (2001). Observations of Ozone Formation in Power Plant Plumes and Implications for Ozone Control Strategies. *Science*, *292*(5517), 719-723. https://doi.org/doi:10.1126/science.1058113

Ryu, Y. H., Hodzic, A., Descombes, G., Hall, S., Minnis, P., Spangenberg, D., Ullmann, K., & Madronich, S. (2017). Improved Modeling of Cloudy-Sky Actinic Flux Using Satellite Cloud Retrievals. *Geophysical Research Letters*, *44*(3), 1592-1600. https://doi.org/10.1002/2016GL071892

Scott, V., Gilfillan, S., Markusson, N., Chalmers, H., & Haszeldine, R. S. (2013). Last Chance for Carbon Capture and Storage. *Nature Climate Change*, *3*(2), 105-111. https://doi.org/10.1038/nclimate1695

Scottish Environment Protection Agency. (2013). *Monitoring Quick Guide 5- Version 1.0 - SM-QG-05-Monitoring Oxides of Nitrogen*. https://www.sepa.org.uk/media/156002/qg5_monitoring_nox_sepa_version_1.pdf

Seinfeld, J. H., & Pandis, S. N. (2016). *Atmospheric Chemistry and Physics: From Air Pollution to Climate Change* (3 ed.). John Wiley & Sons, Inc.

Shen, C., Shen, A., Cui, Y., Chen, X., Liu, Y., Fan, Q., Chan, P., Tian, C., Wang, C., Lan, J., Gao, M., Li, X., & Wu, J. (2022). Spatializing the Roughness Length of Heterogenous Urban Underlying Surfaces to Improve the WRF Simulation - Part 1: A Review of Morphological Methods and Model Evaluation. *Atmospheric Environment*, *270*, 118874. https://doi.org/10.1016/j.atmosenv.2021.118874

Shiekh, B. A., Kaur, D., Seth, B., & Mahajan, S. (2016). The Theoretical-Cum-Statistical Approach for the Investigation of Reaction $NO_2 + O(^3P) \rightarrow NO + O_2$ Using SCTST and a Full Anharmonic VPT2 Model. *Chemical Physics Letters*, *662*, 244-249. https://doi.org/10.1016/j.cplett.2016.08.058

Siddi, M. (2016). The EU's Energy Union: A Sustainable Path to Energy Security? *The International Spectator*, *51*(1), 131-144. https://doi.org/10.1080/03932729.2016.1090827

Simmonds, P. G., Palmer, P. I., Rigby, M., McCulloch, A., O'Doherty, S., & Manning, A. J. (2021). Tracers for Evaluating Computational Models of Atmospheric Transport and Oxidation at Regional to Global Scales. *Atmospheric Environment*, *246*, 118074. https://doi.org/10.1016/j.atmosenv.2020.118074

Simonaitis, R., & Heicklen, J. (1973). Reaction of the Hydrogen Peroxide Radical with Ozone. *The Journal of Physical Chemistry*, *77*(16), 1932-1935. https://doi.org/10.1021/j100635a002

Song, R., Muller, J. P., Kharbouche, S., & Woodgate, W. (2019). Intercomparison of Surface Albedo Retrievals from MISR, MODIS, CGLS Using Tower and Upscaled Tower Measurements. *Remote Sensing*, *11*(6), 644. https://www.mdpi.com/2072-4292/11/6/644

Springston, S. R., Kleinman, L. I., Brechtel, F., Lee, Y. N., Nunnermacker, L. J., & Wang, J. (2005). Chemical Evolution of an Isolated Power Plant Plume During the TexAQS 2000 Study. *Atmospheric Environment*, *39*(19), 3431-3443. https://doi.org/10.1016/j.atmosenv.2005.01.060

Stowe, H. M., Paek, E., & Hwang, G. S. (2016). First-Principles Assessment of CO_2 Capture Mechanisms in Aqueous Piperazine Solution. *Physical Chemistry Chemical Physics*, *18*(36), 25296-25307. https://doi.org/10.1039/C6CP03584A

Stull, R. B. (1983). A Heat-Flux History Length Scale for the Nocturnal Boundary Layer. *Tellus A: Dynamic Meteorology and Oceanography*, *35*(3), 219-230. https://doi.org/10.3402/tellusa.v35i3.11435

Tan, W., Zhu, L., Mikoviny, T., Nielsen, C. J., Wisthaler, A., D'Anna, B., Antonsen, S., Stenstrøm, Y., Farren, N. J., Hamilton, J. F., Boustead, G. A., Brennan, A. D., Ingham, T., & Heard, D. E. (2021). Experimental and Theoretical Study of the OH-Initiated Degradation of Piperazine under Simulated Atmospheric Conditions. *The Journal of Physical Chemistry A*, *125*(1), 411-422. https://doi.org/10.1021/acs.jpca.0c10223

Taylor, P. K. (2015). Air Sea Interations | Momentum, Heat and Vapor Fluxes. In G. R. North, J. Pyle, & F. Zhang (Eds.), *Encyclopedia of Atmospheric Sciences (Second Edition)* (pp. 129-135). Academic Press. https://doi.org/10.1016/B978-0-12-382225-3.00064-5

Thakuri, S., Khatri, S. B., & Thapa, S. (2021). Enflamed CO_2 Emissions from Cement Production in Nepal. *Environmental Science and Pollution Research*, *28*(48), 68762-68772. https://doi.org/10.1007/s11356-021-15347-7

Thompson, J. G., Gao, X., Toma, S., Abad, K., Bhatnagar, S., Landon, J., & Liu, K. (2019). Decomposition of N-Nitrosamines Formed in CO_2 Capture Systems through Electrochemically-Mediated Reduction on Carbon Xerogel Electrode. *International Journal of Greenhouse Gas Control*, *83*, 83-90. https://doi.org/10.1016/j.ijggc.2019.02.003

Thomson, D. J. (1987). Criteria for the Selection of Stochastic-Models of Particle Trajectories in Turbulent Flows. *Journal of Fluid Mechanics*, *180*, 529-556. https://doi.org/10.1017/s0022112087001940

Thornton, A. (1988). The Longest Load. *Mærsk Post*, *1*. https://www.maersk.com/~/media_sc9/maersk/corporate/press/publications/files/1988-march-maersk-post-full-issue.pdf

Tomas, J., Van Dijk, A., & Twenhofel, C. (2018). Modelling Atmospheric Dispersion of Radioactivity with NRK-Puff Using Meteorological Data from Hirlam and Harmonie-Arome. Retrieved 17-03-2023, from https://www.narcis.nl/publication/RecordID/oai:rivm.openrepository.com:10029%2F622112

Tønnesen, D. (2011). *Update and Improvement of Dispersion Calculations for Emissions to Air from TCM's Amine Plant. Part II-Likely Case Nitrosamines, Nitramines and Formaldehyde*. https://www.nilu.com/publication/26340/

Trainer, T. (2007). *Renewable Energy Cannot Sustain A Consumer Society*. Springer, Dordrecht. https://doi.org/10.1007/978-1-4020-5549-2_8

United States Environmental Protection Agency. (1999). *Technical Bulletin: Nitrogen Oxides (NO_x), Why and How They Are Controlled*. https://www3.epa.gov/ttncatc1/dir1/fnoxdoc.pdf
United States Environmental Protection Agency. (2017). Revisions to the Guideline on Air Quality Models: Enhancements to the AERMOD Dispersion Modeling System and Incorporation of Approaches to Address Ozone and Fine Particulate Matter. *Federal Register*, *82*(10), 5182-5235. https://www.epa.gov/sites/production/files/2020-09/documents/appw_17.pdf
United States Environmental Protection Agency. (2022a). *What are Volatile Organic Compounds (VOCs)?* Retrieved 31-01-2023 from https://www.epa.gov/indoor-air-quality-iaq/what-are-volatile-organic-compounds-vocs
United States Environmental Protection Agency. (2022b). *What is the Definition of VOC?* Retrieved 31-01-2023 from https://www.epa.gov/air-emissions-inventories/what-definition-voc#:~:text=%22%20Volatile%20organic%20compounds%20(VOC),participates%20in%20atmospheric%20photochemical%20reactions.
Vallero, D. A. (2021). Chapter 10 - Environmental Systems Science Models. In D. A. Vallero (Ed.), *Environmental Systems Science* (pp. 463-507). Elsevier. https://doi.org/10.1016/B978-0-12-821953-9.00017-9.
Van Kampen, N. G. (2007). Chapter XVI - Stochastic Differential Equations. In N. G. Van Kampen (Ed.), *In North-Holland Personal Library - Stochastic Processes in Physics and Chemistry (Third Edition)* (pp. 396-421). Elsevier. https://doi.org/10.1016/B978-044452965-7/50019-2
VanLoon, G. W. (2017). Environmental Chemistry: a Global Perspective. In S. J. Duffy & G. W. vanLoon (Eds.), (Fourth edition. ed., pp. 54-58). Oxford University Press.
Vilà-Guerau de Arellano, J., Talmon, A. M., & Builtjes, P. J. H. (1990). A Chemically Reactive Plume Model for the NO-NO_2-O_3 System. *Atmospheric Environment Part a-General Topics*, *24*(8), 2237-2246. https://doi.org/10.1016/0960-1686(90)90255-l
Vilà-Guerau de Arellano, J., van Heerwaarden, C. C., van Stratum, B. J. H., & van den Dries, K. (2015). *Atmospheric Boundary Layer: Integrating Air Chemistry and Land Interactions*. Cambridge University Press. https://doi.org/10.1017/CBO9781316117422
Voice, A. K., Hill, A., Fine, N. A., & Rochelle, G. T. (2015). Nitrosamine Formation and Mitigation in Blended Amines for CO_2 Capture. *International Journal of Greenhouse Gas Control*, *39*, 329-334. https://doi.org/10.1016/j.ijggc.2015.05.030
Walker, S. E., Solberg, S., & Denby, B. (2003). Development and Implementation of a Simplified EMEP Photochemistry Scheme for Urban Areas in EPISODE. In *NILU Technical Report 13/2003* (pp. 1-28). NILU.
Weatherspark. (2022). *July 12, 2017 Weather History in Oslo Norway*. Retrieved 31-10-2022 from https://weatherspark.com/h/d/68697/2017/7/12/Historical-Weather-on-Wednesday-July-12-2017-in-Oslo-Norway#Figures-CloudCover
Whalley, L. K., Furneaux, K. L., Goddard, A., Lee, J. D., Mahajan, A., Oetjen, H., Read, K. A., Kaaden, N., Carpenter, L. J., Lewis, A. C., Plane, J. M. C., Saltzman, E. S., Wiedensohler, A., & Heard, D. E. (2010). The Chemistry of OH and HO_2 Radicals in the Boundary Layer over the Tropical Atlantic Ocean. *Atmospheric Chemistry and Physics*, *10*(4), 1555-1576. https://doi.org/10.5194/acp-10-1555-2010
Wikipedia. (2022a). *E-Class Container Ship*. Retrieved 20-09-2022 from https://en.wikipedia.org/wiki/E-class_container_ship
Wikipedia. (2022b). *Triple E-Class Container Ship*. Retrieved 20-09-2022 from https://en.wikipedia.org/wiki/Triple_E-class_container_ship#Specifications

Yarwood, G., Shi, Y., & Beardsley, R. (2021). *Develop CB7 Chemical Mechanism for CAMx Ozone Modeling - Final Report*. https://www.tceq.texas.gov/downloads/air-quality/research/reports/photochemical/5822121802020-20210630-ramboll-cb7.pdf

Yoon, B., & Hwang, G. S. (2022). Intriguing Thermal Degradation Behavior of Aqueous Piperazine for Carbon Dioxide Capture: A First-Principles Assessment. *ACS Sustainable Chemistry & Engineering*, *10*(29), 9584-9590. https://doi.org/10.1021/acssuschemeng.2c02502

Yr. (2022). *Blindern*. Retrieved 31-10-2022 from https://www.yr.no/en/statistics/table/1-73738/Norway/Oslo/Oslo/Blindern?q=2017-07-12

Yurkanis Bruice, P. (2017). *Organic Chemistry* (8 (Global) ed.). Pearson Education Limited.

Zaveri, R. A., Berkowitz, C. M., Kleinman, L. I., Springston, S. R., Doskey, P. V., Lonneman, W. A., & Spicer, C. W. (2003). Ozone Production Efficiency and NO_x Depletion in an Urban Plume: Interpretation of Field Observations and Implications for Evaluating O_3-NO_x-VOC Sensitivity. *Journal of Geophysical Research: Atmospheres*, *108*(D14), 1-23. https://doi.org/10.1029/2002JD003144

Zeng, J., Xing, M., Hou, M., England, G. C., & Yan, J. (2018). How Best Management Practices Affect Emissions in Gas Turbine Power Plants - An Important Factor to Consider when Strengthening Emission Standards. *Journal of the Air & Waste Management Association*, *68*(9), 945-957. https://doi.org/10.1080/10962247.2018.1460634

Zheng, J., Fang, F., Wang, Z., Zhu, J., Li, J., Li, J., Xiao, H., & Pain, C. C. (2020). A New Anisotropic Adaptive Mesh Photochemical Model for Ozone Formation in Power Plant Plumes. *Atmospheric Environment*, *229*, 117431. https://doi.org/10.1016/j.atmosenv.2020.117431

Appendices

Appendix 1: Model Input

Appendix 1 contains Table 12 and Table 13, which shows all the input parameters for the SCICHEM GUI that were used to simulate as accurately as possible the projects by Zheng et al. (2020) (section 2.3) and Charlton-Perez et al. (2009) (section 2.4), respectively. Table 12 and Table 13 show the input for the different GUI subgroups: Material, Release, Domain, Time, Weather and Audit.

In addition, Appendix 1 contains Table 14, which shows the input parameters for the SCICHEM GUI that were used for the simulations at the WtE plant (sections 2.5 and 2.6), and Table 15, which shows the SCICHEM input parameters for the WtE plant simulation used for comparison to the Volumetric Particle Approach model (section 2.7). The input for Table 14 is based on the parameters of the Klemetsrud WtE plant. However, the simulations for the WtE plant in this project are not intended as real scenarios for the Klemetsrud WtE plant and should not be treated as such.

Table 12: Input parameters for the SCICHEM GUI used to simulate the conditions used by Zheng et al. (2020) (section 2.3) per section: Material, Release, Domain, Time, Weather and Audit.

Section	Parameter	Input	Reference
Material	Type	Gas	
	Name	NO	
	Units	kg	
	Linear decay: Daytime decay rate (s^{-1})	0	
	Linear decay: Night-time decay rate (s^{-1})	0	
	Density ratio (rho/rho (air))	1.00	(Knipping, 2021b)

Section	Parameter	Input	Reference
	Gas deposition velocity (cm/s)	0.00	
	Minimum concentration (kg/m^3)	0.00	(Knipping, 2021b)
Release	Time (hr)	0.00	
	Lat (N; degrees)	36.3903	(Zheng et al., 2020)
	Lat (E; degrees)	-87.6539	(Zheng et al., 2020)
	Height (m)	193.5	(Chowdhury et al., 2015)
	Material	NO	
	Duration (hr)	11	(Zheng et al., 2020)
	Rate (kg/hr)	1.00	(Knipping, 2021b)
	Multi-component rate (g/s)	NO: 3502.74	(Zheng et al., 2020)
	Active fraction	1.00	(Knipping, 2021b)
	Diameter (m)	16.6	(Chowdhury et al., 2015)
	Exit temperature (°C)	48.2	(Chowdhury et al., 2015)
	x- velocity (m/s)	Default	
	y- velocity (m/s)	Default	
	z- velocity (m/s)	19.60	(Chowdhury et al., 2015)

Section	Parameter	Input	Reference
Time	Local time of 00:00Z	18:00	
	Start time (yyyy.mm.dd)	1995.07.07 hour 00.00	(Zheng et al., 2020)
	Stop time (yyyy.m.d)	1995.07.07 hour 11.00	(Zheng et al., 2020)
	Maximum time step (s)	20	
	Output interval (s)	40	
Domain	Domain reference	Lat./Lon. in Degrees	
	Horizontal Domain	Lat(N): • Min: 35.00 • Max: 37.00 Lon(E): • Min: -90.00 • Max: -84.00 Resolution (deg.): default	
	Vertical Domain	Maximum height (m): 2500.00 Resolution (m): default	(Knipping, 2021b)
Weather	Weather data type	Fixed Winds	(Knipping, 2021b)
	Boundary layer type	Operational	(Knipping, 2021b)
	Large scale variability	Operational	(Knipping, 2021b)

Section	Parameter	Input	Reference
	Surface roughness (m)	0.50	(Knipping, 2021b)
	Precipitation	No precipitation	(Knipping, 2021b)
	Wind speed (m/s)	5.0	(Zheng et al., 2020)
	Wind direction (degrees)	270	(Zheng et al., 2020)
	Bowen Ratio	0.60	(Knipping, 2021b)
	Albedo	0.160	(Knipping, 2021b)
	Fractional Cloud Cover	0.00	(Knipping, 2021b)
Audit	Mode	Standard	
	Dynamics	Dynamics (Buoyant)	
	Static puffs	Enable static puffs	
	Source nests	Disable source nests	

Table 13: Input parameters for the SCICHEM GUI used to simulate the conditions used by Charlton-Perez et al. (2009) (section 2.4) per section: Material, Release, Domain, Time, Weather and Audit.

Section	Parameter	Input	Reference
Material	Type	Gas	
	Name	NO	
	Units	kg	
	Linear decay: Daytime decay rate (s^{-1})	0	

Section	Parameter	Input	Reference
	Linear decay: Night-time decay rate (s^{-1})	0	
	Density ratio (rho/rho (air))	1.00	(Knipping, 2021b)
	Gas deposition velocity (cm/s)	0.00	
	Minimum concentration (kg/m^3)	0.00	(Knipping, 2021b)
Release	Time (hr)	0.00	
	Lat (N; degrees)	15	(Charlton-Perez et al., 2009)
	Lat (E; degrees)	-54	(Charlton-Perez et al., 2009)
	Height (m)	43.2	(Wikipedia, 2022a, 2022b)
	Material	NO	
	Duration (hr)	36.00	(Charlton-Perez et al., 2009)
	Rate (kg/hr)	1.00	(Knipping, 2021b)
	Multi-component rate (g/s)	NO: 33	(Charlton-Perez et al., 2009)
	Active fraction	1.00	(Knipping, 2021b)
	Diameter (m)	2.5	(Thornton, 1988)

Section	Parameter	Input	Reference
	Exit temperature (°C)	44.00	(Price & Borgnes, 2020)
	x- velocity (m/s)	Default	
	y- velocity (m/s)	Default	
	z- velocity (m/s)	13.60	(Price & Borgnes, 2020)
Time	Local time of 00:00Z	20:00	
	Start time (yyyy.mm.dd)	2008.03.21 hour 12.00	(Charlton-Perez et al., 2009)
	Stop time (yyyy.mm.dd)	2008.03.23 hour 12.00	(Charlton-Perez et al., 2009)
	Maximum time step (s)	15.00	(Knipping, 2021b)
	Output interval (s)	30.00	(Knipping, 2021b)
Domain	Domain reference	Lat./Lon. in Degrees	
	Horizontal Domain	Lat(N): • Min: 14.00 • Max: 16.00 Lon(E): • Min: -56.00 • Max: -52.00	

Section	Parameter	Input	Reference
		Resolution (deg.): default	
	Vertical Domain	Maximum height (m): 2500.00 Resolution (m): default	(Knipping, 2021b)
Weather	Weather data type	Fixed Winds	(Knipping, 2021b)
	Boundary layer type	Operational	(Knipping, 2021b)
	Large scale variability	Operational	(Knipping, 2021b)
	Surface roughness (m)	0.50	(Knipping, 2021b)
	Precipitation	No precipitation	(Knipping, 2021b)
	Wind speed (m/s)	4.00	(Charlton-Perez et al., 2009)
	Wind direction (degrees)	90	(Charlton-Perez et al., 2009)
	Bowen Ratio	0.60	(Knipping, 2021b)
	Albedo	0.160	(Knipping, 2021b)
	Fractional Cloud Cover	0.00	(Knipping, 2021b)
Audit	Mode	Standard	
	Dynamics	Dynamics (Buoyant)	
	Static puffs	Enable static puffs	
	Source nests	Disable source nests	

Table 14: Input parameters for the SCICHEM GUI used to simulate the conditions at the Waste-to-Energy plant (sections 2.5 and 2.6) per section: Material, Release, Domain, Time, Weather and Audit.

Section	Parameter	Input	Reference
Material	Type	Gas	
	Name	NO	
	Units	kg	
	Linear decay: Daytime decay rate (s^{-1})	0	
	Linear decay: Night-time decay rate (s^{-1})	0	
	Density ratio (rho/rho (air))	1.00	(Knipping, 2021b)
	Gas deposition velocity (cm/s)	0.00	
	Minimum concentration (kg/m^3)	0.00	
Release	Time (hr)	0.00	
	Lat (N; degrees)	59.9114910	(Price & Borgnes, 2020)
	Lat (E; degrees)	10.7579330	(Price & Borgnes, 2020)
	Height (m)	80	(Price & Borgnes, 2020)
	Material	NO	
	Duration (hr)	24	

Section	Parameter	Input	Reference
	Rate (kg/hr)	1.00	(Knipping, 2021b)
	Multi-component rate (g/s)	NO: 3.02	(Nielsen, 2019; Price & Borgnes, 2020)
	Active fraction	1.00	(Knipping, 2021b)
	Diameter (m)	2.02	(Price & Borgnes, 2020)
	Exit temperature (°C)	44.00	(Price & Borgnes, 2020)
	x- velocity (m/s)	Default	
	y- velocity (m/s)	Default	
	z- velocity (m/s)	12.80	(Price & Borgnes, 2020)
Time	Local time of 00:00Z	02:00	
	Start time (yyyy.mm.dd)	2017.07.12 hour 11.00	
	Stop time (yyyy.mm.dd)	2017.07.12 hour 14.00	
	Maximum time step (s)	20.00	
	Output interval (min)	1.00	
Domain	Domain reference	Lat./Lon. in Degrees	
	Horizontal Domain	Lat(N): • Min: 59.50 • Max: 60.50	

Section	Parameter	Input	Reference
		Lon(E): • Min: 10.20 • Max: 11.20 Resolution (deg.): default	
	Vertical Domain	Maximum height (m): 2500.00 Resolution (m): default	(Knipping, 2021b)
Weather	Weather data type	Fixed Winds	(Knipping, 2021b)
	Boundary layer type	Operational	(Knipping, 2021b)
	Large scale variability	Operational	(Knipping, 2021b)
	Surface roughness (m)	0.50	(Knipping, 2021b)
	Precipitation	No precipitation	(Yr, 2022)
	Wind speed (m/s)	4.00	(Price & Borgnes, 2020)
	Wind direction (degrees)	135	(Price & Borgnes, 2020)
	Bowen Ratio	0.60	(Knipping, 2021b)
	Albedo	0.160	(Knipping, 2021b)
	Fractional Cloud Cover	0.60	(Weatherspark, 2022)
Audit	Mode	Standard	

Section	Parameter	Input	Reference
	Dynamics	Dynamics (Buoyant)	
	Static puffs	Enable static puffs	
	Source nests	Disable source nests	

Table 15: Input parameters for the SCICHEM GUI used to simulate the conditions at the Waste-to-Energy plant per subgroup: Material, Release, Domain, Time, Weather and Audit. Used for comparison with the Volumetric Particle Approach model (section 2.7).

Section	Parameter	Input	Reference
Material	Type	Gas	
	Name	NO	
	Units	kg	
	Linear decay: Daytime decay rate (s^{-1})	0	
	Linear decay: Night-time decay rate (s^{-1})	0	
	Density ratio (rho/rho (air))	1.00	(Knipping, 2021b)
	Gas deposition velocity (cm/s)	0.00	
	Minimum concentration (kg/m^3)	0.00	
Release	Time (hr)	0.00	

Section	Parameter	Input	Reference
	Lat (N; degrees)	59.9114910	(Price & Borgnes, 2020)
	Lat (E; degrees)	10.7579330	(Price & Borgnes, 2020)
	Height (m)	75	
	Material	NO	
	Duration (hr)	24	
	Rate (kg/hr)	1.00	(Knipping, 2021b)
	Multi-component rate (g/s)	NO: 3.013	
	Active fraction	1.00	(Knipping, 2021b)
	Diameter (m)	2.02	(Price & Borgnes, 2020)
	Exit temperature (°C)	44.00	(Price & Borgnes, 2020)
	x- velocity (m/s)	Default	
	y- velocity (m/s)	Default	
	z- velocity (m/s)	12.80	(Price & Borgnes, 2020)
Time	Local time of 00:00Z	02:00	
	Start time (yyyy.mm.dd)	2022.06.01 hour 12.00	

Section	Parameter	Input	Reference
	Stop time (yyyy.mm.dd)	2022.06.01 hour 14.00	
	Maximum time step (s)	20	
	Output interval (min)	1	
Domain	Domain reference	Lat./Lon. in Degrees	
	Horizontal Domain	Lat(N): • Min: 59 • Max: 61 Lon(E): • Min: 9.80 • Max: 11.80 Resolution (deg.): default	
	Vertical Domain	Maximum height (m): 2500.00 Resolution (m): default	(Knipping, 2021b)
Weather	Weather data type	Fixed Winds	(Knipping, 2021b)
	Boundary layer type	Operational	(Knipping, 2021b)
	Large scale variability	Operational	(Knipping, 2021b)
	Surface roughness (m)	0.25	

Section	Parameter	Input	Reference
	Precipitation	No precipitation	(Yr, 2022)
	Wind speed (m/s)	Depending on height (z_i): 4.38, 5.8, 6.7, 7.6, 8.4, 9.2, 10.0, 10.8 z_i: 10m, 35m, 75m, 150 m, 600m, 1200m, 2400 m	
	Wind direction (degrees)	270	
	Bowen Ratio	0.60	(Knipping, 2021b)
	Albedo	0.160	(Knipping, 2021b)
	Fractional Cloud Cover	0.5	
Audit	Mode	Standard	
	Dynamics	Dynamics (Buoyant)	
	Static puffs	Enable static puffs	
	Source nests	Disable source nests	

Appendix 2: Multi-component Input Files

Appendix 2 includes an explanation of the contents of the multi-component files used in the SCICHEM simulations. Moreover, it includes Figure 42 which is the SCICHEM multi-component input file with the ambient conditions and chemistry scheme used by Charlton-Perez et al. (2009) (see section 2.4). The ambient file used, is provided with the SCICHEM download and can be found under the example no2_mc_2005 in the Windows example folder. This multi-component file has been altered to include the species, ambient mixing ratios, and reactions and rate constants as used by Charlton-Perez et al. (2009).

Appendix 2 also includes Figure 43, which is the multi-component input file that was used to compare the SCICHEM output to the output of Particle Approach model by Dr. Massimo Cassiani, senior researcher at NILU (see section 2.7). In the control section (#Control) of the multi-component input file used in the SCICHEM GUI, units for different parameters are specified. The emission units are the emission rate units for the species selected for the multi-component release. There are three options: ppm-m^3/s, molecules-m^3/cm^3-s or g/s. The species units are the units used for the ambient mixing ratios of non-particle species, mentioned in the species section (#Species). There are two options: ppm or molecules cm^{-3}. The default option is ppm, which was used in this project. The rate time units are the units for the rate constants given in the equations section of the multi-component input file. The options are seconds, minutes and hours. The relative tolerance ("rtol") is used to solve the chemical reaction equations. It was set to 0.001 for this project. An ambient file can be added in the control section as well, to specify the background mixing ratios, which vary hourly. Step chemistry can be used to include chemical reactions. When set to true, the chemistry described in the equation section (#Equation) is applied when running the modulation (Knipping, 2021b).

In the species section (#Species) all the chemical species that are considered in the modulation are characterized. All chemical species included in the equation section (#Equation) are mentioned here as well. Type indicates the type of species. There are four options F (fast), S (slow), A (ambient) and P[N/A] (particle). Fast species are species whose mixing ratios change rapidly, and for which the rate equations will be integrated using LSODE. Slow species are species whose mixing ratios change slowly, and whose mixing ratio will be integrated using a predictor-corrector scheme. Ambient species are species whose mixing ratios do not depend on the reactions included in the multi-component file. Particles are the species whose mixing ratios

depend on the aerosol equilibrium. The N or the A after the P indicate whether the species is of the particle number or particle area type. “Tolerance” represents the absolute tolerance. The deposition velocity (“Deposition vel”) represents the gas deposition velocity in m/s. It is possible to enter the deposition velocity directly, or to enter the species properties to determine the deposition velocity. In the second case, Henry’s law constant at 298 K (“H-law”), the temperature correction factor for Henry’s law constant (“T-fact”), the reactivity scaling factor (“Reactvty”) and the surface resistance scaling factor (“Rscale”) must be added. The wet scavenging coefficient in s^{-1} is to be entered under “WetScav”. “MW” represents the molecular weight in g/mol, which is used to determine mixing ratios throughout the simulation. In the “Dos” and “Dep” columns, the dosage and deposition outputs can be turned on (T) or off (F). If one of them is turned on, the other one will automatically be switched on as well, to have the same amount of species in the output files (Knipping, 2021b).

In the group section (#Group), the chemical species groups are formed, e.g. the NO_y group. The table section (#Table) is used for photolysis reactions. The first column indicates the photolysis reaction. The other columns give the radiation constants at different zenith angles. This table is only used from sunrise to sunset. From sunset to sunrise, the radiation constant is set to 0. The balance section (#Balance) shows the number of nitrogen atoms in the species containing nitrogen (Knipping, 2021b).

Finally, the last section, the equation section (#Equation), contains the chemical reactions included in the model. These are retrieved from CB6R2 of CAMx. In a reaction where all the values after the semi colon are zeros, the zenith angle (see table section) is used. For the other equations: the first value is the reaction rate coefficient type (see Page 4-48 of the SCICHEM user guide (Knipping, 2021b)). The following values are the parameters needed for that reaction type. These are shown on page 4-48 of the SCICHEM user guide (Knipping, 2021b).

```
#Control
 &CONTROL
  emission_units = 'g/s',
  species_units = 'ppm',
  rate_time_units = 'sec',
  rtol = 1.e-3,
  step_chemistry =.TRUE.
 /
#Species,Type,Ambient,Tolerance,deposition vel/(H-law T-fact Reactvty Rscale) WetScav MW  dos dep
NO2       F      100.00E-06    1.0000E-08      (1.20E-02 -2500.   0.8       1.)  0.0      46.00    T        T
NO        F      0.0000E+00    1.0000E-08      (1.90E-03 -1400.   0.0       1.)  0.0      30.00    T        T
O3        F      27.000E-03    1.0000E-08      (8.90E-03 -2900.   1.0       1.)  0.0      48.00    T        T
NO3       F      0.0000E+00    1.0000E-12      (1.80E+00 -4000.   0.1       0.)  0.0      62.00    T        T
O1D       F      0.0000E+00    1.0000E-12      (0.0      0.       0.0       0.)  0.0      16.00
OH        F      0.3660E-06    1.0000E-12      (0.0      0.       0.0       0.)  0.0      17.00
HO2       F      0.0000E+00    1.0000E-12      (0.0      0.       0.0       0.)  0.0      33.00
CH2O      F      100.00E-06    1.0000E-08      (3.20E+03 -6800.   1.0       1.)  0.0      30.00    T        T
CH3OOH    F      100.00E-06    1.0000E-12      (3.10E+02 -5200.   1.0       0.)  0.0      48.00
CH3O2     F      0.0000E+00    1.0000E-12      (0.0      0.       0.0       0.)  0.0      47.00
N2O5      F      0.0000E+00    1.0000E-12      (1.00E+05 -4000.   0.1       0.)  0.0      108.00   T        T
HNO3      F      0.0000E+00    1.0000E-08      (2.10E+05 -8700.   0.0       0.)  0.0      63.00    T        T
H2O2      F      100.00E-06    1.0000E-08      (8.60E+04 -6500.   1.0       0.)  0.0      34.00
PAN       F      0.0000E+00    1.0000E-08      (4.10E+00 -4000.   1.0       1.)  0.0      121.00   T        T
CH4       A      1.9450E+00    1.0000E-08      (1.40E-03 -1600.   0.0       1.)  0.0      16.00
CO        A      2.2000E-01    1.0000E-04      (9.90E-04 -1300.   0.0       1.)  0.0      28.00    T        T
H2O       A           -1.0             1.0000E-06   0.0      0.0  18.02
#Group
GNOY NO NO2 HNO3 N2O5 NO3 PAN
#Table
   0          0.         10.         20.         30.         40.         50.         60.         70.         78.         86.
   1  3.780E-05   3.654E-05   3.290E-05   2.734E-05   2.056E-06   1.345E-05   7.031E-05   2.341E-06   4.021E-07  6.557E-10
   2  8.920E-03   8.850E-03   8.636E-03   8.264E-03   7.704E-03   6.904E-03   5.767E-03   4.108E-03   2.199E-03  1.324E-04
   3  4.815E-05   4.754E-05   4.569E-05   4.257E-05   3.807E-05   3.205E-05   2.430E-05   1.463E-05   5.931E-06  7.788E-07
   4  3.261E-05   3.206E-05   3.041E-05   2.767E-05   2.390E-05   1.914E-05   1.351E-05   7.302E-06   2.568E-06  3.871E-08
   5  2.231E-02   2.222E-02   2.219E-02   2.141E-02   2.064E-02   1.950E-02   1.782E-02   1.513E-02   1.135E-02  3.378E-03
   6  1.542E-01   1.535E-01   1.515E-01   1.479E-03   1.424E-01   1.343E-01   1.222E-01   1.026E-01   7.507E-02  1.927E-02
#Balance  : N
NO        1.0
NO2       1.0
HNO3      1.0
N2O5      2.0
PAN       1.0
NO3       1.0
#Equations -- CB6R2 from CAMx
  1 [O3]   ->  [O1D]           ;  0  0.000E+00  0.0000E+00
  2 [NO2] -> [NO] + [O3]       ;  0  0.000E+00  0.0000E+00
  3 [CH2O] -> [CO]             ;  0  0.000E+00  0.0000E+00
  4 [CH2O] -> [CO] + (2) [HO2] ; 0  0.000E+00  0.0000E+00
  5 [NO3]  ->  [NO]            ;  0  0.000E+00  0.0000E+00
  6 [NO3] -> [NO2] + [O3]      ;  0  0.000E+00  0.0000E+00
  7 [NO] + [O3] -> [NO2]       ;  2  1.400E-12 -1.3100E+03
  8 [OH] + [CO] -> [HO2]       ;  1  1.300E-13
  9 [OH] + [CH4] -> [CH3O2]    ;  2  9.650E-20 -1.082E+03  2.58
 10 [HO2] + [NO] -> [OH] + [NO2]; 2 3.600E-12  2.7000E+02
 11 [HO2] + [O3] -> [OH]       ; 22  2.030E-16  6.9300E+02  4.57
 12 [CH3O2] + [NO] -> [NO2] + [CH2O] + [HO2]; 2  1.820E-13  4.160E+02
 13 [CH3O2] + [HO2] -> [CH3OOH]; 2   3.800E-13  7.800E+02
 14 [HO2] -> [H2O2]    ; 20  1.850E-32  2.80E+03 1.596E-52 3.18E+03
 15 [OH] + [NO2] -> [HNO3]     ; 11  3.3E-30 -3.0  4.1E-11  0.4
 16 [OH] + [HO2] ->            ;  2  4.800E-11  2.500E+02
 17 (2) [CH3O2] ->             ;  2  1.820E-13  4.160E+02
 18 [NO2] + [O3] -> [NO3]      ;  2  1.400E-13 -2.470E+03
 19 [NO] + [NO3] -> (2) [NO2]; 2  1.800E-11  1.100E+02
 20 [NO2] + [NO3] -> [N2O5]    ; 23  3.60E-30 -4.1 0.0 1.90E-12  0.2 0.0 0.35 1.33
 21 [N2O5] -> [NO2] + [NO3]   ;  23  1.00E-03 -3.5 -1.100E+04 9.7E+14 0.1 -1.108E+04 0.35 1.33
 22 [PAN]  -> [NO2]            ;  1  9.250E+03
 23 [N2O5] -> (2) [HNO3]      ; 1  4.000E-04
 24 [NO2] + [NO3] -> [NO2] + [NO]; 2 4.500E-14 -1.260E+03
```

Figure 42: The multi-component input file used in the SCICHEM GUI to compare the model output to the actual measurements performed by Charlton-Perez, using the exact same parameters (i.e. rate constants and background concentrations) as Charlton-Perez (see section 2.4) (Charlton-Perez et al., 2009).

```
#Control
 &CONTROL
  emission_units = 'g/s',
  species_units = 'ppm',
  rate_time_units = 'sec',
  rtol = 1.e-3,
  step_chemistry = .true.,
/
#Species,Type,Ambient,Tolerance,deposition vel/(H-law T-fact Reactvty Rscale) WetScav MW  dos dep
NO2       F      5.6100E-04    1.0000E-08      (1.20E-02 -2500.   0.8       1.)  0.0     46.00    T       T
NO        F      1.6700E-04    1.0000E-08      (0.0      0.       0.0       0.)  0.0     30.00    T       T
O         F      1.7500E-10    1.0000E-12      (0.0      0.       0.0       0.)  0.0     16.00
O3        F      3.4400E-02    1.0000E-08      (8.90E-03 -2900.   1.0       1.)  0.0     48.00    T       T
NO3       F      7.8500E-08    1.0000E-12      (0.0      0.       0.0       0.)  0.0     62.00    T       T
O1D       F      5.8900E-16    1.0000E-12      (0.0      0.       0.0       0.)  0.0     16.00
OH        F      3.0400E-07    1.0000E-12      (0.0      0.       0.0       0.)  0.0     17.00
HO2       F      1.0600E-05    1.0000E-12      (0.0      0.       0.0       0.)  0.0     33.00
N2O5      F      6.0600E-08    1.0000E-12      (0.0      0.       0.0       0.)  0.0     108.00   T       T
HNO3      F      2.0700E-04    1.0000E-08      (2.10E+05 -8700.   0.0       0.)  0.0     63.00    T       T
H2O2      F      2.8800E-04    1.0000E-08      (8.60E+04 -6500.   1.0       0.)  0.0     34.00
HCHO      F      1.0800E-03    1.0000E-08      (0.0      0.       0.0       0.)  0.0     30.00    T       T
CH3CHO    F      3.0100E-04    1.0000E-08      (0.0      0.       0.0       0.)  0.0     44.00
CH3COC2H5 F      1.9100E-05    1.0000E-08      (0.0      0.       0.0       0.)  0.0     72.00
CH3COCHO  F      2.0000E-05    1.0000E-08      (0.0      0.       0.0       0.)  0.0     72.00
CH4       F      1.7300E+00    1.0000E-08      (0.0      0.       0.0       0.)  0.0     16.00
CO        S      1.0000E-01    1.0000E-04      (0.0      0.       0.0       0.)  0.0     28.00    T       T
CH3O2     F      3.4100E-06    1.0000E-12      (0.0      0.       0.0       0.)  0.0     47.00
CH3O2H    F      1.1400E-05    1.0000E-12      (3.10E+02 -5200.   1.0       0.)  0.0     48.00
CH3OH     F      3.9900E-34    1.0000E-12      (0.0      0.       0.0       0.)  0.0     32.00
HCOCHO    F      5.5300E-06    1.0000E-08      (0.0      0.       0.0       0.)  0.0     58.00
CH3COO2   F      3.4700E-07    1.0000E-12      (0.0      0.       0.0       0.)  0.0     75.00
PAN       F      2.0800E-04    1.0000E-08      (0.0      0.       0.0       0.)  0.0     121.00   T       T
C3H6      F      4.3100E-05    1.0000E-08      (0.0      0.       0.0       0.)  0.0     42.00
CH3CHO2CH2OH      F      2.8800E-07    1.0000E-08      (0.0      0.       0.0       0.)  0.0      91.00
CH2O2CH2OH        F      2.2600E-07    1.0000E-08      (0.0      0.       0.0       0.)  0.0      77.00
CH3COCOCH3        F      4.0700E-34    1.0000E-08      (0.0      0.       0.0       0.)  0.0      86.00
CH3COCHO2CH3      F      8.3300E-09    1.0000E-08      (0.0      0.       0.0       0.)  0.0     103.00
C2H4      F      1.2000E-04    1.0000E-08      (0.0      0.       0.0       0.)  0.0     28.00
OXYLENE   F      6.2600E-05    1.0000E-08      (0.0      0.       0.0       0.)  0.0     106.00
OXYLOHO2  F      3.9600E-07    1.0000E-08      (0.0      0.       0.0       0.)  0.0     187.00
MEMALDIAL F      1.0300E-05    1.0000E-08      (0.0      0.       0.0       0.)  0.0     98.00
MEMALO2   F      1.1800E-07    1.0000E-08      (0.0      0.       0.0       0.)  0.0     147.00
ISOPRENE  F      8.1300E-35    1.0000E-08      (0.0      0.       0.0       0.)  0.0     68.00
ISOPO2    F      2.9500E-36    1.0000E-08      (0.0      0.       0.0       0.)  0.0     101.00
MVKETONE  F      8.5000E-34    1.0000E-08      (0.0      0.       0.0       0.)  0.0     70.00
MVKO2     F      4.8800E-35    1.0000E-08      (0.0      0.       0.0       0.)  0.0     119.00
SO2       F      1.0800E-04    1.0000E-08      (1.30E+00 -1800.   0.0       1.)  0.0     64.00    T       T
SULFATE   F      1.9300E-06    1.0000E-08      (1.00E+10 0.       0.0       0.)  0.0     98.00    T       T
C2H5OH    F      3.8500E-34    1.0000E-12      (0.0      0.       0.0       0.)  0.0     46.00
C2H6      F      1.4600E-03    1.0000E-12      (0.0      0.       0.0       0.)  0.0     30.00
C2H5O2    F      1.9900E-07    1.0000E-12      (0.0      0.       0.0       0.)  0.0     61.00
nC4H10    F      7.4400E-04    1.0000E-12      (0.0      0.       0.0       0.)  0.0     58.00
secC4H9O2 F      4.0400E-07    1.0000E-12      (0.0      0.       0.0       0.)  0.0     89.00
H2        F      5.6900E-01    1.0000E-08      (0.0      0.       0.0       0.)  0.0     2.00
H2O       A           -1.0              1.0000E-06   0.0      0.0  18.02
#Group
GNOY NO NO2 PAN HNO3 N2O5 NO3
#Table
    0          0.         10.         20.         30.         40.         50.         60.         70.         78.         86.
58      4.826E-04   2.243E-05   3.677E-03   1.041E+00   1.458E-05   5.077E-04   1.957E-03   6.899E-03   8.818E-02   4.357E+03
59      1.423E-03   3.821E-04   3.398E-03   3.819E-02   3.177E-04   1.455E-03   2.593E-03   4.450E-03   1.326E-02   1.362E+00
60      1.406E-02   5.851E-03   2.512E-02   1.260E-01   5.174E-03   1.427E-02   2.098E-02   3.007E-02   6.226E-02   1.366E+00
61      2.934E-05   5.670E-06   8.708E-05   1.792E-03   4.502E-06   3.015E-05   6.212E-05   1.220E-04   4.777E-04   1.562E-01
62      6.335E-06   4.092E-07   3.883E-05   6.001E-03   2.786E-07   6.629E-06   2.211E-05   6.811E-05   6.625E-04   1.028E+01
63      7.198E-05   1.274E-05   2.264E-04   5.475E-03   9.994E-06   7.408E-05   1.586E-04   3.229E-04   1.360E-03   6.056E-01
64      7.452E-05   2.001E-05   1.779E-04   2.000E-03   1.663E-05   7.616E-05   1.358E-04   2.330E-04   6.944E-04   7.133E-02
65      2.108E-05   2.686E-06   8.242E-05   3.649E-03   2.012E-06   2.181E-05   5.397E-05   1.258E-04   6.959E-04   9.866E-01
66      3.738E-05   5.468E-06   1.334E-04   4.581E-03   4.175E-06   3.859E-05   8.985E-05   1.978E-04   9.762E-04   8.509E-01
67      1.554E-04   2.273E-05   5.544E-04   1.904E-02   1.735E-05   1.604E-04   3.735E-04   8.223E-04   4.057E-03   3.537E+00
68      7.912E-04   1.401E-04   2.489E-03   6.018E-02   1.098E-04   8.143E-04   1.743E-03   3.550E-03   1.495E-02   6.657E+00
69      2.565E-02   2.147E-02   2.884E-02   3.999E-02   2.095E-02   2.572E-02   2.781E-02   2.991E-02   3.466E-02   6.478E-02
70      6.354E-02   5.583E-02   6.922E-02   8.781E-02   5.483E-02   6.367E-02   6.740E-02   7.108E-02   7.913E-02   1.248E-01
71      3.600E-05   1.039E-05   8.193E-05   8.061E-04   8.726E-06   3.675E-05   6.346E-05   1.057E-04   2.967E-04   2.362E-02
72      2.595E-05   6.668E-06   6.379E-05   7.772E-04   5.510E-06   2.654E-05   4.824E-05   8.429E-05   2.605E-04   3.123E-02
#Balance  : N
NO        1.0
NO2       1.0
PAN       1.0
HNO3      1.0
N2O5      2.0
NO3       1.0
#Equations -- CB6R2 from CAMx
 1 [O] -> [O3]; 24 5.67E-34 0.0 -2.8
 2 [O1D] -> [O]; 5  1.340E-09  1.1500E+02
 3 [O] + [NO] -> [NO2]; 24  6.000E-30  0.0000E+00 -1.6
 4 [O1D] -> (2.0) [OH]; 1 2.200E-10
 5 [O3] + [NO] -> [NO2]; 2 1.400E-12 -1310 0.0
 6 [O3] + [NO2] -> [NO3]; 2 1.400E-13 -2470 0.0
 7 [O3] + [OH] -> [HO2]; 2 1.700E-12 -940 0.0
 8 [O3] + [HO2] -> [OH]; 22  1.220E-14  6.9300E+02  4.57
 9 [NO] + [NO3] -> (2.0) [NO2]; 2 1.800E-11 110 0.0
10 [NO] + [HO2] -> [NO2] + [OH]; 2 3.600E-12 270 0.0
11 [NO2] + [NO3] -> [NO] + [NO2]; 2 4.500E-14 -1260 0.0
12 [NO2] + [NO3] -> [N2O5]; 23  2.16E-28 -4.1 0.0 1.14E-10  0.2 0.0 0.35 1.33
13 [NO2] + [OH] -> [HNO3]; 11  1.080E-28 -3.0  1.68E-09  0.0
14 [N2O5] -> [NO2] + [NO3]; 23  7.80E-02 -3.5 -1.100E+04 5.82E+16 0.1 -1.108E+04 0.35 1.33
15 [OH] + [H2] -> [HO2]; 2 7.700E-12 -2100 0.0
16 [OH] + [HO2] -> ; 2 4.800E-11 -160 0.0
17 [OH] + [H2O2] -> [HO2]; 2 2.900E-12 -160 0.0
18 [HO2] + [HO2] -> [H2O2]; 19  1.320E-11  6.00E+02 1.140E-31 9.80E+02
19 [OH] + [HNO3] -> [NO3]; 13  1.44E-12  460.  1.62E-15  2.199E+03  3.90E-32  1335.
20 [SO2] + [OH] -> [HO2] + [SULFATE]; 23  2.70E-29 -3.9 0.0 7.80E-11  0.7 0.0 0.53 1.1
21 [SO2] + [CH3O2] -> [SULFATE] + [HCHO] + [HO2];1 4.000E-17
22 [CH4] + [OH] -> [CH3O2]; 2 1.850E-12 -1690 0.0
23 [CH3O2] + [NO] -> [HCHO] + [HO2] + [NO2]; 2 2.800E-12 285 0.0
24 [CH3OH] + [OH] -> [HCHO] + [HO2]; 2  1.710E-10 -3.45E+02
25 [CH3O2] + [HO2] -> [CH3O2H]; 2 3.800E-13 780 0.0
26 [CH3O2H] + [OH] -> [HCHO] + [OH]; 2 1.000E-12 190 0.0
27 [CH3O2H] + [OH] -> [CH3O2]; 2 1.900E-12 190 0.0
28 [HCHO] + [OH] -> [CO] + [HO2]; 2 8.200E-12 40 0.0
29 [HCHO] + [NO3] -> [CO] + [HO2] + [HNO3]; 1 5.800E-16
30 [CO] + [OH] -> [HO2]; 19  8.640E-12 0.0 2.058E-31 0.0
31 [C2H6] + [OH] -> [C2H5O2]; 2 6.900E-12 -1000 0.0
32 [C2H5O2] + [NO] -> [CH3CHO] + [HO2] + [NO2]; 2 2.500E-12 380 0.0
33 [CH3CHO] + [OH] -> [CH3COO2]; 2 4.400E-12 365 0.0
34 [CH3COO2] + [NO2] -> [PAN];23  1.62E-26 -7.1 0.0 7.20E-10 -0.9 0.0 0.3 1.41
35 [PAN] -> [CH3COO2] + [NO2]; 23  2.94E-01 0.0 -1.21E+04 3.24E+18 0.0 -1.383E+04 0.3  1.41
36 [CH3COO2] + [NO] -> [CH3O2] + [NO2]; 2 7.800E-12 300 0.0
37 [C2H5OH] + [OH] -> [CH3CHO] + [HO2]; 2 4.100E-12 -70 0.0
38 [nC4H10] + [OH] -> [secC4H9O2]; 2 9.100E-12 -405 0.0
39 [secC4H9O2] + [NO] -> (0.65) [CH3COC2H5] + (0.35) [CH3CHO] + (0.35) [C2H5O2] + (0.65) [HO2] + [NO2]; 2 4.200E-12 180 0.0
40 [CH3COC2H5] + [OH] -> [CH3COCHO2CH3]; 2 1.300E-12 -25 0.0
41 [CH3COCHO2CH3] + [NO] -> [NO2] + [CH3COO2] + [CH3CHO]; 1 5.00E-12
42 [C2H4] + [OH] -> [CH2O2CH2OH]; 23  7.0E-29 -3.1 0.0 9.0E-12  0.0 0.0 0.48 0.00
43 [CH2O2CH2OH] + [NO] -> (2.0) [HCHO] + [HO2] + [NO2]; 2 4.200E-12 180 0.0
44 [C2H4] + [O3] -> [HCHO] + (0.42) [CO] + (0.12) [HO2] + (0.12) [H2]; 2 9.100E-15 -2580 0.0
45 [C3H6] + [OH] -> [CH3CHO2CH2OH]; 23  8.0E-27 -3.5 0.0 3.0E-11  0.0 0.0 0.50 0.00
46 [CH3CHO2CH2OH] + [NO] -> [CH3CHO] + [HCHO] + [HO2] + [NO2]; 2 4.200E-12 180 0.0
47 [C3H6] + [O3] -> (0.50) [CH3CHO] + (0.50) [HCHO] + (0.07) [CH4] + (0.40) [CO] + (0.31) [CH3O2] + (0.28) [HO2] + (0.15) [OH] + (0.07) [H2]; 2 5.500E-15 -1880
48 [OXYLENE] + [OH] -> [OXYLOHO2]; 1 1.400E-11
49 [OXYLOHO2] + [NO] -> [MEMALDIAL] + [CH3COCHO] + [HO2] + [NO2]; 1 4.000E-12
50 [MEMALDIAL] + [OH] -> [MEMALO2]; 1  5.600E-11
51 [MEMALO2] + [NO] -> [CH3COCHO] + [HCOCHO] + [HO2] + [NO2]; 1  9.000E-12
52 [CH3COCHO] + [OH] -> [CH3COO2] + [CO]; 1 1.700E-11
53 [HCOCHO] + [OH] -> [HO2] + (2.0) [CO]; 1 1.200E-11
54 [ISOPRENE] + [OH] -> [ISOPO2]; 2 2.700E-11 390 0.0
55 [ISOPO2] + [NO] -> [MVKETONE] + [HCHO] + [HO2] + [NO2]; 2 4.200E-12 180 0.0
56 [MVKETONE] + [OH] -> [MVKO2]; 2 4.100E-12 453 0.0
57 [MVKO2] + [NO] -> [CH3COCHO] + [HCHO] + [HO2] + [NO2]; 2 1.400E-12 -180 0.0
58 [O3] -> [O1D]; 0  0.000E+00  0.0000E+00
59 [O3] -> [O]; 0  0.000E+00  0.0000E+00
60 [NO2] -> [O] + [NO]; 0  0.000E+00  0.0000E+00
61 [H2O2] -> (2.0) [OH]; 0  0.000E+00  0.0000E+00
62 [HNO3] -> [NO2] + [OH]; 0  0.000E+00  0.0000E+00
63 [HCHO] -> [CO] + (2.0) [HO2]; 0  0.000E+00  0.0000E+00
64 [HCHO] -> [CO] + [H2]; 0  0.000E+00  0.0000E+00
65 [CH3CHO] -> [CH3O2] + [HO2] + [CO]; 0  0.000E+00  0.0000E+00
66 [CH3COC2H5] -> [CH3COO2] + [C2H5O2]; 0  0.000E+00  0.0000E+00
67 [CH3COCHO] -> [CH3CHO] + [CO]; 0  0.000E+00  0.0000E+00
68 [HCOCHO] -> [HCHO] + [CO]; 0  0.000E+00  0.0000E+00
69 [NO3] -> [NO]; 0  0.000E+00  0.0000E+00
70 [NO3] -> [NO2] + [O]; 0  0.000E+00  0.0000E+00
71 [N2O5] -> [NO2] + [NO3]; 0  0.000E+00  0.0000E+00
72 [CH3O2H] -> [HCHO] + [OH] + [HO2]; 0  0.000E+00  0.0000E+00
```

Figure 43: The multi-component input file containing the adapted EMEP chemistry scheme and ambient volume mixing ratios provided by NILU. This file was applied in the SCICHEM GUI to compare the SCICHEM and Volumetric Particle Approach models (see section 2.7).

Appendix 3: NILU-Provided Ambient Conditions

Appendix 3 contains Table 16, which holds the species and their ambient VMRs for the WtE plant simulations. These were provided by NILU and are valid for short range distances (up to approx. 30 km). The same species and VMRs are included in the species section in Figure 43 in Appendix 2.

Table 16: The species and corresponding ambient volume mixing ratios considered in the WtE plant simulations. These are also shown in Figure 43 in Appendix 2. The content of this table has been provided by the Norwegian Institute for Air Research (NILU), and are valid for short range distances (approx. 30 km) from the source.

Species	**Volume Mixing Ratio (ppm)**
$O(^3P)$	1.75E-10
$O(^1D)$	5.89E-16
OH	3.04E-07
O_3	3.44E-02
HO_2	1.06E-05
H_2O_2	2.80E-04
NO	1.67E-04
NO_2	5.61E-04
NO_3	7.85E-08
N_2O_5	6.06E-08
HNO_3	2.07E-04
SO_2	1.08E-04
Sulphate (SO_4^{2-})	1.93E-06
H_2	5.69E-01

Species	Volume Mixing Ratio (ppm)
CH_4	1.73E+00
CH_3O_2	3.41E-06
Formaldehyde (HCHO)	1.08E-03
Methanol (CH_3OH)	3.99E-34
CH_3O_2H	1.14E-05
CO	1.00E-01
Ethane (C_2H_6)	1.46E-03
Ethyldioxy ($C_2H_5O_2$)	1.90E-07
Acetaldehyde (CH_3CHO)	3.01E-04
$CH_3C(O)O_2$	3.47E-07
PAN	2.08E-04
C_2H_5OH	3.85E-34
N-butane (nC_4H_{10})	7.44E-04
sec$C_4H_9O_2$	4.04E-07
$CH_3COC_2H_5$	1.91E-05
$CH_3COCHO_2CH_3$	8.33E-09
$CH_3COCOCH_3$	4.07E-34
Ethene (C_2H_4)	1.20E-04
$CH_2O_2CH_2OH$	2.26E-07

Species	Volume Mixing Ratio (ppm)
Propene (C_3H_6)	4.31E-05
$CH_3CHO_2CH_2OH$	2.88E-07
oXylen ($C_6H_4(CH_3)CH_3$)	6.26E-05
oXylOHO$_2$ ($C_6H_3H(O_2)CH_3(OH)CH_3O_2$)	3.96E-07
Memaldial ($CH_3COCH=CHCHO$)	1.03E-05
CH_3COCHO	2.00E-05
MemalO$_2$ ($CH_3COCHOH\text{-}CH(O_2)CHO$	1.18E-07
Glyoxal (HCOCHO)	5.53E-06
Isoprene (C_5H_8)	8.13E-35
IsopO$_2$ ($OHC_5H_8O_2$)	2.95E-36
MVKetone ($CH_3COCH=CH_2$)	8.50E-34
MVKO$_2$ ($OHCH_3COCHCH_2O_2$)	4.88E-35

Appendix 4: Calculations

Appendix 4 contains the detailed calculations used in sections 2.5, 2.6 and 3.4 of the main text to convert 55 ppm NO, 200 ppb CH_3CHO, 200 ppb PZ and 1 ppb PZNO to g/s. For these calculations the flow of one stack of the Klemetsrud WtE plant was used. However, the simulations do in no way represent the Klemetsrud WtE plant. Appendix 4 also shows the calculations to convert 0.272 ppt and 0.174 ppt $PZNO_2$ and 0.389 ppt PZNO to ng/m^3. For these calculations a standard temperature and pressure of 25 ℃ and 1 atm were assumed (Breeze Technologies, 2021).

Conversion of 55 ppm Nitrogen Monoxide to g/s

- 1 cm^3 of air: $2.7 \cdot 10^{19}$ molecules (Cohen & Taylor, 1987)
- 1 m^3 of air: $2.7 \cdot 10^{25}$ molecules
- Flow: 147194 m^3/h (Price & Borgnes, 2020)
- $147194 \frac{m^3}{h} = 147194 * 2.7 \cdot 10^{25} \frac{molecules}{h} = 3.974238 \cdot 10^{30} \frac{molecules}{h}$
- 55 ppm = $55 \cdot 10^{-6} = 55 \cdot 10^{-4}\%$
- $\frac{3.974238 \cdot 10^{30}}{100} \cdot 55 \cdot 10^{-4}\% = 2.1858309 \cdot 10^{26} \frac{molecules\ NO}{h}$
- $\frac{2.1858309 \cdot 10^{26}}{6.022 \cdot 10^{23}} = 362.9742444 \frac{mol\ NO}{h}$
- $362.9742444 \cdot 30 = 10889.22733 \frac{g\ NO}{h}$
- $\frac{10889.22733}{3600} = 3.02478537 \approx 3.02 \frac{g\ NO}{s}$

Conversion of 200 ppb Acetaldehyde to g/s

- 1 cm^3 of air: $2.7 \cdot 10^{19}$ molecules (Cohen & Taylor, 1987)
- 1 m^3 of air: $2.7 \cdot 10^{25}$ molecules
- Flow: 147194 m^3/h (Price & Borgnes, 2020)
- $147194 \frac{m^3}{h} = 147194 * 2.7 \cdot 10^{25} \frac{molecules}{h} = 3.974238 \cdot 10^{30} \frac{molecules}{h}$
- 200 ppb = 0.2 ppm = $0.2 \cdot 10^{-6}$ = $0.2 \cdot 10^{-4}\%$
- $\frac{3.974238 \cdot 10^{30}}{100} \cdot 0.2 \cdot 10^{-4}\% = 7.948476 \cdot 10^{23} \frac{molecules\ CH_3CHO}{h}$
- $\frac{7.948476 \cdot 10^{23}}{6.022 \cdot 10^{23}} = 1.319906343 \frac{mol\ CH_3CHO}{h}$
- $1.319906343 \cdot 44 = 58.07587911 \frac{g\ CH_3CHO}{h}$
- $\frac{58.07587911}{3600} = 0.016132188 \approx 0.016 \frac{g\ CH_3CHO}{s}$

Conversion of 200 ppb Piperazine to g/s

- 1 cm^3 of air: $2.7 \cdot 10^{19}$ molecules (Cohen & Taylor, 1987)
- 1 m^3 of air: $2.7 \cdot 10^{25}$ molecules
- $147194 \frac{m^3}{h} = 147194 * 2.7 \cdot 10^{25} \frac{molecules}{h} = 3.974238 \cdot 10^{30} \frac{molecules}{h}$
- 200 ppb = $200 \cdot 10^{-9}$ = $200 \cdot 10^{-7}\%$
- $\frac{3.974238 \cdot 10^{30}}{100} \cdot 200 \cdot 10^{-7}\% = 7.948476 \cdot 10^{23} \frac{molecules\ PZ}{h}$
- $\frac{7.948476 \cdot 10^{23}}{6.022 \cdot 10^{23}} = 1.319906343 \frac{mol\ PZ}{h}$
- $1.319906343 \cdot 86.4 = 114.0399081 \frac{g\ PZ}{h}$
- $\frac{114.0399081}{3600} = 0.031677752 \approx 0.032 \frac{g\ PZ}{s}$

Conversion of 1 ppb Piperazine Nitrosamine to g/s

- 1 cm^3 of air: $2.7 \cdot 10^{19}$ molecules (Cohen & Taylor, 1987)
- 1 m^3 of air: $2.7 \cdot 10^{25}$ molecules
- Flow: 147194 m^3/h (Price & Borgnes, 2020)
- $147194 \frac{m^3}{h} = 147194 * 2.7 \cdot 10^{25} \frac{molecules}{h} = 3.974238 \cdot 10^{30} \frac{molecules}{h}$
- 1 ppb = $1 \cdot 10^{-9}$ = $1 \cdot 10^{-7}\%$
- $\frac{3.974238 \cdot 10^{30}}{100} \cdot 1 \cdot 10^{-7}\% = 3.974238 \cdot 10^{21} \frac{molecules\ PZ}{h}$
- $\frac{3.974238 \cdot 10^{21}}{6.022 \cdot 10^{23}} = 6.599531717 \cdot 10^{-3} \frac{mol\ PZ}{h}$
- $6.599531717 \cdot 10^{-3} \cdot 115 = 0.758946147 \frac{g\ PZ}{h}$
- $\frac{0.758946147}{3600} = 2.108183743 \cdot 10^{-4} \approx 2.1 \cdot 10^{-4} \frac{g\ PZ}{s}$

Conversion of 0.207 ppt Piperazine Nitrosamine to ng/m³

- 0.207 ppt Nitrosamine (PZNO, $C_4H_9N_2NO$)
- Concentration ($\mu g/m^3$) = $\frac{Molecular\ Weight \cdot Concentration\ (ppb)}{24.45}$ (Breeze Technologies, 2021)
- Concentration ($\mu g/m^3$) = $\frac{115 \cdot 0.207 \cdot 10^{-3}}{24.45}$
- Concentration ($\mu g/m^3$) ≈ 0.00097
- Concentration (ng/m^3) ≈ 0.97

Conversion of 0.134 ppt Piperazine Nitramine to ng/m^3

- 0.134 ppt Nitramine ($PZNO_2$, $C_4H_9N_2NO_2$)
- Concentration ($\mu g/m^3$) = $\frac{Molecular\ Weight \cdot Concentration\ (ppb)}{24.45}$ (Breeze Technologies, 2021)
- Concentration ($\mu g/m^3$) = $\frac{131 \cdot 0.134 \cdot 10^{-3}}{24.45}$
- Concentration ($\mu g/m^3$) ≈ 0.00072
- Concentration (ng/m^3) ≈ 0.72

Conversion of 0.327 ppt Piperazine Nitrosamine to ng/m^3

- 0.327 ppt Nitrosamine (PZNO, $C_4H_9N_2NO$)
- Concentration ($\mu g/m^3$) = $\frac{Molecular\ Weight \cdot Concentration\ (ppb)}{24.45}$ (Breeze Technologies, 2021)
- Concentration ($\mu g/m^3$) = $\frac{115 \cdot 0.327 \cdot 10^{-3}}{24.45}$
- Concentration ($\mu g/m^3$) ≈ 0.00154
- Concentration (ng/m^3) ≈ 1.54